INFORMATION TO USERS

This manuscript has been reproduced from the microfilm master. UMI films the text directly from the original or copy submitted. Thus, some thesis and dissertation copies are in typewriter face, while others may be from any type of computer printer.

The quality of this reproduction is dependent upon the quality of the copy submitted. Broken or indistinct print, colored or poor quality illustrations and photographs, print bleedthrough, substandard margins, and improper alignment can adversely affect reproduction.

In the unlikely event that the author did not send UMI a complete manuscript and there are missing pages, these will be noted. Also, if unauthorized copyright material had to be removed, a note will indicate the deletion.

Oversize materials (e.g., maps, drawings, charts) are reproduced by sectioning the original, beginning at the upper left-hand corner and continuing from left to right in equal sections with small overlaps. Each original is also photographed in one exposure and is included in reduced form at the back of the book.

Photographs included in the original manuscript have been reproduced xerographically in this copy. Higher quality 6" x 9" black and white photographic prints are available for any photographs or illustrations appearing in this copy for an additional charge. Contact UMI directly to order.

UMI

A Bell & Howell Information Company
300 North Zeeb Road, Ann Arbor MI 48106-1346 USA
313/761-4700 800/521-0600

Reproduced with permission of the copyright owner. Further reproduction prohibited without permission.

ABSORPTION, AND RESONANCE RAMAN SPECTROSCOPY OF MASS-SELECTED METAL CLUSTERS IN ARGON MATRICES

By

Robert D. Craig

A dissertation submitted to the Graduate Faculty in Chemistry in partial fulfillment of the requirements for the degree of Doctor of Philosophy, The City University of New York.

1997

UMI Number: 9732905

UMI
300 North Zeeb Road
Ann Arbor, MI 48103

This manuscript has been read and accepted for the Graduate Faculty in Chemistry in satisfaction of the dissertation requirement for the degree of Doctor of Philosophy.

1/31/97

Date

Chair of the Examining Committee

1/30/97

Date

Executive Officer

Supervisory Committee

THE CITY UNIVERSITY OF NEW YORK

To my Mentors:

John R. Lombardi,Derek M.Lindsay,Evan T. Williams,
Zhendong Hu, Huaiming Wang, Egbert A. Craig, Jr.,
Philip D. Craig and,

in Loving Memory of

Veola E. Craig

Acknowledgments

I would also like to thank the many of my teachers, colleages, students, and loved ones who have made this work possible. Prof. Max Diem, Prof. William E.L. Grossman, Prof. Fitzgerald Braunwell, Prof. Richard Pizer, Excutive Officer of the Ph.D. Program in Chemistry here at CUNY, and his office administrators Mrs. Cordella Stokes, Ms. O. Diane Adebowale, Ms. Vivian Mason have put forth a great deal of patience throughout my graduate career. Prof. Daniel L. Akins, Director of the Center of Analysis of Structures and Interfaces (CASI)here at City College have eudured and stood by me through my "ups and downs". I must also mention my dear friends Mr. Timothy J. Bush, Mr. Michael Sheppard, Mr. Alfonso Scott, Mr. Frank Martinez, Mr. Lance P. Newton, Mr. Robert Limpson, Ms. Lanette Gibson, and all the staff of the CUNY Graduate Center. Of course special thanks to Dr. Hanae Haouari, Dr. Jian-Guo Dong, Dr. Alberto L. Vivoni, and Mr. Yifei Lui who help me to produce and analyze much of the spectra.

Of most importance, I must thank Provost Pamela Reid, Associate Dean Gail Smith of the MAGNET fellowship Committee and Mr. Mathew Schoengood, Director of Student Services, CUNY, who without their support, I could not have made my graduate career possible!

And, with great love, I would like to thank Joanne Fleury, for giving me the motivation to perservere when I had lost this within myself!

ABSTRACT

ABSORPTION, AND RESONANCE RAMAN SPECTROSCOPY OF MASS-SELECTED METAL CLUSTERS IN ARGON MATRICES

BY

ROBERT D. CRAIG

Advisors: John R. Lombardi, and Derek M. Lindsay

Resonance Raman spectroscopy has been employed to interrogate mass-selected metal clusters in argon matrices. Previous matrix Raman measurements involved samples which contained a variety of metal clustering species, (such as dimers, trimers, and tetramers, etc.) and resulted in ambiguous to which molecule was the spectral carrier. With the CCNY metal cluster depositon source, metal cluster cations, (produced by argon atom-bombardment) are mass-selected using a Velocity or "Wien" filter, and then co-deposited with excess rare gas on a cold window in the presence of low energy electrons. Neutralized cluster samples are interrogated by absorption, excitation, fluorescence and Raman spectroscopy. We have obtained good quality Raman spectra for many transition metal dimers (V_2, Nb_2, Zr_2, Ta_2, Hf_2, W_2, Re_2, Co_2, Ni_2, Rh_2 and Ru_2) as well

as higher clustering species (Zr_3,Ta_4, and Nb_3). Vibrational constants for these clusters have been evaluated under conditions where there is no ambiguity to which cluster species is the spectral carrier. These results have provided structural information (force constants, bond energies, geometries, etc.) which have participated in the understanding of the bonding properties (e.g. bond strengths, relative participation of s and d orbital) of small transition metal clusters as a function of position in the periodic table.

TABLE OF CONTENTS

LIST OF TABLES

LIST OF ILLUSTRATIONS

"That which does not kill us makes us stronger."
Friedrich Nietzshe

I. INTRODUCTION

The current interest surrounding metal cluster research (which can be traced to the earliest days of computational chemistry) derives in large from the challenge of unraveling the factors which most influence the first row transition metals, in stages, till properties transformate to that of the bulk material. While the properties of the free atom and that of the bulk are quite well understood, much less is known about the transformation from one to another. The primary interest of the metal cluster laboratory at CCNY is appplying spectroscopic methodologies (e.g Raman scattering, absorption, fluorescence, ESR) to study the structure and dynamical properties of mass-selected, matrix-isolated metal cluster species. These samples are particular to transition elemental clusters. The ultimate objective is to understand the structure and bonding of these species and to apply this information to problems pertinent to catalysis, micro-electronics (nano-technology), film formation, etc. In addition, advanced structural theories which aim to connect atomic, molecular and bulk metallic properties can be investigated. We have advanced theories to explain enhanced laser light scattering for certain dyes which aggregate when adsorbed onto surfaces. Most experimental studies to date have utilized non mass-selected samples, which complicates interpretation and analysis.

The class of clusters that have been interrogated are those consisting of transition metals. Clusters in this class are known to form chemically bound aggregates which can be produced by sputtering techniques. The passage from an atom to bulk material might be visioned as occurring in roughly three stages. Molecular size clusters, which have 2 to perhaps as many as 50 atoms, will have properties that are noticeably dependent upon geometry. In some undefined region, geometrical features are no longer dominate and cluster properties will be decided by a combination of lattice structure (which are not necessarily that of the bulk) and surface effects. For very large aggregates, neither geometry nor the surface will be particularly important for these species will be nearly indistinguishable from a marcoscopic sample.

In surfaces manufactured by the deposition apparatus, changes in their visible absorption spectrum,optical (Raman scattering, absorption, fluorescence) and magnetic resonance spectroscopies provides details of the vibrational modes, electronic states and geometric structure of these systems which, in turn, provides information on chemical reactivity and electronic properties.

In order to undertake such spectral analysis, it is appropriate to first identify the spectral carrier. An essential feature of our experiment involves the deposition of sputtered(secondary ion), mass-selected metal clusters. These must be produced in sufficient number to be detectable and this in turn requires a very high brightness sputtering source(the primary source). Heavy gas (argon, krypton, etc.) primary ion beams operating at energies of up to 30 keV are known to be efficient secondary ion producers. The secondary ions must be deposited at low energies in order to have minimum fragmentation (soft-landing conditions), which requires a very large available secondary ion flux. These experiments have yielded spectroscopic (i.e. structural) information on ground-state metal aggregates and ion clusters with adsorbed molecules. This information obtained with the subject apparatus in combination with findings from theoretical studies conducted in our laboratory, will allow us to better understand metal cluster structures and reactivities.

Only with the recent advent of mass-selection cluster deposition techniques, has it become possible to overcome these assignment problems.[19] The importance of mass-selection is illustrated by the elegant experiments of Honea et. al.,[20] who have recently reported matrix Raman measurements on Si_4, Si_6 and Si_7 and are able to predict cluster geometries by comparison of their observed spectra with frequencies form calculated structures.

In the past, such information about these clusters could only be obtained by performing large scale quantum mechanical calculations. The mathematical solutions to these "*ab-Initio*" and Ligand field methods take a great deal of time to arrive at, even with the help from large mainframe computers. Nuclear and electronic motion in atoms and molecules can yet only then be approximated by such calculations, which involve solving many complex one and two electron differential equations. Such calculations must be correlated with experimental results; exactly those which we have obtained with the CCNY metal cluster deposition source.

The CCNY cluster deposition apparatus is described in detail in Refs. 21 and 22. Briefly, an intense argon ion beam (15 mA at 25 KeV) sputters cluster ions from a metal target maintained at about 350 V. Secondary ions are extracted at 2-3 KeV, mass selected with a Wien Filter, bent by 10 degree inclination (in order to separate neutral species) and then co-deposited with low energy electrons and the matrix gas (argon) on a cold CaF_2, Aluminum, or Sapphire substrate, typically -260 °C/13 K. The deposition region (Ref. 22, gives a fuller description) is enclosed by a "Faraday cage" whose potential with respect to the sputtering target controls the kinetic energy (about 10 eV in our experiments) of the deposited ions. The fragmentation can be estimated by comparing the ratio of atomic features in a cluster deposition to those obtained from depositions of the atom.

Resonance Raman spectroscopy in the only method to obtain vibration constants for homonuclear metal clusters, as they have no dipole moment. As consequence, it is first necessary to map out the cluster absorption spectrum to observe this effect, as you must excited into the absorption bands of the molecule. This method has been found to increase the signal intensities by factors of 10^3. Also, you should then to have available both a wide range of laser wavelengths and a correspondingly versatile detection system to excite in the absorption bands found by scattering-depletion spectroscopy.

In our laboratory, we have lasers (large frame argon ion, standing wave dye and CW-Titanium sapphire) which cover (almost continuously) the UV-Visible to the Far Infrared region of the energy spectrum (a 275 - 1000 nm range of wavelengths). As a detection system, we have been using a double 1/4 m monochromator combined with either a Hamamatsu R943-02 photomultiplier tube, or (for wavelengths beyond about 800nm) a low noise (4 Hz dark count) silicon diode detector. However, as of February of '94, we have upgraded to the Spex 1877 "Triplemate" monochromator equipped with the "Spectrum-One" CCD detector. This has allowed us less analysis time, larger limits of detection, and the ability to describe and characterize the vibrational and dynamic properties of such transition metal clusters.

Chapter II. Apparatus Design and Experimental Technique

2.1 CORDIS Ion Source:

The CORDIS ion source produces an intense, high energy and well collimated beam of gaseous (Argon, Krypton, etc.) ions. Specifically, a 25 KeV argon ion beam can routinely produce currents in excess of 15 mA with a 10 mm beam diamter 0.5 m from the source. The benefits of employing this specific instrument are above any laser vaporization or desorption method known to-date.

The CORDIS plasma ion source is also the only production-line instrument in the world which has been field-tested for brightness requirements relating to deposition experiments using mass-selected metal clusters. While there are are ion sources manufactured in the United States, none of these instruments has demonstrated an ability on a routine basis to provide sufficient secondary ion cluster intensities to allow for the types of spectroscopic studies described. Past trials at the Ecole Polytechnique Federale'de Lausanne show secondary, mass-selected silver dimer cation currents approaching

100 nA. These fluxes allow secondary ion energies to be reduced to a point where soft-landing conditions are practical. Relatively few domestic manufactures produce plasma ion sources. Furthermore, these domestic products are inadequate for our research program in that they produce insufficient current and/or are suitable for lighter gases and/or have low beam energies.

The decisive specifications for our intended research is the ability to produce large, continuous (10-100 nA) currents of mass-selected transition metal clusters which can be subsequently decelerated (to < 10 eV) and deposited with low energy (<1 eV) electrons and excess rare gas (ratio: > 1000:1) as a solid matrix sample and under conditions of minimum fragmentation. Critical to this process is a proven (in the context of secondary ion production), reliable primary ion beam producing 10-20 mA argon and/or krypton cations at energies of 20-30 keV. The primary beam must be transportable over 600 mm while maintaining a beam diameter, $3 < \theta < 10$ mm.

Electrons are evaporated by 6 tantalum (Goodfellow, 0.03″ Ta coil, 99.9%) filaments connected in series at the back end of the ion source chamber (see below). Voltage is applied to the filament connection by a TCR products "constant voltage/constant current" supply, which is floated at the ion potential applied by the Glassman Power supply (Glassman high voltage 25 kV supply) in conjunction with the "Screen" lens supply of minus 2 or 3 kV Glassman supply. These coils must be replaced regularly, and are done so by applying 8 turns around an an increment borer, sliced at 2 cm in length, and situated arounded the filament spindle made of molydenum, parrallel to the beam axis.

Parrallel connection of these filament wires is prefered over series, due to the fact that the current drop across the filaments will be proportional to the degradation of the filament wires with time. As the current through the filaments decreases, due to the erosion of the filament material, the resistance will increase at constant voltage. This feature also allows for protection of this circuit line.

Secondary ion currents limit the number of neutral cluster species that can be trapped in rare gas matrix. This in turn determines the minimum sensitivity requirements of the spectroscopic techniques applied to the analysis of the samples and, accordingly, the detail of the information extractable from these experiments, as for example resolution, is a performance characteristic that expresses the ability of a spectroscopic instrument to distinguish between closely spaced (in the frequency domain) spectral features. It also determines the degree of distortion introduced by the instrument in the shape of spectral lines. Our research requires the observation of molecular spectral features well distinguished from each other and at the same time free of distortion in their relative intensities that might be caused by overlapping wings of spectral bands. Since resolution is intimately related to signal intensity, optically dense samples are crucial. For example: visible absorption techniques generally need sample absorbances of 10^{-2} or better for adequate noise suppression; ESR techniques require (in the case of many hf transitions) collecting 10^{15} - 10^{16} cluster species. For both examples, secondary ion currents of 10 nA (as discussed above) can produce useful samples following times of about one hour.

The actual source is a slightly diversified model of the high-current ion source type CORDIS, developed at GSI Darmstadt for use with gases. CORDIS relies on the principle of a magnetic multipole/reflex discharge. The ion beam is formed by a single-aperature accel/decel extraction-system which can be aligned independently of other source parts. The extraction plates can easily be replaced by others to allow, for example, the installation of multi-aperature plates if higher beam currents than actually specified should be desired at a later time. Since in the different processes of ionization and beam formation power loads of several kilowatts are involved, care must be observed in preparing and operating the source.[26]

The whole source is to connected to the beam line with its 100-mm conflat (CF-100) flange. When mounted in the horizontal orientation the source must be externally supported when completely assembled; the high voltage insulators(4″x 2″x 8″) are not designed to carry the entire weight of 45 Kg freely. This is done by mounting the source first to a Super-pillow block (SPB-16-0PN), and then securing it to a steel metal assembly.

With the previous overview, refer to Figure 2.1, which is a simplified drawing of the ion source. Note, however, that this is a basic one and several viewing sections are rotated into the drawing plane.

For a complete service, all units of the ion source must be disconnected: cathode chamber, discharge chamber, and extraction system, however, order of disasssembly doesn't matter in which order. The assembling of the extraction system does not present any difficulty, but the three extraction electrodes must be aligned very carefully. This alignment is a delicate procedure and very important for the performance of the extraction system. The delivered aligning rod is machined to a diameter of 0.01 mm less than the aperature widths on the three extraction plates and can be passed through all three apertures if the alignment was carried out correctly. A tunable table must be used to mount and make sure the extraction electrodes are aligned with a precision up to 1/1000 of a degree, perpendicular to each other. Any tilt in these lenses will decrease the argon ion flux at the target, and possibly miss direct the beam. This has resulted in the argon ion beam also hitting the target holder, adding copper an iron as impurities in our samples. Such precautions are consequent of the particular experimental arrangement of the user.

2.2 SPUTTERING CHAMBER: TARGET AREA

The sputtering chamber is of custom desing by Dr. D.M. Lindsay and Dr. Z. Hu, constructed by MDC (MDC Vacuum Product Corp., Hayward, CA). It is a eight port, 18″ diameter, 12″ high drum which allows for the ion source entrance, cluster extraction at 50 degrees, visual ports, and ion gauge mounting. The total top and bottom circumfrances allow for support and evacuation of gases by a Balzers turbo molecular pump (TPU 510, Balzers Pfieffer, Germany Gmbh),as well as access through the top. Of most interest, is the target holder, or top plate of this chamber. Three 2-3/8″ ports are alinged in a row across this chamber, two of which are used to (1) allow for insulation of target, target voltage and support for the internal target holder, and (2) for a manipulator to rotate this holder also of MDC design. The target holder assemebly is customed designed by our laboratory.

As shown, the ports (Del-Seal flanges, 304 SS) are 8″ non. O.D. (F5), 6″ nom. O.D. (F2), 4-1/2″ O.D. (F3) and 2-3/8″ O.D. (F1). A 6″ port (type F2) and a 8″ port (type

F5) have been made available at a 50° inclination, to provide the maximum effiicency for the flux of positive ions off the target surface. The chamber is equiped with an ion gauge (Inficon Corp.) situated behind the target holder, secured in a 2-3/8″ (type F1) port. The top flange target and manipulator ports must be insultated with a glass fittings, as to ground or allow voltage control of the target holder itself.

2.3 SECONDARY BEAM LINE

A simplified diagram and a photograph of the secondary beam line of the CCNY deposition source (see Figure 2.3). It consists of first a Colutron 200B extraction system, a 600B extraction system, drift space, and a set of Einzel lenses.

2.3.1 COLUTRON 200-B lens System

The extraction lens system consists of 4 concentric electrostatic rings, (3 mm thickness, 1 mm aperature) which draw ions produced by sputtering into the velocity filter. Only two of these lenses are allowed to float while the other two are at ground potential (see below).

Lens A1 is the first lens in the voltage train, and the first voltage the cluster ions meet after being sputtered. This lens is usually maintaned at 360 V, while now current is allowed to pass through it. An additiional voltage of -1500V (Keithly power supply) is run from this plate to faraday cage, which encases the faraday plate (ion measurement) and the substrate plate supported by the cold finger (ADP Displex refrigerator). Lenes C1 and C2 are not at ground, (permitted by an octal feedthrough, ISI Insulator

Seal Incorp., Hayward, CA 94545), and carry voltages of appoximately 300V and 250V (Kikusui DC power suplies, Model PAB18-1A, Kikusui International Corp., Torrance, CA). Lens A2 completes the extraction system with a static voltage of approximately 300 V, and deflector plates D1(+) and D1(-) make for additional adjustment to maximize the flux of ions through the 600-B lens system.

To increase resolution of the secondary beam line, decisions were made to "Float" the line (-1000 to -1500 V).

2.3.2 COLUTRON 600-B lens System (Wien Filter)

Colutron (Colutron Corp., Colurado) also offers a model 600 series velocity filters, with a larger range of system combinations. The overall length for the model 600-B is 10" and the side feed-through ports are centered between the two standard rotatable 8" Conflats, with 6" ID.

Liquid cooling was then addded to make higher currents possible, so higher magnetic field strength can be obtained. We have sided with the bakable model, although our experiments have never required that we do so. At the time of this dissertation, specifications and operating conditions for both models may be found from the Colutron corporation at their World Wide Web address

Wahlin@Colutron.com of by contracting Dr. Erik Wahlin at Colutron Co..

Cooling of the encapsulated magnet coils on Model 600B must be done by Freon, Refigerant 11 of 12. Refrigerant 12, however, has been found to have a greater viscosity and more appropriate thermal properties, and the Colutron corp recommends Dupont HFC -134a). Freon cooled baffles connect return line to magnet coils for cooling, maintained by a homemade circulator. (See above, Figure and Picture of complete system)

Pressure was monitored by a one-stage valve placed on top of the MDC housing (6″ I.D. 8″ O.D.-rotatable, 304-SS) for the 600-B lens system. Temperature was inturn, overseen by an Omega temperature indicator interface, with scientific instruments 5500 thermocouple temperature controller, designed as well by Dr. Z. Hu and Dr. D.M. Lindsay.

A 175 mm drift space (see above) has been provided to increase the M/δM of the velocity filter. After exiting the filer, ions are still further controlled by deflection plates D2(-) and D2(+) (see above). The dimensions of the drift space further alow for the spread of ions, much like a quadrupole mass filter. Einzel lens, designated L1 and L2, then direct ions into the the deposition region. A 10 degree inclination, allowed by the use of a belows flange, restrict neutrals of comparable flux from reaching the deposition region.

2.4 THE DEPOSITION REGION

The cold finger (ADP Displex) with substrate support is allowed to fit into the top of a six-way cube (CU800-6, MDC Vacuum products) of 9.97″ o.d. The cube is supported by the second Turbo molecular pump (TPU 510, Balzers Pfieffer, Germany Umbh), and surrounded laterally as follows (See below).

The Displex refrigerator's primary and secondary displacers are concealed by a belows flange, which is supported by rods, so as not to be "pulled-in" by the pressure created due to the turbo molecular pumps.

Such an arrangement allows einzel like lens (designated L1, L2 and L3) to guide the cluster of concern to be meet by electrons by an tungsten filament, (Philips Electronic design), and trapped in a matrix of Argon, Kryton, or Xenon. A scematic of such a "soft-landing" of metal clusters may be found elsewhere, however, a simplified diagram is shown below, (Figure 2.8).

The interaction of electrons with cluster ions has is sufficient to neutralize positive cluster ions as they are trapped in the Argon matrix at atleast 14 K. Since the ionization potential is less than the bond energy, we expect neutralization to occur before the clusters are imbedded into the matrix.

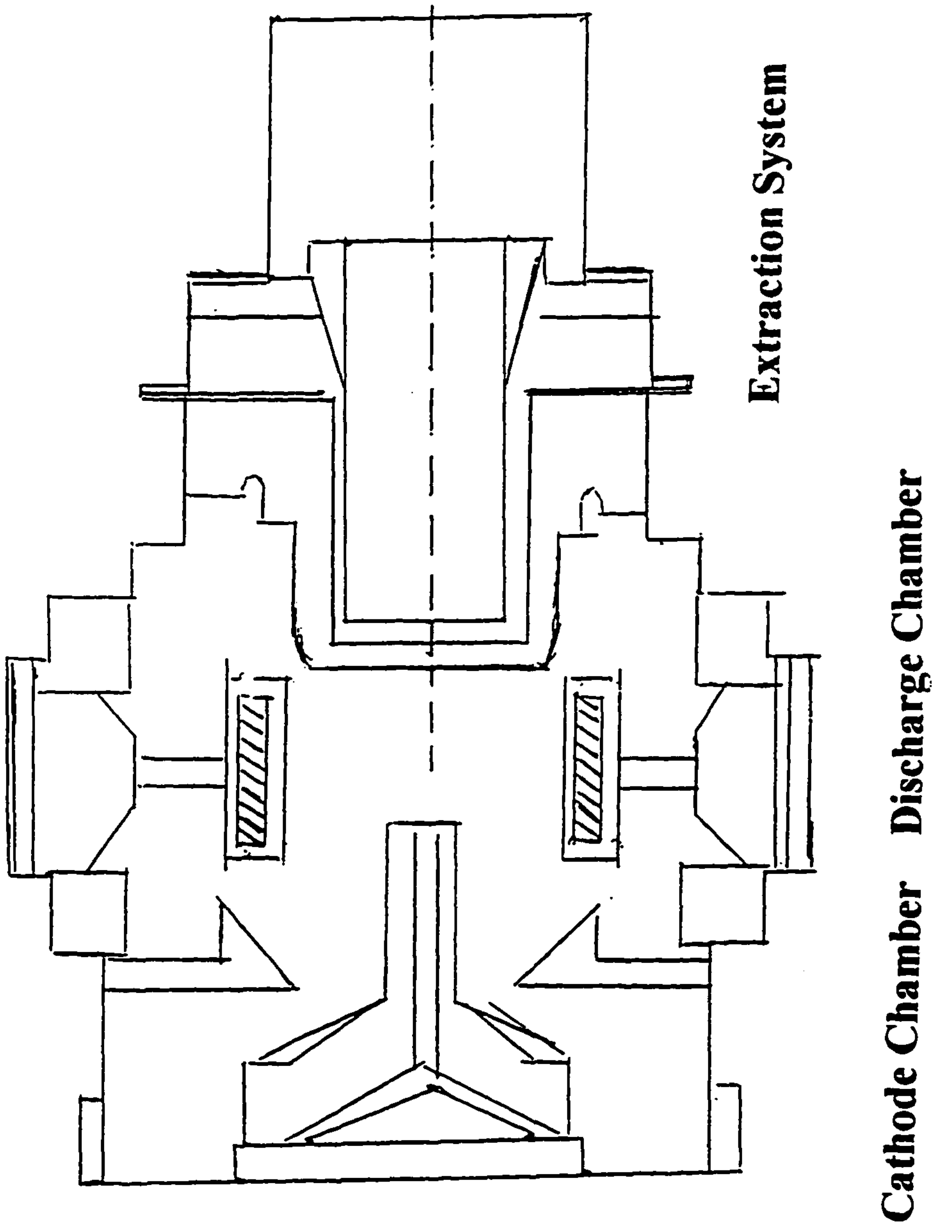

Figure 2.1. Simplified representation of Ion source

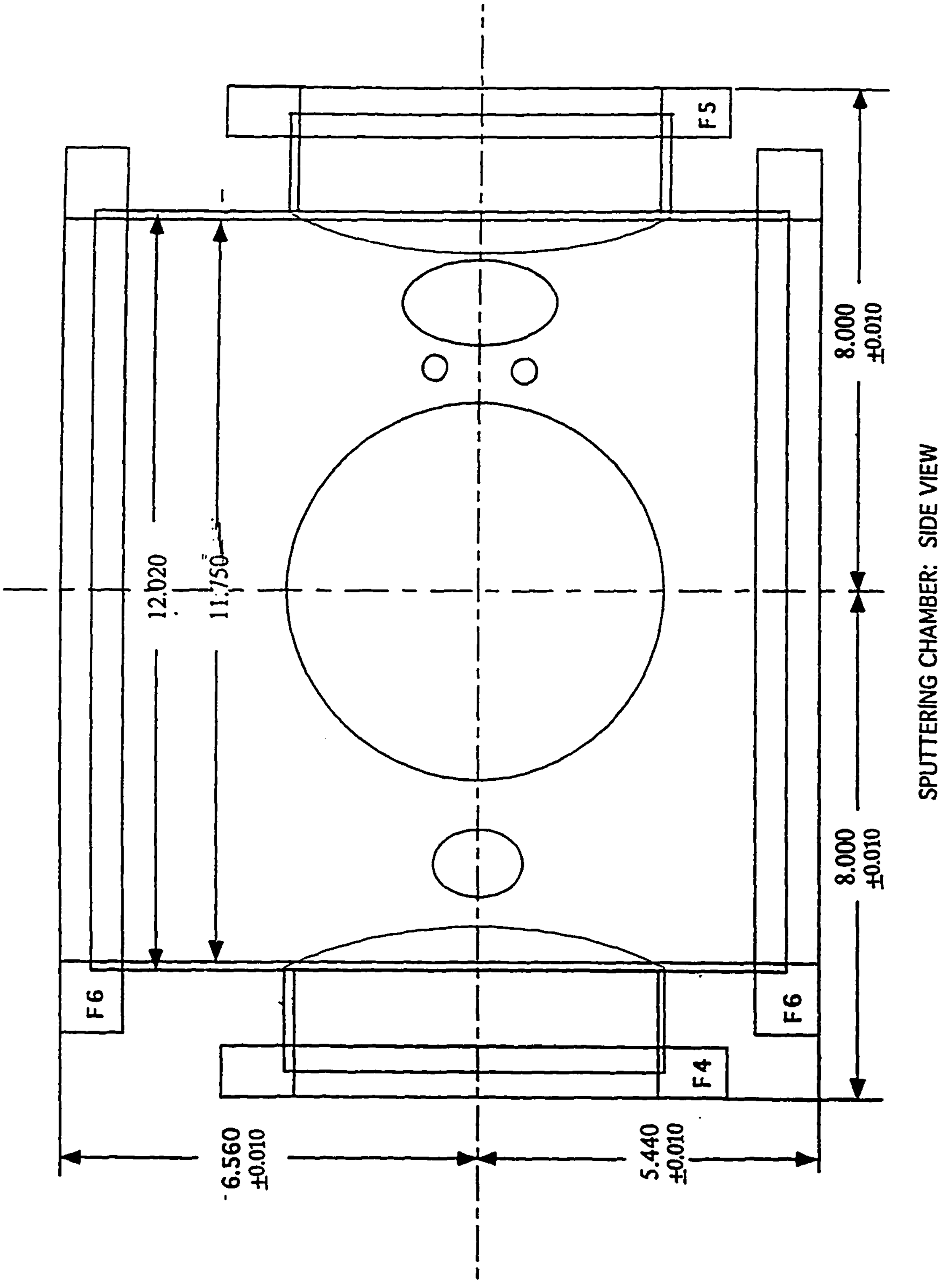

Figure 2.2. Sputtering Chamber(Side View)

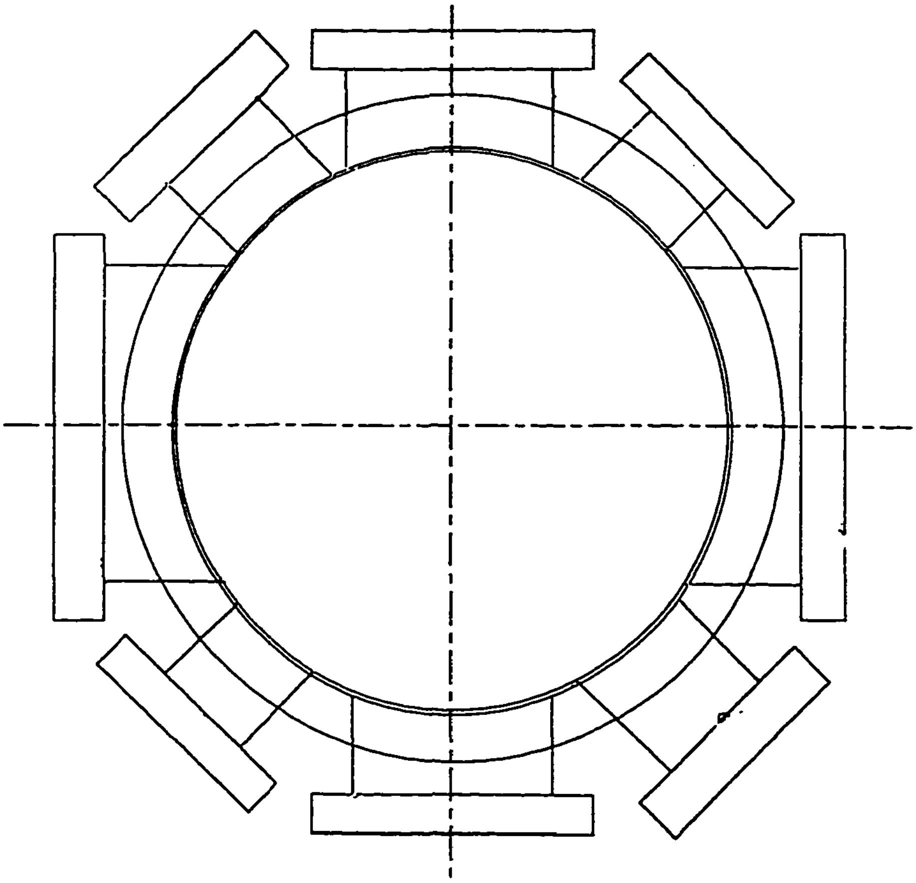

Figure 2.3. Sputtering Chamber(Top View)

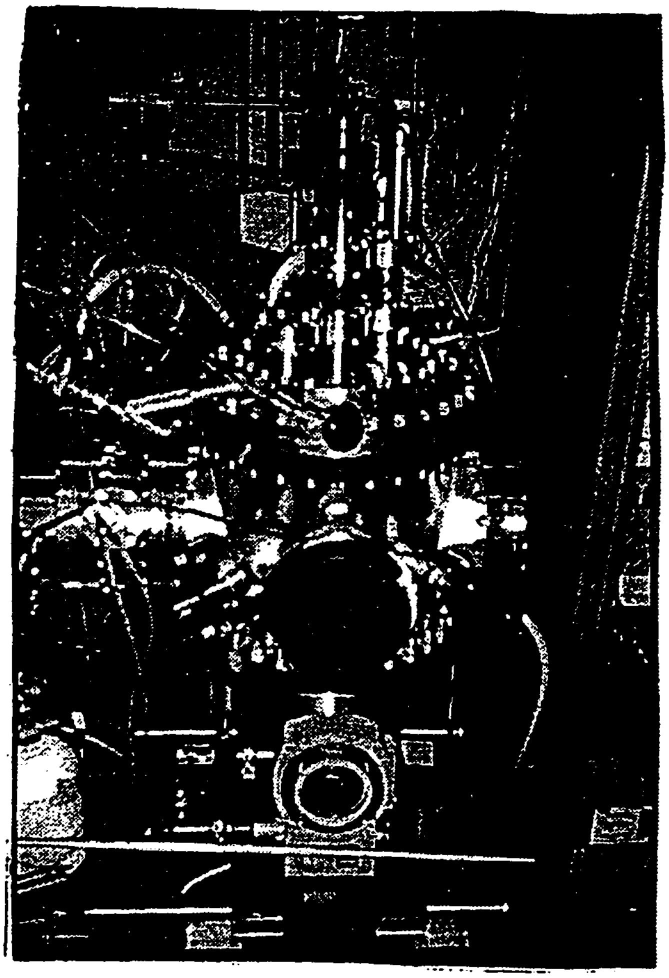

Figure 2.4. Picture of Sputtering Chamber

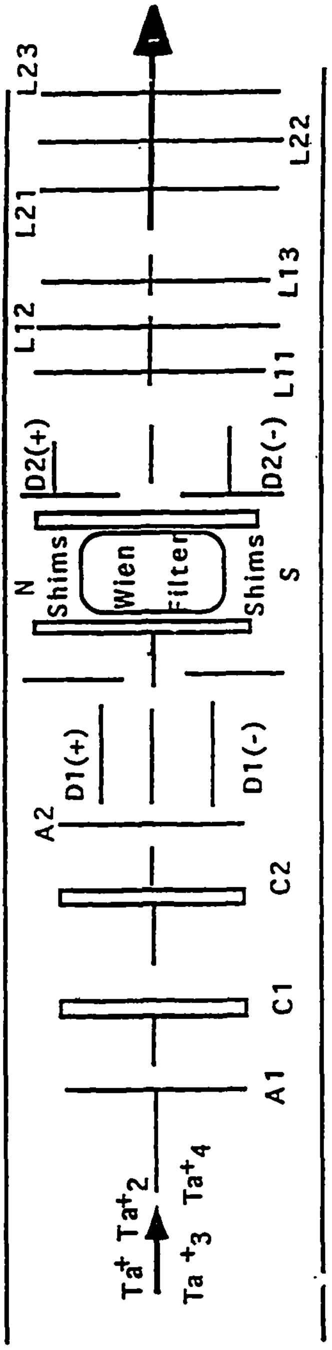

Figure 2.5. Schematic of Secondary Beam Line

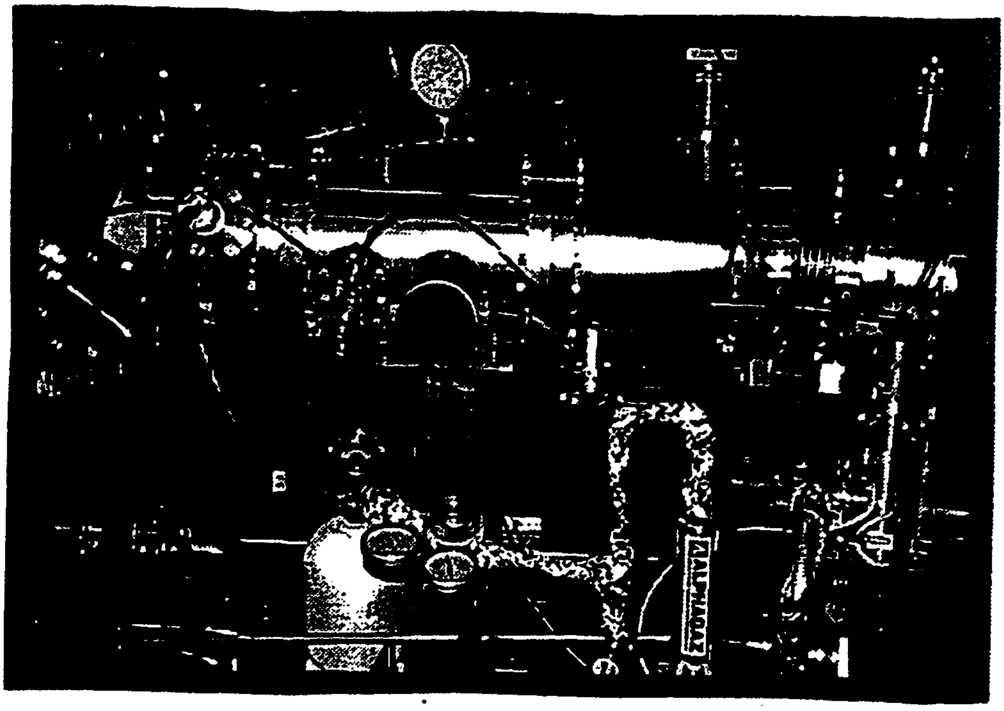

Figure 2.6. Picture of Secondary Beam Line

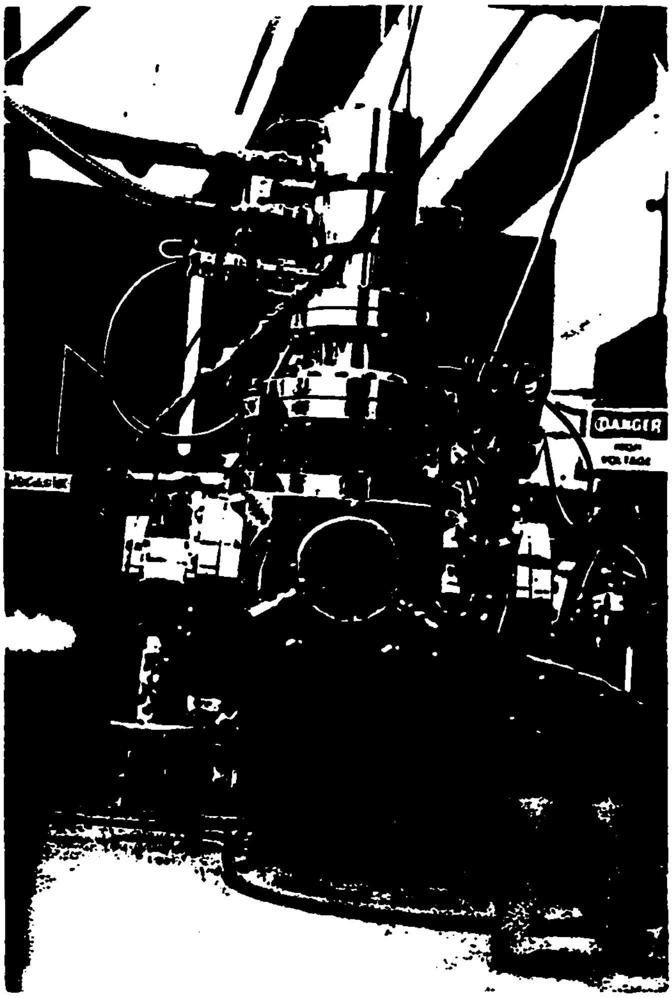

Figure 2.7. Picture of Deposition Region: Hex Cube and Cryostat supported by Balzers TurboPump

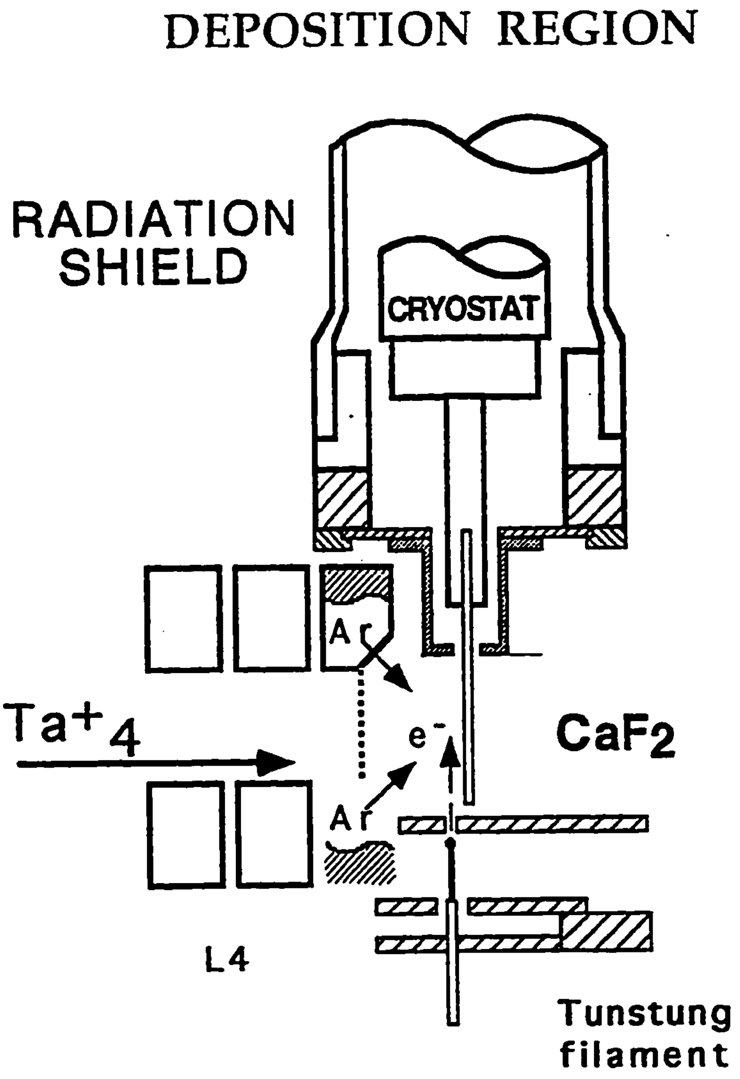

Figure 2.8. "Soft landing" of Positive Metal clusters in Rare gas matrix, with neutralization of electrons

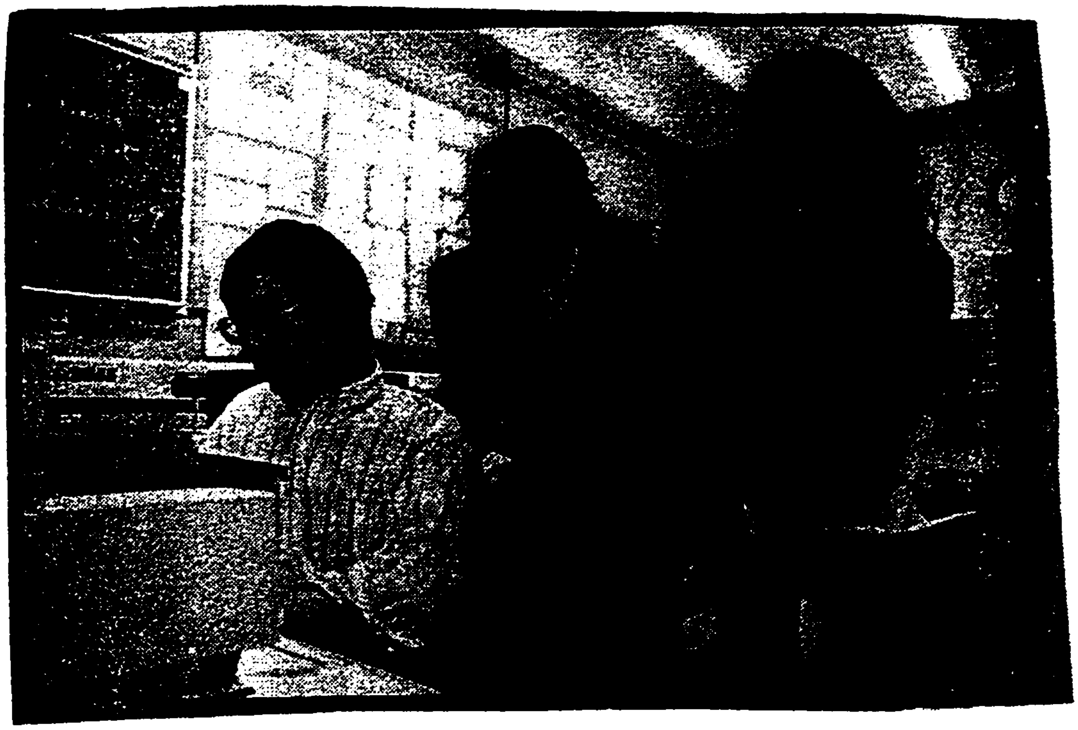

Figure 2.9. The Metal Cluster Group

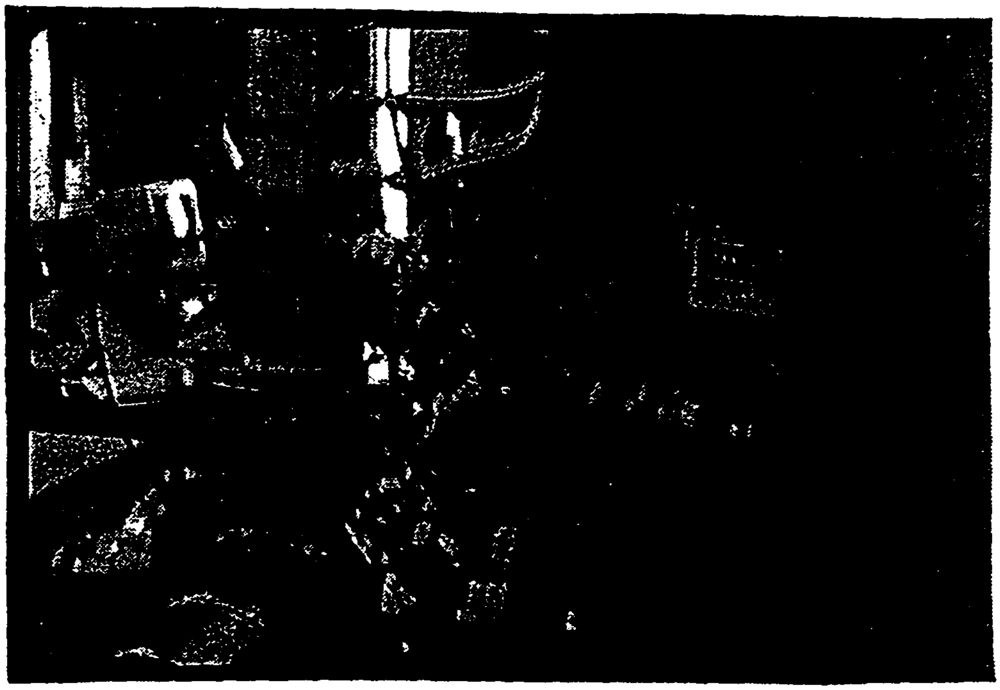

Figure 2.10. The Metal Cluster Deposition Source

Figure 2.11. (From left to right) Prof. Huaiming Wang, Dr. Wumin Wang, Prof. John R. Lombardi, Mr. Yifei Liu, Dr. Robert Craig, Dr. Abdula Cavus, and Dr. Hanae Haouari

Chapter III. Spectral Information from Mass Scans, Absorption, Excitation and Raman Spectroscopy

3.1 Mass Scans:

The mass scans are obtained by a Faraday plate situated in the deposition region, perpendicular to the substrate. Cluster ions which are accelerated through the secondary beam line (described above) can be monitored by reading the current of the positive ions meeting this plate, with dispersion sufficient to separate the dimer from the trimer from the atomic mass current. Mass scans are read by software written by this laboratory. Below, the mass scan spectra for various transition metal clusters are shown (Figure 3.1) In many ways, it is this data which decide what higher clustering species may be analyzed, and exploited for their spectroscopic properties.

3.2 Excitation Spectroscopy:

The kinetic energy distribution of arriving ions (measured by applying a retarding potential to the Faraday plate) is centered close to the target potential and has a full-width at half maximum (FWHM) of 10-20 eV. Suprisingly, few dimers (neutral bond energy, 4 eV)[10] are fragmented by the deposition process. Measured dimer fragmentation ranges from < 1/2% for (e.g.) Ta_2 (bond energy 4 eV)[23] to approximately 15% for V_2 (bond energy 2.8 eV)[23] and 30% for Ni_2 (bond energy 2.03 eV)[25] . A plot is also shown in Figure 3.2 for the fragmentation of Ag_2 with deposition energy. Ion current for V_2 verse Ion energy (under soft-landing conditions), and the V_2 energy distribution is shown in Figure 3.3 and Figure 3.4, respectively. Generally, increase of fragmentation with ion energy may be estimated by comparing the intensities of atomic excitation features in a cluster deposition with those obtained during a dimer, trimer or tetramer deposition under similar conditions. Thus, the atomic signal from fragmentation is often comparable to that arising from the few neutrals which manage to negotiate the 10° bend, as determined by experiments in which ions were prevented form reaching the deposition region by applying a suitable retarding potential. Since the ionization potential of a cluster is generally larger than its bond energy, we suppose that the matrix surface plays an important role in supressing fragmentation during the neutralization step. Interestingly, the deposition of dimer ions without electrons also leads to a Raman spectrum, but it is approximately 10 times weaker (when scaled for equivalent conditions) than that obtained with electrons added. A similar result pertains to Excitation spectra when just the atomic ion is deposited. A similar phenomenon has been noted for the deposition of atomic silver ions.[21]

The same optical arrangement as for absorption spectra is employed; however, there are two differences. First, the mirror M1 is disabled by our customized software to project light at one particular lateral position on the substrate; secondly, low pass filters are placed in an Oriel Corp. filter holder placed before the PMT (Figure 3.5)

3.3 Absorption "SDS" Spectroscopy:

Absorption spectra are measured by a method developed by Prof. Lindsay, in which the reference region is the outer edges of the substrate plate, and the signal region is at the center of the substrate where the concentration of the cluster species is rich. The term "Scattering Depletion Spectroscopy" may be used to define such a technique. Due to the fact that our samples are amorphous, (even at 13 K and 10^{-7} torr), as well as the ability to direct cluster ions within approximately a 2 mm region on the substrate, we may measure the dense cluster region in the center of our substrates by atleast 10^2 counts/second with a reference intensity of 2 x 10^6, characteristic of the dilute perimeter of the substrate plate.

The Absorption condition may be expressed as

$$R^{sds} = \{1 + \alpha_a/\alpha_s\} \frac{1 - \exp(-as)}{1 - \exp(-a_s - a_a)} \qquad (1)$$

Where α_a and α_s are absorption and scattering coefficients, proportional to the number of absorbers/scatterers and the sample thickness.

For strongly scattering samples, SDS has an advantage over normal absorption spectroscopy, due to a flatter background.

To accomplish this, a stepping motor (Compumotor Co.) has been situated to direct light emitted from a tungsten and a deuterium lamps, after passing through a Spex monomate, projected to meet the sample plate at a right angle. Over 12 positions may be selected laterally across the substrate plate. A reference region, such as position 2 along the substrate, may be used as a reference region to that of position 7, approximately 1 and 4 mm along the substrate in question. A description of the setup may be found in Ref. 21. Prior to recording scattering depletion spectra, an optical density profile is obtained by recording single beam spectra as a function of lateral position on the sample. It is generally found that the sample is non-uniform, with about twice as much absorption in the center as compared to near an edge. Thus, the reference also contains sample characteristics of the matrix (see Figure 3.6).

Position of light from the Spex monomate must be carried out by eye. The interface software designed by Dr. George Sukenick and Dr. Zhengdong Hu in Quick Basic 4.0 is run on a 386 PC AT, and allows for clockwise and anti-clockwise settings of reference and signal regions.

3.4 Raman Spectroscopy:

Although matrix samples may be interrogated by excitation and fluorescence spectroscopy[19], transition metal clusters (apart from a few examples, e.g. Group IB clusters and Mo_2)[23] show a notable lack of fluorescence. Accordingly, Raman spectroscopy is a relatively sensitive probe of these species, provided that the exciting laser is resonant with an absorption band.[24] As a consequence, it is first necessary to map out the cluster absorption spectrum, and then to have available both a wide range of laser wavelengths and a correspondingly versatile detection system.

In the Raman spectrum, we encounter the effects of molecular vibrations. It is instructive to examine the spectrum of a diatomic molecule first. A diatomic molecule has only one chemical bond, which may be modeled in the lowest approximation as a harmonic oscillator, The energy levels are simply:

$$E_{vib} = (n + 1/2)h\omega_e \qquad (2)$$

The quantum number n can take on values of 0,1,2,3 ... while ω_e is the classical oscillation frequency of the harmonic oscillator and is equal to $2\pi(\kappa/\mu)^{1/2}$. Here μ is the reduced mass of the diatomic molecule and κ is the harmonic force constant. In fact, it is this latter that is most chemically interesting because it is intimately related to the nature of chemical bonding. More realistic models can be obtained by considering anharmonic corrections to the above formula. If x_e and y_e measure cubic and quartic distortions to the quadratic potential, we obtain:

$$E_{vib} = (n + 1/2)h\omega_e - (n + 1/2)^2 h\omega_e x_e + (n + 1/2)^3 h\omega_e y_e \qquad (3)$$

Where for example, the dissociation energy, defined by the Kratzner relationship, $D_e = \omega_e^2/4\omega_e x_e$. For an exact harmonic oscillator, the strict selection rule $\delta n = \pm 1$ holds, resulting in the observation of a single line in the spectrum at the fundamental frequency ω_e. However, anharmonicity mixes harmonic wave functions, resulting in a breakdown of the selection rules. The result will be the observation of overtones at approximately $2\omega_e$, $3\omega_e$, ... Note however, each succeeding overtone will be spaced more closely to the last due to the negative sign in the second term, until the states merge into a continuum at the dissociation energy, D_e. Above this energy the molecule dissociates into separated atoms in various atomic excited states.

For polyatomic (N-atoms) molecules, the situation is much more difficult to define. Of course, there will be 3N - 6 independent vibrational degrees of freedom held to others with individual stretching force constants along each chemical bond. Bending motions may also be included by adding angular force constants. The resulting force field may be represented in matrix form, which upon diagonalization, will provide a set of collective, in-phase oscillations of the nuclei. If the potential energy for vibration is expressed interms of these 3N - 6 normal modes, in the harmonic oscillator approximation, the vibrational energy will be given by:

$$E_{vib} = \sum_{i-1}^{3N-6}(n_i + 1/2)\hbar\omega. \qquad (4)$$

So that each normal mode oscillates as though it were an independent oscillator. We then expect the harmonic oscillator selection rules will apply to each mode separately. However, anharmonicities can allow overtones to be observed as for the diatomic case, and furthermore, combination bands in which several oscillators are simultanously excited can be observed. Needless to say, the resulting spectrum can become quite complex for large molecules. Often, in order to completely account for the spectrum, interactions between non-bonded atoms must be added to the force field. These Urey-Bradley forces may often have a large effect on the observed spectrum.

Spectrum intensities are not only governed by the harmonic (or anharmonic) selection rules, but the intensities may also be shown to be proportional to the square of the dipole moment derivative with respect to the normal mode of vibration. Thus, since the advent of lasers, Raman spectroscopy has taken an increasingly prominent place in the study of molecular vibrations.

The Raman effect was predicted by Heisenberg in the 1930's, but due to the weakness of the effect, it was only observed by C.V. Raman some years later. It is related to the phenomemena called Rayleigh scattering, which is caused when an molecule is placed in a non-resonant oscillating electric field. The molecule is caused to oscillate at the same frequency through its susceptibility, radiating light in all directions. The intensity of this scattered light is proportional to ω^4, so that high frequency light is much more apt to be scattered than that of lower frequencies.

When a molecule is stimulated by an oscillating field, the ensuing scattering may also mix with the natural oscillation frequencies of the molecule, due to both rotations and vibrations of the normal modes. The resultant light, also scattered in all direction will contain both the sum and difference frequencies, causing a shift in scattered frequencies by the amount of internal oscillation. This is what is responsible for the Raman effect. The magnitude of this effect is small, often as little as 10^{-6} times weaker than Rayleigh scattering. Thus, in order to be observed, an intense highly monochromatic light source is needed. Most early work was carried out with atomic emission lamps, such as mercury, but the problems involved made routine spectroscopy difficult. Since lasers have become commonplace in modern laboratories, the use of Raman spectroscopy for spectral analysis has increased dramatically.

The information contained in a Raman spectrum is, in principle, the same as that of an infrared spectrum. By determining the Raman shifts with respect to the Rayleigh line, we may measure both vibrational frequencies. The Raman intensity is proportional to the square of the susceptibility $X^{(1)}$ α_{on}. The quantum expression for this quantity is given by:

$$\alpha_{on} = 2/\hbar \sum_{m} \frac{\omega_{om}}{\omega_{om}^{2} - \omega^{2}} \left| \langle 0|\mu|m\rangle \langle m|\mu|n\rangle \right|^{2} \qquad (5)$$

The sum over m runs over all excited molecular states. Note the selection rules depend on two different dipole moment matrix elements being simultaneously non-zero. These are sometimes referred to as two-photon selection rules. Note for this case, the restrictions on microwave and infrared spectra on homonuclear diatomic and non-polar molecules, do not apply. Raman spectroscopy is the major way in which spectra of non-polar molecules are obtained.

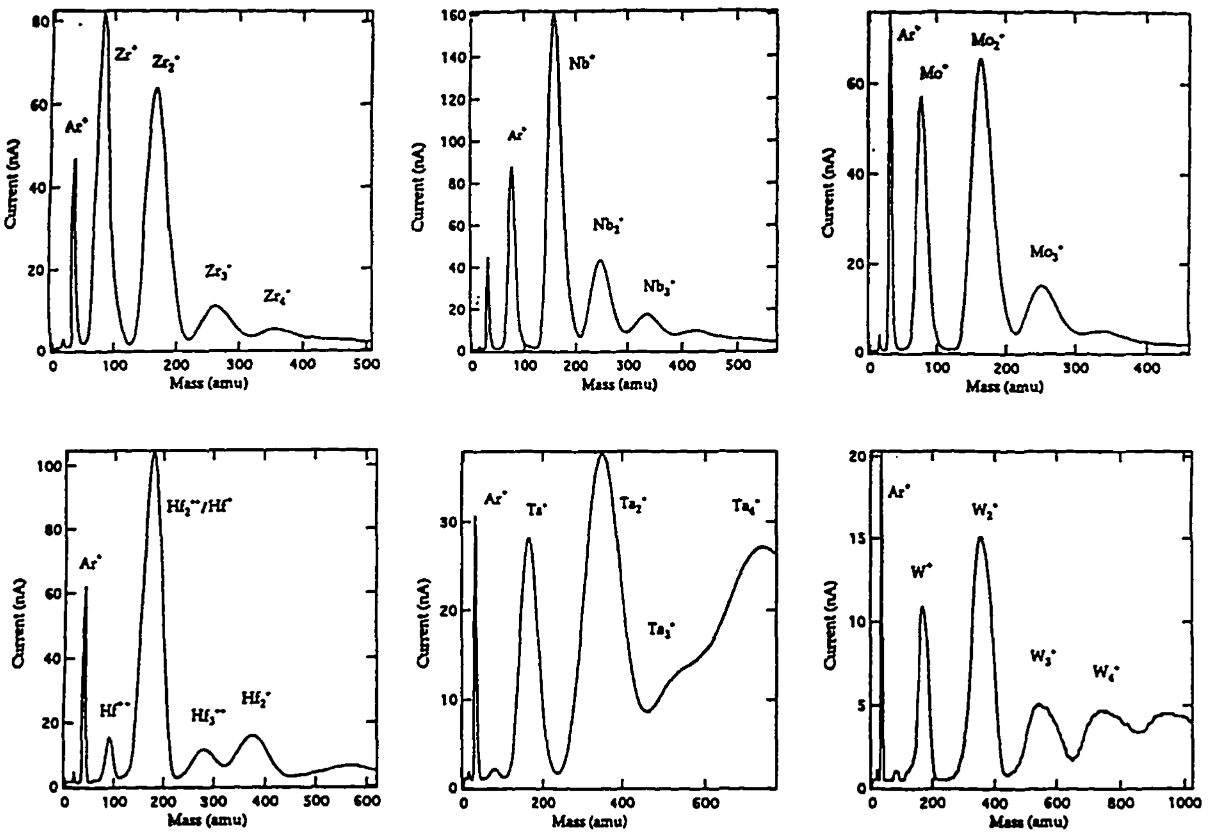

Figure 3.1. Mass scans of transition metal clusters obtained by the CUNY depostion apparatus

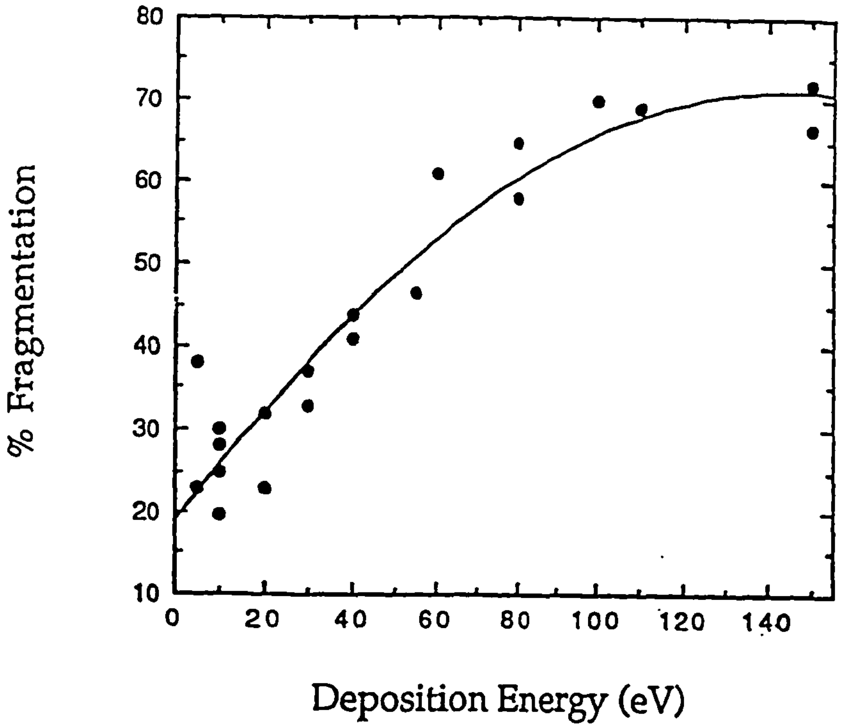

Figure 3.2. Fragmentation of Ag_2

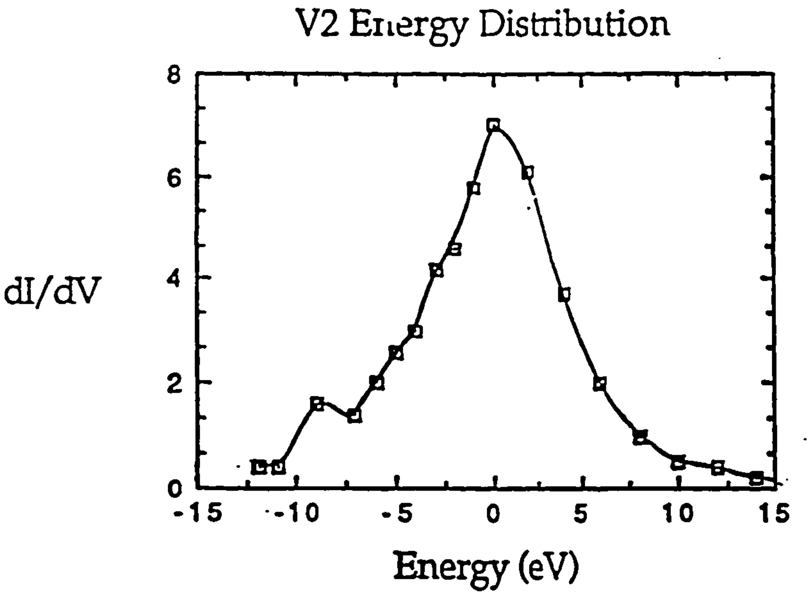

Figure 3.3. V_2 Current vs. Ion Current

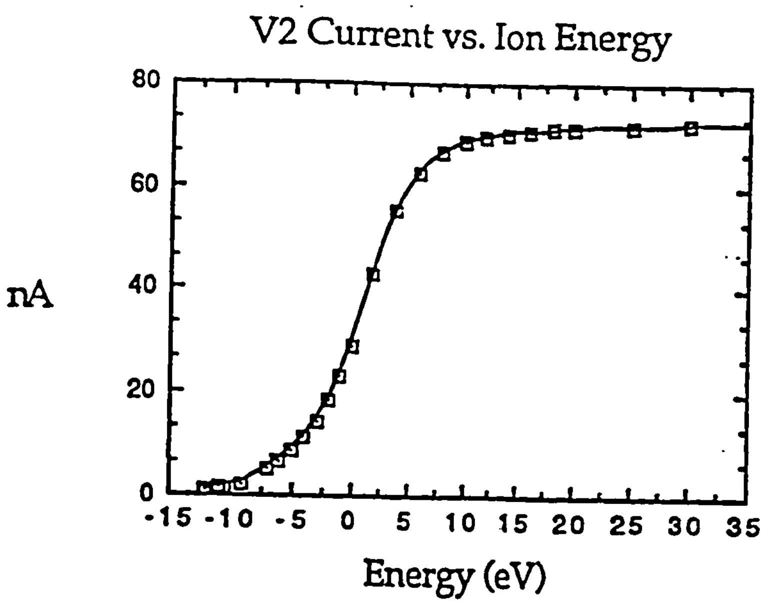

Figure 3.4. V_2 Energy Distribution

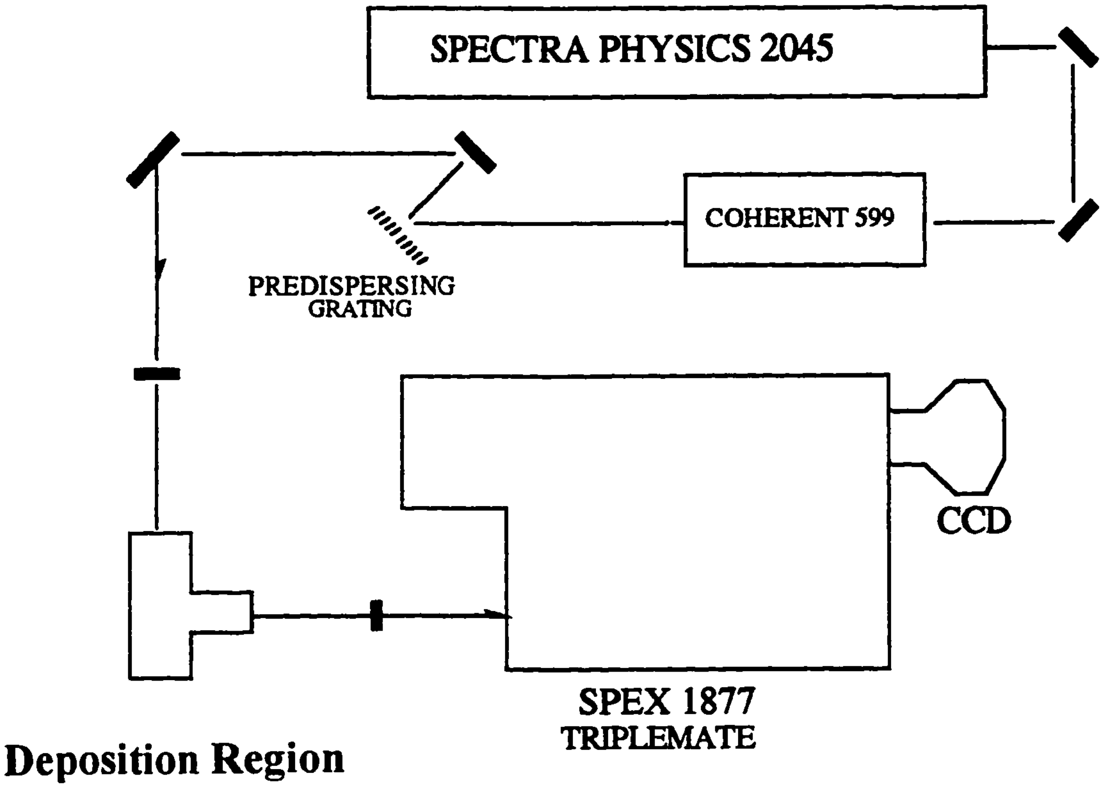

Figure 3.5. Schematic of Raman and Excitation system

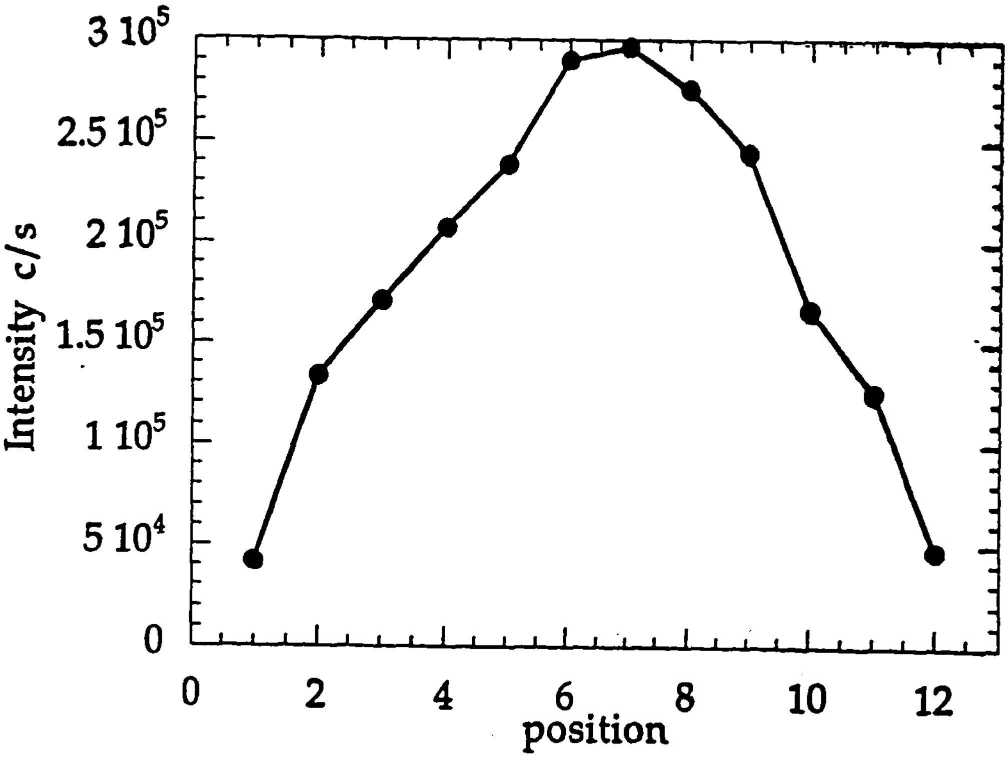

Figure 3.6. Optical Desity profile of absorption across the substrate plate

Figure 3.7. Prof. Derek M. Lindsay, and Dr. Robert Craig

Figure 3.8. Prof. John R. Lombardi, and Dr. Robert Craig

Chapter IV. Absorption, and Resonance Raman Spectroscopy of Mass-selected Transition Metal Clusters

4.1 COBALT DIMER, Co_2

An issue of considerable interest in any study of transiton metal bonding involves the extent of d-electron participation in metal-metal bonds[26,27]. The most important determinants of such interactions are (I) the relative sizes of the (n +1)s and the nd orbitals and (ii) the $(n+1)s^2nd^m$ - $(n+1)s^1nd^{m-1}$ atomic energy differences. Considering the position of Co between Fe and Ni in the periodic table, it is surprising that so little experimental information has been published on Co clusters.[28,29] A careful *ab initio* HF-CI calculation on the dimer of cobalt [32] predicts that the ground state is $^5\Sigma_g^+$ and that the d electrons participate only slightly in bonding The photoelectron spectroscopic results of Leopold and Lineberger [32] indicate on the other hand, that for Fe_2 and Co_2 the bonding is 3d-3d while in Ni_2 it is most likely 4s-4s.[33] Both experimental [32] and theorectical [33] results indicate that the trimer of nickel has weak if any d-electron contributions to bonding. Thus

Co has a pivitol position on the border between d and s bonding in the first row of the transiton metals. Determination of the structure and force constants in Co metal clusters would provide an invaluable guide for theory in this matter.

The Co_2 molecule was first observed by Kant and Strauss[28] who measured the Co_2^+/Co^+ ratios over liquid cobalt. From the ion intensity data, they dervied a dissociation energy using estimated molecular parameters.

Many excellent theorectical and experimental investigations of cobalt dimer have been carried out. In other matrix-isolation work, DiLella, Loewenschuss, and Moskovits have obtained a resonance Raman spectrum of Co_2.[29] On the basis of this spectrum the vibrational frequency of Co_2 is assigned to be $\omega_e'' = 290$ cm^{-1}.[29] In another study, an attempt to observe an ESR spectrum for Co_2 isolated in rare gas matrices failed to produce detectable Co_2 signals.[38]

The only other expermental data on Co_2 were obtained by photoelectron spectroscopy on Co_2- produced from $Co_2(CO)_8$ in a flowing afterglow ion source.[28] The electron affinities of Co and Co_2 were determined to be 0.662 ± 0.003 and 1.110 ± 0.008 eV, respectively. From these data we may conclude that Co_2- bond is 0.448 ± 0.011 eV more strongly than Co_2, in keeping with the general behavior expected for metal clusters as discussed in the previous subsection. Two intense band systems of Co_2 were observed in the photoelectron spectrum reported by Leopold and Lineberger.[29] The lower energy system produces Co_2 in its ground electronic state. A vibrational progression is observed with $\omega_e'' = 280 \pm 20$ cm^{-1}, which is consistent with the reported matrix-isolation value.[28] Hot bands arising form υ= 1 and υ= 2 level of Co_2^- determine the vibrational frequency of the anion to be $\omega_e'' = 240 \pm 15$ cm^{-1}, On the basis of the Frank-Condon intensity pattern observed, it is suggested that the bond length of Co_2^- exceeds the value for Co_2 by 0.08 ± 0.02 A.[27]

These results are in conflict with the expected model of chemical bonding in the heavier homonuclear dimers of the 3d transiton series. Apart from earlier extended Huckel,[45] restricted Hartree-Fock,[41] and preliminary local spin calcualtions[42] which are generally unreliable, the only calculation Co_2 is an all-electron, *ab initio* Hartree-Fock configuration calculation by Shim and Gingerich.[41] In this calculation, orbitals were optimized for the lowest energy configuration and used without further change in a configuration interaction calculation which allowed full reorganization within the 3d shells. All 84 states arising from the interaction of two $^4F(3d^8 4s^1)$ cobalt atoms were found to lie in an energy range within 0.42 eV of the ground state. The energies of these 84 electronic states, calculated for an internuclear separation of 2.50 A, a r_e given in Ref 28. The ground state itself was calculated to be $^5\Sigma_g^+$, arising from a $(3d\sigma_u)^{2.00}(3d\pi_u)^{3.09}(3d\delta_g)^{3.02}$ $(3d\pi_g)^{2.91}(3d\sigma_u)^{2.00}$ $(4s\sigma_g)^{1.94}$ $(4s\sigma_u)^{0.06}$ natural orbital occupation. The near equality of occupation number for the 3d bonding and antibonding orbitals indicates that these orbitals are essentially localized on the individual atoms, which are held together by a $(4s\sigma_g)^2$ bond. The values $r_e'' =$ 2.56 and $\omega_e'' = 162$ cm^{-1} are obtained for the $^5\Sigma_g^+$ ground state of Co_2.[29] This value for ω_e'' is considerably less than the value obtained in resonance Raman [26,27] and photoelectron spectroscopic[28] experiments. In additon, the dense manifold of low-lying electronic states is in conflict with the observed photoelectron spectra.

Earlier work on the absorption spectrum[29] was hampered by the apparent overlap of atomic and dimer bands in the ultraviolet spectrum. Mass separation of species unambiguous assignment of spectral features, and here we apply that technique to the study of Co and Ni species to examine bond trends in the first row transition metals.

Figure 4.1 shows a typical mass scan (ion energy approximately 350 eV) obtained by applying a (nonlinear) voltage ramp to the power supply controlling the Wien filter magnetic field. Although the mass scale can be estimated from the (approximately) known parameters of the Wien filter and the beam energy, we generally refine (as has been done in Figure 4.1) these scales using assigned cluster masses. Although not true for all metals, ion currents for sputtered cobalt clusters decrease monotonically with increasing cluster size. Under "soft-landing" conditions (deposition energy = 10eV), the measured ion currents were 100 nA for Co^+, 55 nA for Co_2^+ and 10 nA Co_3^+, i.e., somewhat lower than those shown. Fragmentation may be estimated by comparing the intensisties of atomic excitation freatures in a dimer of trimer depositon with those obtained from depositons of the atom under similar conditions. By this measure we estimate the fragmentation of cobalt dimers and trimers to be 15%-20% and 5%, respectively.

Matrix samples were interrogated insitu by adsorption, resonance Raman, and (in the case of atomic cobalt) excitation spectrscopy.

No strong dimer absorption bands were observed following a 265 nA-h depostion of dicoblat in argon. Indeed, the only clearly recognizable dimer feature between 250 and 900 nm was a weak, unstructured absorption (maximum at 440 nm) extending from 425 to 485 nm. This assignment to dicobalt is verified by the observation (see below) of resonance Raman spectra for excitation wavelengths (457.9-496.5 nm) in this region. Apparently, this feature corresponds to the 442 nm band previously reported by Ozin and Hanlan.[36] A second (approximately 60 nm wide) absorption was observed at around 335 nm, which is a little to the blue of the 340 nm dimer band found by the authors of Ref. 54. Superimposed on our 335 nm band was a sharp atomic absorption at 325 nm; another atomic feature is visible at 293 nm. In fact, the 335 nm region contains several atomic transitions. A group of relatively sharp absorptions occurs at 325.0, 332.5, 339.0, and 348 nm (as reported by Ozin and Hanlan)[36] and these were clearly evident in our excitation spectra of both atomic and dimer matrix samples. Since no Raman spectra were observed when exciting at 363.8 nm and since the dimer fragmentation (15%-20%, as noted above) was quite high, we feel that our spectra are inconclusive as regards the 335 nm feature.

Raman spectra were observed at six different excitation wavelengths between 457.9 nm and 496.5 nm, although spectra excited be the 465.8 nm ion laser line were most intense. Figure 4.3 shows a typical Raman spectrum(7 cm^{-1} resolution) for a 265 nA-h sample of dicobalt in argon. The dimer transition are labeled $\upsilon''=0-\upsilon''$; the (nonresonant) Raman line at 330 cm^{-1} arises from the CaF_2 support.[37] A strong background due to Rayleigh scattering has been subtracted out, and the features near 200 cm^{-1} may be an artifact of this background. The average Stokes shifts (which were further calibrated using the CaF_2 line) for six different excitation wavelengths are (one standard deviation uncertainty in parentheses): 291.1(17), 581.5(55), 860.5(81), 1146.6(53), and 1418.4(83)cm^{-1} for $\upsilon''=1$ to 5, respectively. These data give $\omega_e=296.8 \pm 5.4$ cm^{-1} with $\omega_e x_e=2.2 \pm 0.8$ cm^{-1}. The dimer frequency agrees within experimental error with the 280 $\pm$ 20 cm^{-1} value obtained fom photodetachment studies[27] and is also in accord with an unpublished Raman measurement[43] of 290 cm^{-1}.

Since the Raman measurements determine the dicobalt anharmonicity, the spectroscopic dissociation energy of the dimer can be estimaed from the Kratzer relationship, $D_e = \omega_e^2/4\omega_e x_e$, [39] which gives D_e=10,000 ± 3700 cm^{-1}. The thermodynamic dissociation energy, $D(Co_2)$, is lower than this value by approximately 3500 cm^{-1}, [28] since (as noted above) the dimer dissociates asymptotically to one ground ($3d^7 4s^2$) and one excited ($3d^8 4s^1$) state atom. Accordingly, the Raman data give $D(Co_2)$=6500 ± 3700 cm^{-1} in good accord with a "third law" measurement, $D(Co_2)$=7700 ± 2900 cm^{-1}.[26]

4.2 NICKEL DIMER, Ni_2

We have examined this molecule by absorption , and Resonance Raman spectroscopy. Interestingly enough, when mass selecting and depositing the molecule (see figure of Mass Scan, Figure 4.4), we found a current of about 200 nA-h, and a great deal of fragmentation, 25-30%, after examning the excitation spectra. This might be indicative of the s character in the bonding in this molecule. Also, we had to our advantage previous installed the Spex model 1877 triple-mate with the "Spectrum-One" CCD device. The detector being liquid nitrogen cooled, allowed us to resolve Ni_2 isotopically amoung those with the largest percentages, namely the 58, and 60 atomic isotopes (Figure 4.6).

Kant first confirmed the existence of Ni_2 by observing it mass spectrometrically in the vapor phase over liquid nickel at 2000-2200 K.[65] A second-law calculation from his data gave $D_0°(Ni_2) = 2.03 + 0.30$ eV, while the absolute entropy method gave $D_0°(Ni_2) = 2.36 \pm 0.22$ eV. Kant also determined the appearence potential of Ni_2^+ to be 6.4 ± 0.2 eV, from which one may dervive $D_0°(Ni_2^+) = 3.26 \pm 0.5$ eV. using the second-law value of $D_0°(Ni_2^+) = 3.30 \pm 0.2$ eV, indicating significantly stronger chemical bonding in Ni_2^+ than in Ni_2.

The electronic ground state according to Melius et. al for Ni_2 is:

$$1\delta^3{}_g 1\delta^3{}_u 1\pi^4{}_u 1\sigma^2{}_g 1\sigma^2{}_u 2\sigma^2{}_g$$

This configuration, however, produces many states which are degenerate[64]

Experimentally, Moskovits and Hulse[55] characterized the UV-visible spectra of diatomic, triatomic and higher nickel clusters in 1976. Also that year, Alfred B. Anderson at Yale theorectized the U.V. spectra for Ni_2 and Ni_3 in argon matrix. Moskovits and Dilella[36] then obtained resonance Raman spectra for Trinickel in Argon matrices, However, their samples were not mass selected, and instead grown by resistive vaporization of metal filament of the sample.

Even Recent studies using EXAFS on small metal clusters have reveled a strengthening in bonding of Ni-Ni and Cu-Cu metal clusters increase with cluster size. As evident from our mass scan data, (see Figure 4.4) ion currents, and thus possibly stabilty builds slowly with cluster size in Ni-Ni bonding.

Using two resonance photon ionization spectroscopy, Morse et. al. has investegated this molecule rotaional, and found excellent results when super cooling the sample in an Helium expansion.[24]

The absorption spectrum (SDS)of an approximately 200 nA-h sample of Ni_2 in argon shows two regions of absorption as may be seen in Figure 4.5. The 325 nm band actually actually consists fo four transitions which occur at 305.5, 316.6, 323.0 and 332.0 nm. Since the dimer fragmentation (25%-30%, as noted above) was high and since atomic nickel in argon absorbs at 303, 317, 321, and 329 nm[64], It is quite certain that these bands are due to fragmented dimers. The second band is very weak, continuous and centered at approximately 480 nm. This band arises from isolated nickel dimers. This assignement is verified by the observation (see Figure 4.6) of resonance Raman spectra for several excitation wavelengths in the range 457.9-496.5 nm. The plot of the dimer Raman intensity (scaled by laser power) vs. excitation wavelength shows a maximum Raman intensity at about 480 nm. This Raman excitation profile is superimposed in Figure 4.6 and nearly coincides with dimer absorption band thus confirming our assignment.

Furthermore, our dimer absorption feature is in agreement with previously reported measurements by De Vore et al.[56] and by Moskovits and Hulse.[55] The spectrum was assembled in two segments, but has a common ordinate scale. Transitions near 325 nm arise form atomic nickel. The weak band near 480 nm is assigned to the dimer. The dotted line (...) represents the background. The insert shows the Raman excitation profile (right-hand scale) of Ni_2 in an argon matrix.

Raman spectra were recorded using six different visible lines of an argon-ion laser. Figure 4.6 shows a typical spectrum. The principle features of the spectrum are a vibrational progresion (labeled $\upsilon''=0 \rightarrow \upsilon''=1,2,3$)and a nonresonant Raman transition from the CaF_2 substrate. The $\upsilon'=2$ and 3 components each have a triplet fine structure. Naturally occurring nickel has three important isotopes, ^{58}Ni (68.3%), ^{60}Ni (26.1%), and ^{62}Ni (3.6%),[57] and so the three components of each band in Figure 4.6 can readily be assigned to $^{58}Ni_2$, $^{58}Ni^{60}Ni$ and a combination of $^{60}Ni_2$ plus $^{58}Ni^{62}Ni$. Isotope shifts for the fundamental band ($\upsilon''=1$) were too small to be resolved. We were able to reproduce the fine structure of each Raman transition (see Table 4.2) using the expression[58]

$$\omega_{ij} = 1000\zeta\left[\frac{(M_i + M_j)}{0.58916 M_i M_j}\right]^{1/2} \qquad (6)$$

Where ξ=1.0714 is a constant determined by setting ω_e=259.2 cm^{-1} for $^{58}Ni_2$ and M_i, M_j are isotopic masses. We take this fit as an absolute confirmation of the assignement of this spectrum to the nickel dimer species.

In table 4.2, we list the average (one standard deviation in parentheses) of the Stokes shifts found for six different excitation wavelengths between 457.9 and 496.5 nm and those calculated using Eq (6). Using standard methods,[59] the Stokes shift data give ω_e=259.2(30) cm^{-1} with $\omega_e x_e$=1.9(7)cm^{-1} for $^{58}Ni_2$ in an argon matrix. The calculated frequencies for each isotope are listed in Table 4.2. Previous to this work, the only reported dinickel vibrational frequency was 280 ± 20 cm^{-1} obtained from photodetachement studies.[60] Although the Raman and photodetachemnt results nearly differ by more than their reported uncertainties, the dinickel photodetachment spectra are relatively congested. Accordingly, the two values for we should not be viewed as being in disagreement with each other.[61]

When we had previously compared the force constants of the "late," first row transition metal dimers, the relatively large error in the dinickel force constants we could not, at that time, preclude a transition following Ni_2 rather than after Co_2[51]. In light of the improved measurement for Ni_2, it is worthwhile comparing again experimental force constants for the series Fe_2,[62] Co_2,[54] Ni_2, and Cu_2.[63] As shown in Figure 4.7, there is an abrupt drop in this parameter between Co_2 and Ni_2. This observation suggest a concomitant change from some degree of *d-d* bonding in Fe_2 and Co_2 to little or no *d-d* bonding in Ni_2 and Cu_2 and confirms earlier theoretical predictions,[74] employing Hartree-Fock methods with extensive configuration interaction, that the chemical bonding in dinickel originates primarily from the interactions of the 4s orbitals on each Ni atom. In addition, recent ligand field calculations[75] indicate three low lying states (0^+_g, 0^-_u, and 5_u at 0, 12, and 58 cm^{-1}, respectively) all arising from a $3d^9_A 3d^9_B \sigma^2_g$ configuration.

Figure 4.7 also shows that the force constant for Ni_2 (1.16 mdyne/A) is even smaller than that for Cu_2 (1.33 mdyne/A). A careful rotational analysis of recent two photon ionization spectra[68] has shown that the ground state bond length of Ni_2 is somewhat shorter (by 0.0652 A) than that of Cu_2. Badger's rule would then imply that Ni_2 should have a larger force constant than Cu_2. However, several recent measurements suggest that Badger's rule may be violated more ofrten in transition metal dimers than in other molecules. For example, a Frank-condon analysis of the dirhenium absorption spectrum,[67] shows a decrease in internuclear distance on excitation from the ground (X) state to the A state, while the force constant also decreases. In a gas-phase rotational analysis of Nb_2, Hames and co-workers[68] found that the A and the E states have both larger force constants and inter-nuclear distances than the ground state, once again violating Badger's rule.

4.3 *TANTALUM Ta_2 "REVISITED"*

In the case of Ta, the first deposition and analysis of the experimental procedure in 1993 has been enhanced since then, and resonance Raman spectra taken from the Spex 1877 triple mate and the "Spectrum-One" CCD detector (cooled down to 133°C/140°C) greatly enhanced the spectra in many ways. As evidence of this is, I first show you Ta_2 resonance Raman spectra in an Argon matrix with a ground state progession to $v''= 4$ (Figure 4.8). The first Raman experiment was carried out with the Spex Double mate combined with a 943-02 Hammatsu PMT. Tantalum was used to focus our new Triple mate system at this point, since our system had provided reproducible results in the past with a resonable progression, and as this metal is inexpensive. Next, I would like you to observe Ta_2 resonance Raman spectra taken with the triple mate and the "Spectrum-One" CCD detector (Figure 4.11) with a Raman progression for this dimer out to $\upsilon''=14$.

For a complete discussion, let's start from the begining of the prior study. Again, an intense (typically 15 mA at 25 KeV) argon ion beam from the CORDIS ion source sputters tantalum cluster ions for a water cooled, tantalum target (Rembar, 99.9%) maintained at about

300 V. Cluster currents measured (after deceleration to 10 eV) on a Faraday plate in the depositon region were Ta^+ (50 nA), Ta_2^+ (40 nA), and Ta_3^+ (20 nA) (Figure 4.10).

Tantalum ions were codeposited (at about 14 K) with Ar and electrons on a polished CaF_2 substrate, and the matrices were grown at 5 m/h with an Ar:metal dilution ratio of approximately 10^4:1.

The kinetic energy distribution of the arriving ions was centered close to the target potential and had a full-width at height maximum (FWHM) of 10-20 eV. Suprisingly few tantalum dimers (neutral bond energy, 4 eV)[77] were fragmented by the depositon process. Although comparison of atomic and diatomic excitation spectra leads to an estimate that 0.5% of the tantalum dimers were fragmented, the actual value is probably even smaller. Thus, the atomic signal from fragmentation was comparable to that arising from the few (approximately 0.1%)[79] neutrals which manage to negotiate the 10° bend, as determined by experiments in which ions were prevented form reaching the depositon region by applying a suitable retarding potential. Interestingly, the depostion of dimer ions without electrons also led to a Raman spectrum, but this was approximately 10 times weaker (when scaled or equivalent conditions) than that obtained with electrons added. A similar result pertains to the depositon of the atomic ion.

For the absorption measurements we employed either a deuterium or a tungsten lamp, dispersed by a single 1/4 m monochromator (also calibrated with a Hg lamp), reflected off a plane mirror and then focused onto the matrix sample. The mirror is mounted on a computer controlled stepping motor, which allows the light to be scanned (in several steps) across the 8 mm wide sample. The absorption measurements were again made by collecting the light scattered at 90° to that incident. Prior to recording scattering depletion spectra, an optical density profile is obtained by recording single beam spectra as a function of lateral position on the sample (see Figure 3.6). It is generally found that the sample is non uniform, with about twice as much absorption in the center as compared to near an edge.

Figure 4.9 shows the absorption (scattering depletion) spectrum of Ta_2 in an Ar matrix at 14 K. The spectrum was obtained following a 5 h depositon of 42 nA of Ta_2^+ (210 nA H) (Ref. 79) at a depostion energy of 10 eV. Figure 4.9 was recorded in 3 segments. The portion between approximately 200 and 350 nm was recorded using a

Deuterium lamp, whereas a tungsten lamp was employed for the two remaining segments. In additon, a 1200 g/mm (250 nm blaze) grating was used between 200 and 500 nm, but the portion further to the red was recorded using an 1800 g/mm holographic grating. Each of the three segments was futher processed by subtracting "background spectrum" approximated as a locally straight line. Prior to this refinement, the scattering depletion specra are dominated by a broad background (peaking near 300 nm) which arises from wavelength dependent differences in the light collected from the signal and reference positions of the sample. All three segments in Figure 4.9 have the same ordinate scale, however. The maximum change in the referenece/signal ratio (i.e., at 480 nm) is about 0.1, which is significantly smaller than the found[75,76] for Nb_2 and Zr_2.

The absorption spectrum of Ta_2 in argon (Figure 4.8) consists of two weak features at 235 and 247 nm, a broad band centered near 300 nm, a relatively intense band with maximum absorption at 480 nm and two further weak absorptions around 600 and 640 nm). The possibility that the 600 nm band belongs to dimer ions cannot be ruled out, since weak absorptions in this region were also observed when Ta_2^+ was deposited without electrons. The 480 nm dimer band includes a poorly resolved vibrational progression, as indicated in the upper right hand panel of Figure 4.8.

The members of this progression were analyzed to give $\omega_o' = 260 \pm 15$ cm^{-1} with $T_o \leq 21{,}330 \pm 20$ cm^{-1}. The vibrational structure was less well defined after the sample was annealed to 25 K. Accordingly, the middle panel of Fig. 4.8 pertains to the unannealed sample.

The spectrum was recorded at 10 cm^{-1} resolution (200 m slits) with an acquisition time of 4s for each 5 cm^{-1} step with the Spex double-mate and Hammatsu PMT. The principal features of the Fig. 4.8 spectrum are a vibrational progression (labeled $\upsilon''=0\text{->}\upsilon\text{->}1$) and a Raman transiton from the CaF_2 support, whose 330 cm^{-1} frequency[85] was used to further calibrate the Raman data. The Raman spectrum is resonantly enhanced due to the dimer adsorption band at 480 nm, which conveniently overlaps the visible lines of a argon ion laser. Raman spectra were recorded at six different wavelengths between 454.5 and 488.0 nm. Some Raman transitions were not observed because of more intense atomic fluorescence features. The data was analyzed by standard methods to give $\omega_e'' = 300.2 \pm 1.2$ cm^{-1} and $\omega_e x_e'' = 1.2 \pm 0.2$ cm^{-1}.

Analysis of the date of the more recent study of lead us to possibly two different interpretations of the long Raman progression. Either (1) we have observed Raman progressions from 4 different sites within the argon matrix, or (2) have populated an excited state approximately 504 cm^{-1} above the ground state and observed its progression, (see Figure 4.8).

Apart from the results presented here, there have been no previous spectroscopic measurements on Ta_2. Indeed, very little is known (either experimentally or theorectically) about the properties of any of the third row transition metal dimers. However, inferences about the bonding in the lighter transition metal dimers might also be expected to remain applicable for elements of the third row. Thus, for example, a relatively strong bond (and concomitantly large force constant) is a notable characteriestic of many "early" (groups IIIB-VIIB) transition metal dimers. As discussed elsewhere, [77,86,87] chemical bond formation is most favorable in those instances where at least one of the interacting atomic moieties has an open s-shell configuration: s^1d^m as opposed to s^2d^{m-1}. If s^1d^m is not the ground state configuration, bonding can still take place but at the cost of a certain amount of promotional energy. The dimer bond strength is then largely dependent upon the amount of overlap between the atomic d orbitals, one determinant of which is the relativesize for the (n + 1)s and nd orbitals. Thus, for example, the ratio of expectation values <r4s>/<3d> is consistently much greater than <r5s>/<4d> and this is thought to contribute to the tendency for the 4d metals to form stronger bonds than the 3d elements. [77]

This trend in bond strength is reflected in a modest increase in force constant (given is parentheses in mdyne/A) between Ti_2 (2.35) (Ref. 88) and Zr_2 (2.51)(Ref.76) and from V_2 (4.33) (Ref. 79,88) to Nb_2 (4.84) (Ref.75,89); the change for the group VIB elements, Cr_2, (3.13) (Ref. 90) and Mo_2 (6.43) (Ref. 91), is much larger. Since the d orbital overlap is even more favorable for <r5s><r4d> (Ref. 87), it might be anticipated that Ta_2 should measurements determine a ditantalum force constant of 4.80(4) mdyne/A which (within experimental error) is the same as the 4.84(1) mdyne/A value for Nb_2. [75,89] A possible explanation may lie in the s-d promotion energy. Thus, although $6s^1 5d^4$ configuration lies 1 eV above $6s^2 5d^3$. Because the lanthanum series precedes Hf, the $s^1 d^m$ configuration energetically relatively remote for many third row elements. Accordingly, the force constants of other isovalent 4d and 5d dimer molecules may also be found to be similar in magnitude.

4.4 Tantalum Tetramer, Ta_4

In this analysis we have turned our attention to a larger cluster, namely the tetramer of Ta. In addition to questions as to the geometry of such clusters, it will also be of interest to determine the effect of bonding to multiple atoms on the magnitude of the stretching force constants.

One of the earliest tetramers to be investigated by Raman spectroscopy was that of phosophorus (P_4).[97] This was also supported by an infrared spectrum,[98] as well as electron diffraction,[99] and x-ray diffiraction.[100] The diffraction studies, coupled with the Raman data provided show that the structure of phosphorous tetramer is tetrahedral. Although no similar experimental results exist for Bi_4, by scaling the dimer force constans from phosophorous vibrational frequencies[101] have been predicted. However, earlier reports of a tetramer spectrum[102] have recently been shown to arise from , the trimer instead.[103] Silver tetramer has been presumed to be tetrahedral,[104] although no Raman spectra have yet been reported. The tetramer of Si had been studied with surface enhanced Raman spectroscopy (SERS),[105] and found instead to have a planar rhombus structure. An electron spin resonance study of matrix isolated Cr (Ref. 106) indicates either a trigonnally distorted tetrahedral Cr_4 or square-based pyramid Cr_5. It is with these results in mind that we turn to the tetramer of Ta which is the subject of this work. We have been able to deposit a sufficient quantity of Ta_4 to observe several broad optical transitions in which we have excited resonance Raman spectra. These spectra are suprisingly rich, involving three vibrational fundamentals. One of the progressions has a frequency alteration which suggest a weak Jahn-Teller coupling. This result implies that the ground electronic state is degenerate, reducing the likely structural possiblities to either square planar or tetrahedral. The former may be eliminated since the expected fundamental frequencies should be nearly equal, while for the latter we expect frequency ratios (2:SQR(2):1) almost exactly as observed. Our conclusion is that the tetramer of Ta falls into the category of molecules which are tetrahedral in geometry at least in the ground state. We also present evidence of considerable distortion form tetrahedral geometry in the two observed excited states.

The optical absorption (SDS) spectrum of Ta tetramer is shown in Figure 4.13. Only two broad transitons were observed, one (marked A) centered at 768 nm, and shaded slightly to the blue, and a second (B) more symmetrical peak at 532 nm. The red transiton displays weak structure with features at 13,020 cm^{-1}, 13,360 cm^{-1}, and 13,500 cm^{-1}. The spacing of approximately 240 cm^{-1} most likely corresponds to a vibration in the excited state. Due to the relative lack of features, it is difficult to say much as to the characterization of the nature of these bands at this point. However, analysis of Raman resonances will give us some clue as to their origin.

Resonance Raman spectra have been obtained by excitation into the blue band (B) were somewhat more extensive than those observed in the red band (A), but otherwise no significant difference between the spectra were obtained. We have varied the excitation wavelength extensively throughour both regions, and consequentlythe Raman shifts reported herein reperesent averages over approximately 50 separtae measurements, and with several different deposited samples. Typical Raman spectra are shown in Figure 4.13, where the excitation wavelength is 760.1 nm and Figure 4.14 with excitation at 538.4 nm. The Raman shifts observed are listed in Table 4.4. All the observed lines can be explained by assuming three fundamental frequencies. The highest frequency (**υ_1**) progression starts at 270.2(2) cm^{-1}. The intermediate fundamental (**υ_2**) occurs at 185.1(1) cm^{-1} and this has only one overtone at 372.5(2) cm^{-1}. Note that the ratio of frequencies (**υ_1/υ_2**) is 1.46, very close to 2:1, as would be expected for a tetrahedral geometry,[107] Further evidence for this interpretation will be given below, in which we obtain a value for **υ_3** to be 130.6(2) cm^{-1}. The ratio of (**υ_2/υ_3**) then is 1.42, once again close to 2:1 as expected for a tetrahedral molecule. Normal mode calculations for all other reasonable tetramer geometry indicate considerable deviations form these ratios. If the geometry is indeed tetrahedral we may assign υ_1 to the totally symmetric **a_1** vibration and **υ_3** to the doubly degenerate **e** vibration.

The third and lowest progression starts at 134.5(2) cm^{-1} for which a rather long progression up to n=8 is observed for excitation in the blue absorption. All the other band observed in the spectrum involve combinations of the two lowest progressions with this lowest progresion. The lowest progression actually displays an alteration of frequency separation between 135 cm^{-1} and 126 cm^{-1}, with a corresponding alteration in intensities. This is characteristic of a weak Jahn-Teller interaction, which would again indicate a high degree of symmetry for the molecule. Since this alternation occurs in an e vibration, we must fit consider wether the coupling is with an E or T electronic state. For T-e coupling, no splittings are expected. All levels are nearey shifted by a constant amount.[108] Thus, it is most likely that the ground state is of E electronic symmetry. For weak E-e Jahn-Teller coupling we expect the vibronic energy levels to be governed by the formula

$$E_{nlj} = \omega_e[n + 1 + 2\lambda (l^2 - j^2 - 3/4)], \qquad (7)$$

where n is the principal vibrational quantum number (n = 0,1,2,3,...) while l is the vibrational angular momentum (l = $n, n-2, \ldots, -n+2$), and j is the total vibronic angular momentum ($j = l \pm 1/2$). For a particular n the ($2n + 1$)-fold degeracy remains since the energy is independent of the sign of j. The parameter l is the Jahn-Teller coupling parameter. Since j is a good quantum number we expect the selection rules $\delta j=0$ to hold. The vibrational angular momentum quantum number l is not strictly a good quantum number, but in the case of weak coupling we expect $\Delta l = 0$

to be the most intense trasnsitions with $\delta l = +1$ to be somewhat weaker. This explains the intensity alternation observed. For the lowest state $(n,l,j) = (0, 0,1/2)$ we expect trasnitions to states with $j = 1/2$, and alternating values of $l = 0$ (for n even) and 1 (for *n* odd). Thus the expected Raman frequencies for transitons to states (*n*, 0 or 1, 1/2) are

$$\omega_{nlj} - \omega_e\{n + l(1-(-1)n\} \qquad (8)$$

Analysis of the frequencies observed gives a best fit for ω_e=130.6(2) cm^{-1} and λ_e = 0.017(2). The relatively small value for the latter parameter justifies the weak coupling assumption. It also indicates that any geometrical distortion from tetrahedral geometry will be slight.

Thus the resonance Raman spectrum of the Ta tetramer indicates that the ground state is of tethedral geometry with an electronic *E* Symmetry. There is weak Jahn-Teller coupling with the e vibration. Our spectra give no information as to the possible spin degeneracy. In fact, for the third row transition elements, we should expect such strong spin-orbit coupling as to entirely quench any Jahn-Teller effect. Our value of the Jahn-Teller coupling parameter is, of course, extremely small, indicating that spin-orbit quenching is not complete in this case.

As for the nature of the two excited eelctronic states observed, first it should be noted that electronic transitons form an *E* state are allowed only to vibronic *T* states. Thus, a possible interpretation of the 240 cm^{-1} progression observed in the red band is that of T vibronic symmetry. This could arise from a T electronic state coupled with an a_1 vibration, slightly less than the 270 cm^{-1} spacing of the a_1 vibration in the ground state. However, this interpretation does not explain why Raman transions are seen to vibraions of all three symmetries in the ground state. It is usually stated[107] that for resonance Raman spectroscopy, transitons to totally symmetric vibration are expected to dominate. In fact, this statement should be modified since it holds only when vibronic coupling is weak in both states involved. When, for instance, the ground state is vibronically nontotally symmetric, we should say instead that resonace Raman transitions are allowed to those states for which there is no overall change in vibronic symmetry. however, if there is strong vibronic mixing in the excited state, so that the syummetry is lowered, then transitons are allowed to those totally symmetric states(or states having the same symmetry as the ground state) using the point group of the state of *lower* symmetry.

the net result would be transitons allowed to several if not all ground species.

We have shown that the tetramer of Ta falls in the category of tetrahedral molecules, along with P. With the latter molecule, the ratios of observed ground state fundamentals deviates considerably from the ratios 2:2:1 expected[107] in the case of a central force field. However, electron and x-ray scattering data indicate tetramers of phosphorous are indeed tetrahedral, so that the assumption of central forces must be called into question. In order to properly fit the observed frequencies it is necessary to introduce off-diagonal (stretch-stretch interaction) elements into the force constants. The Tantalum spectrum comes a lot closer to the ratios predicted by a central force model. However, even in this case an accurate fit to the observed frequencies requires additon of a small interaction term to the force constant matrix.

The rather large magnitude of the tantalum dimer force constant (4.80 mdyn/A) indicates a large contribution of d-orbital character to the chemical bond. This is consistent with other third row transiton dimers which have been observed. However, for the tetramer we expect due to the fact that each atom is bonded to three others, the bond-bond streching force constant will be considerably decreased. In Table 4.5, we compare the dimer and tetramer force constants for several tetramers for which experiemental data exist.

Note that in all cases the reduction factor is 2-3. These may be compared to the scheme proposed by Ozin and McIntosh.[104] They propose that the reduction in force constant should be proportional to the increased number of bonds each atom is involved with. For tetrahedral geometry they expect a reduction of 1/3 on going from dimers to tetramers. This slightly underestimates the tetramer force constant in both cases. For the planar rhombus of Si, there are tow types of bonds, on the edge and across the short diagonal. A good fit to the experimentally observed frequencies is obtained with both being nearly equal. The predicted constant for the diagonal bond is slightly lower while that for the edge bonds is slightly higher. In fact, the predictions are all remarkably close, and we certainly consider this scheme to provide an excellent predictor of spectra. The slightly higher force constants observed as compared to those predicted could possibly be caused by slight decreases in bond lengths, and/or consequent increases in d-orbital participation in bonding on going form dimer to tetramer. In any case, the results presented here should provided a sensitve test or theoretical investigations of third row transition metal wave functions.

4.5 Zirconium Trimer, Zr_3

Several articles, both experimental and theorectical, have recently appeared concerning the structure and bonding in zirconium clusters. Theorectical predictions of the dimer ground state[109,110] indicate either a $^1\Sigma_g^+$ or $^1\Delta_g$ state, a result that is confirmed by experiment.[111] The remaining theorectical articles involve the trimer[112] and tetramer.[113]

The following are results of a Raman spectrocopic study of zirconium trimers in an argon matrix. Since our samples are quite thin, absorption spectra are hard to obtain. We have found that Raman excitation profiles often provide higher sensitivity. Although no visible absorption spectra of Zr_3 could be obtained, we have identified two optical transitions by scanning the visible region of Raman excitation. The Raman spectrum itself indicates that in the ground state, zirconium trimer is an equilateral (D_{3h}) geometry. Both the totally symmetric a'_1 and degenerate e' vibrations are observed.

Ziconium cluster ions were codeposited with Ar gas (99.9998% Ar, Matheson) from a coaxial injector ring and low-energy electrons in the usual way, and the mass-scan (figure 4.16) showed us measured ion currents were 81 nA for Zr^+, 76 nA for Zr_2^+, 15 nA for Zr_3^+, and 7 nA for Zr_4^+.

Fragmentation may be estimated by comparing the intensities of atomic excitation features in the trimer deposition with those obtained from depositions of the atom under similar conditions. By this measure, we may estimate the fragmentation of zirconium trimers to atoms to be less than 3%.

Despite repeated attempts in several deposited samples, no trace of an absorption or SDS spectrum could be observed. It is our conclusion that due to our optically thin samples, any visible transitions are too weak to be observed under these experiemtnal conditions. Such a circumstance presents some difficulty in obtaining resonance Raman spectra since it is not clear exactly where to begin. However, after searching at several excitation wavelengths, we were able to observe Raman spectra. A typical spectrum is shown in Figure 4.17, in which the excitation wavelength is chosen to be 608.2 nm. Three Raman lines may be ascribed to Zr_3; the remaining line at 330 cm^{-1} is due to the substrate CaF_2. Similar spectra were observed at numerous excitation wavelengths, over which we have averaged the observed lines. The averages, along with standard deviations (in parentheses) are 176.7(13) cm^{-1} (υ_2), 258.0(12) cm^{-1} (υ_1), and 516.1(8) cm^{-1}($2\upsilon_1$).

The (very weak) high-frequency line is almost exactly twice that of the most intense line, and we take it to be the first overtone. The ratio of the frequencies of the two lowest lines (υ_1/υ_2) is 1.46, which is very close to sqr(2). This is indicative of a symmetrical equilateral geometry (D_{3h}).[120] In such a case we expect two normal frequencies: one for a totally symmetric stretch of symmetry e′ (υ_2).

The Raman excitation profiles of the two lines int he region 450-650 nm are shown in figure 4.18, along with least squares fits of Gaussian bands. The profile of the $\upsilon_1(a_1')$ line shows two broad maxima: one near 491 nm and the other near 614 nm. The $\upsilon_2(e')$ profile, while somewhat noisier due to its lower intensity, shows a broad region of intensity near 614 nm, and is otherwise too weak to be reliably observed elsewhere.

The Raman spectrum of the zirconium trimer indicates clearly that the structure is most likely that of an equilateral triangle. Only two fundamentals are observed, and their ration is almost exactly that expected for D_{3h} geometry. The experimental bond force constant obtained from this analysis is 1.19 mdyne/A. This may be compared with that of the dimer,[111] which is 2.51 mdyne/A. Ozin and McIntosh[121] have suggested a scheme by which to predict the force constants of higher clusters from that of the dimer. They suggest that the reduction in force cosntant should be proportional to the increased number of bonds each atom is involved with. For an equilateral trimer this factor is 1/2, so that they would predict a trimer force constant of 1.26 mdyne/A, quite close to our measured value.

Additional information as to the nature of the ground and excited states may be obtained from an analysis of the Raman excitation profiles. these show evidence of two excited electronic states. The lack of a long progression is either vibration indicates that there is little change in geometry between ground and excited states. Note that the e′ vibration shows intensity only in the 614 nm region, while the 491 nm band is present only in the a'_1 vibrational profile. In D_{3h} symmetry we expect either singly or doubly degenerate electronic states. In the absence of vibronic coupling, resonance Raman spectra whould only be observed for totally symmetric ground state vibrations. The Jahn-teller theorem indicates that a doubly degenerate electronic state must necessarily couple with a vibrationof the same symmetry. We may conclude, therefore, that the 491 nm band lacks any measurable vibronic coupling, in either state, and must represent a transition between nondegenerate electronic states. The ground state is thus nondegenerate. On the contrary, since we observe intensity in the e′ vibration in the 614 nm region one of the two electronic states involved in this transition must be vibraonically couple. Since the ground state must be nondegenerate, the excited state must arise from a doubly degenerate electronic state.

It would be appropriate at this time to examine theorectical predictions as to the elctronic states available to the molecule. To our knowledge, only one paper has been published on the zirconium trimer by Dai and Balasubramanian.[112] In all, they examine the properties of 12 electronic states of Zr_3 by two methods. In the first, they utilize the complete active space multiconfiguration self-consistent field (CAS-MCSCF) and follow with muiltireference single and double configuration interaction (MRSDCI) calculations. Although both levels of calculation disagree as to the ordering of the states, the MRSDCI calculation is considered the more accurate treatment, and we have decide to focus on these results. The lowest lying states predicted by these calculations come from the following configurations:

Configuration	State (D_{3h})
$(1a'_1)^2(2a'_1)^2(1e')^4(1a''_1)^2(1a''_2)^2$	$^1A'_1$
$(1a'_1)^2(2a'_1)^2(1e')^4(1a''_1)^1(1a''_2)^1(2e'')^2$	$^3E''$, $^1E''$
$(1a'_1)^2(2a'_1)^2(1a''_2)^2(1a''_1)^2\ (1e')^3(2e'')^2$	$^5E''$

Dai and Balasubramanian predict the ground state to be the $^1A'_1$, and while the next states are predicted tot be split by Jahn-Teller interactions, their minima lie withing 0.73 eV of the predicted ground state. Further, they predict the ground state to be slightly distorted to C_{2v} geometry with an apex angle of 71.1°. In the limit of D_{3h} geometry our experimental results are in agreement with the theoretical results as to the nature of the ground state. In the limit of D_{3h} geometry our experimental results as to the nature of the ground state. If this assignement is indeed correct, considering D_{3h} selection rules, we may further assign the 614 nm band to be $^1A_1'-^1E'$ (x,y polarized), while the 491 nm band must be $^1A_1'-^1A''_2$. (z polarized). The short progressions observed justify the maintenance of D_{3h} notation in the excited states as well. Although these assignments must be viewed as tentative, it is hoped that they will provide a stimulus to further theoretical and experimental work on this molecule.

4.6 Niobium Trimer, Nb_3

The nature, importance and potential applications of metal clusters are issues attracting wide attention by a large number of investigations working in quite diverse areas of research. Diatomic metal molecules have been studied extensively by means of various experimental measurements and state-of-the-art calculations.[122,123] We now know force constants for the ground states of homonuclear transition metal diatomic species in a large portion of the periodic table.[124] Comparatively speaking, the studies of the properties of trimers and higher clusters are quite limited and still require more experimental and theoretical attention. In the case of niobium, several articles have addressed the bonding energies or ionization potentials (IPs) of larger niobium species, but little detailed information, especially regarding the structure and bonding of triniobium has emerged to date. Assuming that the $^6A_1$ state is the ground state of Nb_3 in C_{2v} geometry, Sellers[125] obtained ionization potentials[126,127] and some geometric parameters.

we report on the observation of resonance Raman spectra and absorption (scattering depletion) spectrum of Nb_3 in argon matrices. From the absorption spectrum three transition features of niobium trimer can be identified in the visible region. The resonance Raman spectra indicate that the ground state of the Nb_3 molecule is nearly an equilateral triangular geometry (D_{3h}). Both the totally symmetric a′ and degenerate e′ vibrations are observed.

Niobium trimer(or atomic) ions were co-deposited with argon gas and electrons onto a ~14K substrate, either CaF_2 or polished aluminum or silver plate. Ion currents under soft landing conditions could be measured on a Faraday plate in the deposition region and were: Nb^+(60nA), Nb_2^+(120nA), Nb_3^+(30nA) and Nb_4^+(15nA)(Figure 4.19). Prior to deposition, the selected ions were simultaneously slowed to 10eV by a surrounding "Faraday cage". In order to avoid interference from the CaF_2 Raman transition (at 330cm^{-1})[129] and obtain a better spectrum, we finally selected an aluminum substrate (held at the same potential as the Faraday cage). Matrices were grown at about 4~6μ/hour with an Ar:metal ratio of approximately 10^4:1. By comparing the intensities of known atomic excitation features in a trimer deposition with those obtained from depositions of the atom under similar conditions, the trimer fragmentation is estimated to be less than 0.6%(D_0=5.0eV).[122]

Figure 4.20 shows a "Scattering Depletion Spectrum"(SDS) of niobium trimers in argon matrix at 14K. The spectrum was obtained following the deposition of 100nA-hours of Nb_3 at an energy of 10eV and was recorded with 0.4nm resolution using a tungsten lamp. Three absorption features are shown with maxima at about 492nm (20,300cm^{-1};A), 532nm (18,800cm^{-1};B) and 587nm (17,000cm^{-1};C). No detectable absorption is observed beyond this region except one broad absorption band centered at 360nm (27,800cm^{-1}), which may be seen in the SDS spectrum (not shown) taken with a deuterium lamp. Annealing the sample to 36K had little effect on the absorption spectrum. By comparing the absorption features of triatomic niobium in argon with those obtained from the atomic and dimer niobium in argon,[130] we can attribute these transitions to niobium trimer with confidence. This assignment is verified by the observation of resonance Raman spectra for excitation into these bands. Further analysis is difficult due to the relative lack of features. However, analysis of Raman excitation profile will give us some clue as to their origin.

Resonance Raman spectra were observed throughout the region 458.5-614.0nm, but not upon excitation at 360nm band or further to the red. The progressions observed by excitation into the band A were somewhat more extensive than those observed in the other bands (B and C), but otherwise no significant difference between the spectra were obtained. Typical resonance Raman spectra of Nb_3 isolated in argon matrix are shown in Figure 4.21, where spectrum (a) is obtained excited with 514.5nm Ar^+ laser radiation; and spectrum (b) with 588.8nm dye laser radiation, respectively. The average Stokes shifts (one standard deviation in parentheses) found for over 60 different excitation wavelengths are listed in Table 4.6. All the observed Stokes lines can be explained by assuming two fundamental frequencies. The high frequency(ν_1) shows a progression ($v''=0 \rightarrow v''>0$) starting at 334.9(28) cm^{-1} and displays three overtones at 669.7(33), 1,003.8(28) and 1,340.6(62) cm^{-1}. The low fundamental frequency(ν_2) occurs at 227.4(29) cm^{-1} and has no overtone. The other bands observed in the spectra involve combinations of these two fundamentals.

The plot of Raman intensity (scaled by the laser power) vs. laser wavelength is superimposed in Figure 4.20. The Raman excitation profile of n_1 bears a strong resemblance to the triniobium absorption spectrum (Figure 4.20), but the peaks seem more closely spaced than the absorption spectrum. This pattern may be a result of interference effects observed in Raman excitation profiles.[133] Both the v_2 profile and first overtone of n_1 profile show an intense peak near the band A and a weak tail in the red region. Note that both n_1 and n_2 vibrations are observed with the same intensity near the peak A, while the n_1 vibration dominates the profile at the peak B. Neither display much intensity near the peak C.

The resonance Raman spectrum of niobium trimer in argon matrix shows two fundamentals at 334.9 and 227.4cm^{-1}. Further analysis of the line shape using least squares fitting of Gaussian function indicates that the widths of the 227.4 cm^{-1} line (Δn = 8.2 cm^{-1}) and other combination lines are almost twice that in the 334.9 cm^{-1} line (Δn = 4.5 cm^{-1}). Since the natural abundance of niobium is a single isotope (M=93) and we observe no effect on the line shape during annealing the sample to 36K, we might expect that the fundamental at 227.4cm^{-1} really consists of two unresolved lines, which are so close that they overlap to cause apparent broadening. Furthermore, notice the ratio of these two numbers is 1.47, very close to the ratio ($\sqrt{2}:1=1.41$) expected for an equilateral triangular geometry (D_{3h}).[132] Both observations suggest that the Nb_3 molecule is almost D_{3h} in shape with a possible slight distortion. In this case we assign the high frequency mode as the totally symmetric stretch $a'_1(n_1)$ and the low frequency to the doubly degenerate bend of symmetry $e'(n_2)$. A metal-metal force constant and a stretch-stretch interaction constant calculated by means of the Wilson FG method[134] assuming D_{3h} geometry give 1.95 and 0.05 mdyne/Å, respectively.

Sellers[125] has suggested a ground state of Nb_3 as the $^6A_1$ state in C_{2v} geometry because that state dissociates into fragments in their correct ground spin states. At the relativistic effective core potential-configuration interaction, single and double excitations(RECP-CISD) level, he obtains an ionization potential of 4.33eV which is somewhat smaller than the experimental results (IPs=5.6~5.8eV).[126,127] The optimum geometry is with an apical angle of 41.5°, far from our observations. The maximum experimental deviation of the apical angle from 60° (assuming the observed line widths are caused by slight deviations from D_{3h} geometry) is 1.7°.

Dai and Balasubramanian have recently reported the electronic structure of Zr trimer.[135] Since Nb has only one more electron than Zr, if we assume that the orbital ordering of Nb_3 is the same as Zr_3 in D_{3h} geometry, then the configuration of ground state is:

$$(1a'_1)^2(2a'_1)^2(1e')^4(1a''_2)^2(1a''_1)^2(2e')^3$$

containing a hole in the second e′ orbital and indicating a likely $^2E'$ ground state. This state is susceptible to Jahn-Teller distortion in the D_{3h} geometry. However, due to the short progression in e′ we see no conclusive evidence of Jahn-Teller interactions. The broader bandwidth in the e′ vibration stems from a possible slight splitting. In any case, we expect the Jahn-Teller coupling to be small due to probably strong spin-orbit coupling.

The absorption spectrum shows three electronic transitions. If the vibronic symmetry of the ground state is $^{ev}E'$, the vibronic selection rules are $^{ev}E' \rightarrow {}^{ev}E''$ (z polarized) and $^{ev}E' \rightarrow {}^{ev}A''_2$ (x,y polarized). Since the fundamental in the e′ vibration is observed in the A band (492 nm), this indicates substantial vibronic coupling in *one* of the states involved in transition. In this band we also observe a long progression in a'_1 vibration which indicates that the excited state probably has a large difference in internuclear distance from ground state and therefore is of somewhat different orbital character. In the 532nm region the intensity of the e′ vibration is substantially reduced with a shorter progression in the a'_1 vibration. In this case we infer that the excited and ground state will have similar orbital character and geometry. As to the 587nm band, it is difficult to assess its character because neither a'_1 nor e′ displays much intensity in this region.

4.7 Rhodium Dimer, Rh_2

Rhodium metal is quite important as a catalyst in many processes. Despite this fact, relatively little is known experimentally about the properties of small metal clusters[136,137,136] of this material, although there are numerous theoretical calculations on the dimer of rhodium. Shim [139] carried out the first *ab initio* plus CI calculation, while Balasubramanian and Liao[140] conducted a complete active space SCF calculation followed by a multi-reference configuration interaction calculation including spin-orbit interactions. Illas *et. al.*[141] carried out studies utilizing a set of nonempirical relativistic pseudopotentials and a rather large basis set with *f*-orbitals. More recently density functional theory has been applied by Harada and Dexpert[142]. Cocke and Gingerich[143] obtained a thermodynamic value for D_e by using third law methods. Of interest here are values for the ground state vibrational frequency ω_e as well as $\omega_e x_e$ from which we can determine a value for the dissociation constant. In the theories mentioned above predicted values of ω_e ranged from 118 cm^{-1} to 267 cm^{-1} while D_e has been reported to be anywhere from 0.25 eV to 2.92 eV. In order to resolve these questions, an experiment is clearly in order.

We are now pleased to report on the observation of resonance Raman spectra and absorption (scattering depletion) spectrum of Rh_2 in argon matrices. Our samples are prepared by neutralizing a mass-selected beam of dimer ion, and therefore there is little or no interference between the spectroscopic transitions of the dimer and those from atom and trimer. This allows unambiguous assignment of spectral features. From the absorption spectrum only a single transition of rhodium dimer can be identified in the visible region with a broad band observed at 480 nm. By resonance excitation into this band with the 514 nm line of an Argon ion laser, we obtain a sharp progression of Raman vibrational lines up to $\upsilon = 3$. The resulting value for ω_e is 284.3(14) cm^{-1} and for D_e is 1.2 (2) eV.

Ion currents under soft landing conditions could be measured on a Faraday plate in the deposition region and were: Rh^+(70nA), $Rh2^+$(13nA), and $Rh3^+$(12nA). Prior to deposition, the selected ions were simultaneously slowed to 10eV by a surrounding "Faraday cage". Matrices were grown at about 4~6μ/hour with an Ar:metal ratio of approximately 10^4:1. By comparing the intensities of known atomic excitation features in a dimer deposition with those obtained from depositions of the atom under similar conditions, the dimer fragmentation is estimated to be less than 1%.

Matrix samples were interrogated *in situ* using both absorption and Raman spectroscopy. As previously reported[145,146] the absorption measurements were made by collecting the light at 90° to that incident, a technique we term "Scattering Depletion Spectroscopy" (SDS).

Raman spectra were recorded using the visible line of an argon ion laser (Spectra Physics model 2045) at 514 nm. Scattered light was collected at 90° into a Spex 1877E 0.6m Triplemate Spectrometer and detected by a liquid nitrogen cooled CCD detector (Spex model "Spectrum One") with DM3000R software.

Figure 4.23 shows a "Scattering Depletion Spectrum" of rhodium dimers in argon matrix at 14K. The spectrum was obtained following the deposition of 50 nA-hours of Rh_2 at an energy of 10 eV and was recorded with 0.4 nm resolution using a tungsten lamp. Only one absorption feature is shown with maximum at about 480nm. Annealing the sample to 36K had little effect on the absorption spectrum. By comparing the absorption features of diatomic rhodium in argon with those obtained from the atom in argon[146,147] we can attribute these transitions to rhodium dimer with confidence. This assignment is verified by the observation of resonance Raman spectra for excitation into this band.

Resonance Raman spectra were observed by excitation with the 514 nm line of an Argon ion laser, and a typical scan is shown in figure 4.23. Due to the high cost of Rh metal, only one dimer deposition was made, contrary to our usual practice. However several independent scans of the spectrum were carried out at different points on the sample plate. The average of 8 separate scans produce lines at 281.0(15) cm^{-1}, 556.0 (18)cm^{-1}, 827.4 (22)cm^{-1}, and 1097.0(23) cm^{-1}. We report one standard deviation of each measurement in parentheses. These clearly can be assigned to the $\upsilon = 0$ through $\upsilon = 3$ components of a progression in the single ground state vibrational frequency of rhodium dimer. Analysis of these lines by standard techniques[13] results in a determination of $\omega_e = 283.9$ (18) cm^{-1} with $\omega_e x_e = 1.83$ (33) cm^{-1}. Utilizing the expression[148] for $D_e = \omega_e^2/4\omega_e x_e$ we determine an experimental dissociation energy of 1.4(3) eV.

Our results do not shed any light directly on the spin or orbital nature of the ground state of rhodium dimer. However, they do represent the first unambiguous experimental determination of ω_e and D_e. It is therefore worthwhile to discuss our results in the light of the widely disparate results of the various calculations reported. We have summarized these in table 4.7.

The largest value reported for the dissociation energy is 2.92 eV by Cocke and Gingerich[143], who utilized a rather complex third law calculation to analyze their high temperature Knudsen effusion mass spectrometric results. This work involves measuring the appearance potentials of various ions, and determining the temperature dependence of the equilibrium constant K_p for a series of related reactions of Rh with graphite, resulting in a determination of the enthalpy for the reaction $Rh_2 = 2Rh$. Typical temperatures were on the order of 2500K, which is equivalent to a kT of 0.2 eV. At thermal equilibrium, therefore, numerous states of both the dimer and atoms will be populated. It is difficult to interpret the exact meaning of their measurement under these circumstances, except to say that it most likely represents an average dissociation energy of numerous low lying electronic states of the dimer. In this case it might be best regarded as an upper limit to the correct ground state dissociation energy. By contrast, our measurements were carried out at 10K, and there is no doubt that we are viewing the ground state of the dimer.

The remainder of the results in table 4.7 represent several quantum mechanical calculations, with varying degrees of sophistication. It is first striking that there is almost total disagreement as to the assignment of the nature of the ground state. Most researchers seem to agree that the ground state is of quintuplet spin degeneracy, but Σ_g^+ , Δ_g , and Δ_u are all separately suggested as candidates for the orbital state. This difficulty is due to the open shell nature of the configurations involved, stemming from Rh($4d^8 5s^1$; $^4F_{9/2}$) as well as other spin-orbit components within 0.3 eV. The excited Rh($4d^9$; ^2D) atomic configuration is only 0.34 eV above the former. Correlation with dissociation to two ^4F atomic states alone predicts 112 low lying molecular states before spin-orbit effects are taken into account. Thus we might anticipate considerable difficulty in determining the properties of the ground state of Rh_2 even with recent advances in computational abilities.

The calculations of Shim[139] were carried out using SCF/CI leading to a $^5\Sigma_g^+$ with the dominant configuration of $\pi_u^3\delta_g^3\delta_u^3\pi_g^3$. Both ω_e (118 cm^{-1}) and D_e (0.85 eV) are very small by comparison with our results here. Given the limited nature of this calculation, it is not expected that very accurate results can be obtained. Somewhat better results were obtained by Harada and Dexpert[142] who utilized density functional theory using an all-electron Gaussian basis set for three different multiplicities, as well as employing a relativistic effective core potential (ECP) with non-local corrections. These calculations make a good case for the quintuplet nature of the ground state. For the quintuplet calculations, a vastly improved ω_e (191 cm^{-1}) is obtained, though this is still considerably lower than the experimental result. This is most likely due to the lack of inclusion of relativistic corrections in the density functional theory. Presumably, effective core potentials were added with the intent of correcting for lack of relativistic terms. However, this modification results in almost no change in the value for vibrational frequency. The density functional value for D_e (2.09 eV) is somewhat larger than the experimental result though the inclusion of the effective core potential reduces the value of this parameter to 1.32 eV. The use of an effective core potential usually tends to lower the dissociation energy, since correlation effects cannot be adequately calculated with elimination of nodal structure in the effective core. Despite the excellent agreement with experiment for D_e for the ECP calculation, the rather poor determination of ω_e, which should actually be more accurately determined, suggests that the agreement of the calculated value for D_e may be fortuitous.

The best agreement for a value of ω_e between theory and experiment is perhaps provided by the calculations of Balasubramanian and Liao[140]. They carry out a complete active space multireference configuration interaction calculation on 36 electronic states including spin-orbit coupling. They employ relativistic effective core potentials retaining the outer nine electrons on each atom for the active space. A total of 105,000 configurations with single and double excitations were employed. The predicted ground state is $^5\Delta_g$ (4_g), which after spin-orbit effects are included lies 336 cm^{-1} below the first excited (3_g) state. The leading configuration for this calculation is $1\sigma_g^2 2\sigma_g^2 1\sigma_u \delta_g^4 \delta_u^3 \pi_g^2 \pi_u^4$ with an approximate bond order of 3. This differs from that of Shim[139] in that one electron is moved each from the antibonding π_g and σ_u orbitals to the more bonding π_u and δ_g orbitals, resulting in an increased bond order, and presumably increased ω_e, as well as D_e. This CASSCF calculation produces the best theoretical value of ω_e (267 cm^{-1}), very close to the experimental value, and D_e of 2.1 eV. This is somewhat larger than the experimental result. Their value of D_e was obtained by taking the difference between the calculated energy at a separation and that of the equilibrium internuclear distance (2.28 A). However, Illas *et. al.*[141] are critical of this approach. Using *ab initio* CI methods, and including only states correlating directly to the atomic grounds states, they determine a ground state of $^5\Delta_u$ in contrast to the g symmetry of Balasubramanian and Liao. They find several low lying electronic states dissociating to the ground state of the isolated atoms which were not included by the latter authors and, further, they note that their (Balasubramanian and Liao) leading configuration does not dissociate to the atomic ground state (^4F). Illas *et. al.* suggest that as the internuclear distance increases, the leading configuration of Balasubramanian and Liao will change to one with the correct dissociation products. However, their own values for ω_e (238 cm^{-1}) deviates substantially from that determined here. This may be due to the lack of static correlation. Their atomic integrals were obtained using a mono-configurational calculation, as opposed to the multi-reference CASSCF calculation of Balasubramanian and Liao. The value of Illas *et.al.* for D_e (1.5 eV), however, is quite close to the experimental result. Once again, in view of the poor value for ω_e obtained in these calculations, this may also be fortuitous.

It is also possible that the ground state of Rh_2 does indeed dissociate into excited states of the atoms. We have observed this previously for Re_2[149].In this latter experiment we were aided by an extensive, and sharp absorption spectrum which enabled us to determine dissociation energies for several states. However, the preference of transition metals for bonding with ns^1 configurations suggests most likely that Rh_2 will dissociate to ^4F atoms. In any case, if Rh_2 dissociates to excited atoms, the fairly accurate ω_e of Balasubramanian and Liao, despite the limitations, may still represent the best extant theoretical description of the ground state. Our experimental results involve a vibrational frequency and therefore force constant which is greater than those suggested by *all* the quantum theories. This suggests a bond order even greater than 3, and that d orbital contributions are somewhat greater than those invoked in the theories so far. It is clear that further theoretical work is called for.

4.8 Ruthenium dimer, Ru_2

Besides metals late in the periodic table being of interest for their catalytic properties, Ruthenium is of special importance since several complexes of this metal have been implicated in the cleavage of water and thus efficient conversion of solar energy into chemical energy by photoinduced electron transfer.[150]

Surprisingly, little work has been carried out on Ru_2. Miedma and Gingerich[151] estimated D_e from a relationship with the heat of vaporization and surface energy of the pure solid. Several quantum mechanical wave function calculations have been carried out. The earliest was an all-electron *ab initio* SCF-CI claculation by Coton and Shim.[152] Das and Balasubramanian used the complete active space multiconfiguration SCF mehtod, while there have also been several density functional calculation[154,155,156]. Common to all these calculations is the assignment of the ground state as $^7\Delta_u$ state. However, the calculated values for ω_e as well as D_e vary considerably among the several reports.

The mass scan, (figure 4.24) shows that ion curents under soft-landing conditions were: Ru^+(75 nA), Ru_2^+(26 nA), and Ru_3^+(24 nA). By comparing the intensities of known atomic features in a dimer deposition with those obtained from depositions of the atom under similar conditions, the dimer fragmentation is estimated to be less than 1%.

The "scattering depletion" (absorption) spectrum is an insert shown in figure 4.25. It consistsof a single broad transition centered about 470 nm. No other features attribute to Ru_2 are observed.

The resonance Raman spectrum of Ru_2 excited at 458.7 nm is shown in figure 4.25. A line due to the CaF_2 substrate is also in evidence. The spectrum consists of a single progression of almost equally spaced lines each accompanied by a weak side-band to higher frequencies. The lines may be assigned to the 0-n (n=1,5) vibrational transitions. Averaging over eighteen separate apectra taken at various excitation wavelengths (between 458 and 497 nm) we obtain mean line positions of lines at 343.8(26) cm^{-1}, 681.6(32) cm^{-1}, 1017.5 (26) cm^{-1}, 1,350.2(25) cm^{-1} and 1,678.9(8) cm^{-1}. Using standard techniques of analysis[159], we obtain ω_e=347.1 (9) cm^{-1} with $\omega_e x_e$=1.85(15) cm^{-1}.(dimer content = 120 nA-h).

The natural abundance of the isotopes of Ru involve masses of 96, 98, 99, 100, 101, 102, 104 amu. The most abundant, 102 is only present as 31.6%. The resulting isotope distribution contributes to slight broadening of the spectral lines, which becomes more pronounced in the higher overtones. Assuming a common force constant (and linewidth) for all the possible dimers, we may simulate the effect on lineshape. In figure 4.26 we illustrate the result of including 28 isotopes, comparing the result with the observed spectrum for 0-4 transition. These fits increase our confidence in our analysis, and allow more accuracy in line positions. They further show that the observed side-bands are definitely not due to isotope effects.

In order to eliminate the possibility that the sidebands were due to site effects, we carried out an annealing experiment, raising the temperature of the sample gradually from 14K to 35K, and lowering it back down again. The side-bands did not disappear, but the relative intensity of the sharp peaks to the sidebands shanged in a reproducible manner. This behavior is characteristic of phonon interactions, where the sharp peak is the zero phonon line and the side-band represents energy exchange with the lattice. As a test of this, we measured the integrated intensity of the zero phonon line (I_z) and the total intensity (I_t) as a function of temperature (T). The relationship is [160].

$$\mathrm{In}\ (I_z/I_t) - -S[1 + 6.6(T/\Theta_d)^2] \qquad (9)$$

where, Θ_d is the Dedye temperature of the solid (assumed to be 92 K, as pertains to crystalline argon)[161], which for Ar is 92 K, and **S** is the Huang-Rhys factor[17] which measures the phonon coupling strength. If $S \leq 1$ the coupling is said to be "weak", whereas if $S \geq 10$ the coupling is "strong". The areas of the principal and sideband peaks were determined by fitting simulated Lorentzian functions (one for each peak) to the first four Strokes transitions recorded at 13.5 K. A fit to Eqn. (9) gives S = 0.08 (3), 0.14 (3), 0.39 (6) and 0.69 (12) for the 0-1 through 0-4 transitions, respectively. Thus in all cases there is a weak coupling between the dimer and the matrix.

In the experiment we have measured ω_e and $\omega_e x_e$ which enables us to determine the dimer force constant (k = 3.59 (2) mdyne/A) and, from the Kratzer relationship ($D_e = \omega_e^2/4\omega_e x_e$), [162] to predict the spectroscopic dissociation energy, D_e = 2.0(2) eV. There are some well known difficulties in using this formual to determine dissociation energies[165], leading to the possibility that s-s bonds have differing dissociation rates from those of d-d bonds, leading to potentials which deviate somewhat from the Morse potential. While we have no evidence for such a distortion in Ru_2 the possibility remains that a distortion may be detected on examination of levels higher than those observed here. In Table 4.9 we compare several calculated harmonic frequencies and dissociation energies with our measurements. All calculations (except, possibly, those of ref. 154) predict a $^7\Delta u$ ground state arising from $1\sigma^2_g 1\pi_u^4 1\delta_g^3 2\sigma_g^2 1\delta^2_u 1\pi_g^2 1\sigma_u$ (or predominately, in the case of multiconfiguration calculations). There is much less agreement both among the various calculated (or empirical) ω_e and D_e and between these data and our experimental values. The only calculation which give a dissociation energy close to the spectroscopic value are those of Das and Balasubramanian.[153] Their calculated ω_e is about 20% too low, however. The remaining D_e values in Table 4.9 are at best within 30% of our result. The authors of Ref. 154 note that Local-Spin-Density (LSD) calculations typically over estimate transition metal dimer dissociation energies by approximately 0.5 eV. In this case, the LSD result could be considered as being in resonable agreement with experiment. The LSD ω_e is within 10% of that measured, as is the value calculated by Goursot et. al[156]. Chen, Krasowski and Fitzgerald[155] obtain $\omega_e = 335\ \text{cm}^{-1}$, which is almost identical with the experiemtnal value of 347 cm^{-1}. However, a sampling of their calculations (Table II of ref. 155) for other dimers we have interogated (Ni_2 or Rh_2, for example) raises the possibility that the agreement in the case of Ru_2 migtht be fortuitous.

Figure 4.27 compares the force constants obtained for the series Ru_2, Rh_2, Pd_2, [166] and Ag_2, [167] along with the corresponding data for the first row series Fe_2 -> Cu_2. In the latter case, a small but decided break is evident between Co_2 and Ni_2 which was interpreted as indicating the point at which d-orbital participation in chemical binding substantially decreases. No such break is obrserved for Ru_2 -> Ag_2. Instead, k declines smoothly from Ru_2 through Pd_2 and Ag_2. Thus, apparently, the participation of d-electrons in bonding also declines monotonically and smoothly in this row. The closeness of the Pd_2 force constant to that of Ag_2 probably arises because atomic Pd has a $4d^{10}$ ground state configuration. Since two interacting $4d^{10}$ atoms will lead to a van der Waals bond, the bonding in Pd_2 undoubtedly results from the interaction of two Pd atoms at least one of which has been promoted to $4d^9 5s^1$. The resulting dimer ground state is generally thought to be $^3\Sigma_u^+$ arising from a $(4d^{19})4d\delta_u 5s\sigma_g$ configuration. [166] For this situation, Pd_2 has a formal bond order of unity i.e. the same as in Ag_2. 169 Of all the late transition metal dimers measured so far, Ru_2 has the highest observed force constant. In fact, the force constant for Ru_2 (3.59 mdyne/A) is almost three times that of Ag_2 (1.18 mdyne/A)[167] which is consistent with Pauling's rule [168] as Ag_2 has a single bond whereas the most likely ground state configuration for the ruthenium dimer ($1\sigma^2{}_g 1\pi_u{}^4 1\delta_g{}^3 2\sigma_g{}^2 1\delta^2{}_u 1\pi_g{}^2 1\sigma_u$) has a formal bond order of 3.[166]

Table 4.1 Characteristics of Homo Nuclear Diatomic Metal Clusters.

element	mass (amu)	frequency (cm-1)	± σ (cm-1)	k (mdyne/Å)	± σ (mdyne/Å)
Sc	44.9560	238.90		0.756	
Y	88.9050				
La	138.9100				
Ti	47.9000	407.90		2.348	
Zr	91.2200	305.70	3.50	2.511	0.058
Hf	178.4900	176.20	2.60	1.632	0.048
V	50.9420	536.90	1.10	4.326	0.018
Nb	92.9060	420.50	0.50	4.840	0.012
Ta	180.9480	300.20	1.20	4.804	0.038
Cr	51.9960	479.00	2.00	3.515	0.029
Mo	95.9400	477.10		6.433	
W	183.8500	336.80	0.70	6.144	0.026
Mn	54.9380	76.40		0.094	
Tc	99.0000				
Re	186.2000	337.90	4.70	6.263	0.174
Fe	55.8470	299.50		1.476	
Ru	101.0700	346.40	1.10	3.573	0.023
Os	190.2000				
Co	58.9332	296.80	5.40	1.529	0.056
Rh	102.9050	283.90	1.80	2.443	0.031
Ir	192.2000				
Ni	58.7100	259.20	3.00	1.162	0.027
Pd	106.4000	210.00	10.00	1.382	0.132
Pt	195.0900	215.00	15.00	2.657	0.371
Cu	63.5400	266.43		1.329	
Ag	107.8700	192.40			
Au	196.9670	190.90		2.115	
Zn	65.3700	25.70	0.20	0.0127	0.0002
Cd	112.4000	22.90	0.20	0.0174	0.0003
Hg	200.5900	18.50	0.50	0.0202	0.0011

Table 4.2 Raman frequency shifts and ground state constants (cm^{-1}) for Nickel dimers and their dominant isotopes in an argon matrix. Estimated errors (1 standard deviation) in parenthesis.

	$^{58}Ni_2$		$^{58}Ni\ ^{60}Ni$		$^{60}Ni_2$	
ω_e observed	259.2 [a] (30)					
ω_e calculated	259.3 [a]		257.0 [d]		254.8 [d]	
v"	obs. [b]	cal. [c]	obs. [b]	cal. [e]	obs. [b]	calc. [e]
1	256.3(21)	255.5		253.0		251.0
2	506.5(15)	507.3	502.5 (15)	503.0	498.9(20)	498.6
3	755.4(15)	755.4	749.1(21)	748.9	743.1(21)	742.3

a. Using obs. or calc. Stokes shifts and $G(v+1/2) = \omega_e v - 2\omega_e x_e(v''+1)$

b. Average Stokes shifts from 6 laser frequencies.

c. Using $\omega_e = 259.2\ (30)$ cm-1 with $\omega_e x_e = 1.9\ (7)$ cm-1.

d. Using Eqn (1) in text with $\xi = 1.0714$.

e. Using " ω_e calculated " with $\omega_e x_e = 1.9\ (7)$ cm-1.

Table 4.3 Raman frequency shifts (cm^{-1}) for ditantalum in argon matrix.

λ_{ex} (nm)	$\upsilon'' = 1$	$\upsilon'' = 2$	$\upsilon'' = 3$	$\upsilon'' = 4$	$\upsilon'' = 5$	$\upsilon'' = 6$
454.5	301.6	592.7	885.1	1178.3	1463.4	1749.0
457.9	296.0	586.0	885.7	1171.5	1466.2	1750.0
465.8	295.5	594.5	883.9	1179.0	1463.3	
472.7	299.5	588.3	885.7	1172.0		
476.5	301.5	598.1	886.4		1464.5	
488.0	300.3	593.6		1179.0		
Mean (σ)	299.1(27)	592.2(44)	885.4(9)	1176.0(39)	1464.3(14)	1749.5(7)

Table 4.4. Observed resonance Raman transitions (in cm^{-1}) and assignments for the Tetramer of Tantalum.

Band	$\nu_3(e)$	$\nu_2(t)$	$\nu_1(a_1)$
134.5(2)	1		
185.1(1)		1	
260.1(1)	2		
270.2(2)			1
372.5(2)		2	
395.5(1)	3		
447.4(1)	2	1	
521.6(1)	4		
530.9(1)	2		1
581.8(1)	3	1	
656.9(1)	5		
709.0(2)	4	1	
783.6(1)	6		
791.5(1)	4		1
918.2(1)	7		
970.8(1)	6	1	
1045.0(1)	8		
1052.4(1)	6		1
1232.4(1)	8	1	

Table 4.5. Comparison of the force constants (mdyne/A) for dimers and tetramers of several species. P and Ta tetramers are tetrahedral, while Si is a planar rhombus. These are compared with those predicted by utilization of the force field of Ozin and McIntosh.

Element	Dimer force constant	Tetramer force constants	
		Observed	Predicted(Ref.13)
P	5.56	2.07	1.85
Ta	4.80	1.89	1.60
Si(planar)	4.65	1.65 1.65	1.86(edge) 1.55(diagonal)

Table 4.6. Observed resonance Raman transitions(in cm^{-1}) and assignments for the niobium trimer in argon matrix.

Band	$v_1(a_1')$	$v_2(e')$
227.4(29)		1
334.9(28)	1	
561.1(28)	1	1
669.7(33)	2	
895.9(45)	2	1
1003.8(28)	3	
1340.6(62)	4	

Table 4.7. Summary of numerous theoretical determinations of ω_e and D_e for the ground state of rhodium dimer. These should be compared to our experimental values of 284.3 cm^{-1} and 1.2 eV respectively.

Authors(Ref)	Method	Ground State	ω_e (cm^{-1})	D_e(eV)
Shim(139)	SCF/CI	$^5\Sigma_g^+$	118	0.85
Balasubramanian,Liao(140)	MCSCF(CASSCF)	$^5\Delta_g$ (4_g)	267	2.1
Illas, Rubio,	*ab initio*	$^5\Delta_u$	238	1.5
Cahellas,Ricart(141)	Gaussian, density funct	singlet	245	0.25
Harada, Dexpert(142)	Gaussian, density funct	triplet	186	1.86
"	Gaussian, density funct	quintuplet	191	2.09
"	Effective core potentials	quintuplet	204	1.32
"	Third law	-	-	2.92
Cocke, Gingerich(143)				

Table 4.8. Observed resonance Raman transitions (in cm^{-1}) and assignments for the ruthenium dimer.

Measured							Calibrated with -0.78nm						
	Raman shift (cm-1)							Raman shift (cm-1)					
nm	CaF2	0-1	0-2	0-3	0-4	0-5	nm	CaF2	0-1	0-2	0-3	0-4	0-5
477.12	333	346.0	685	1017	1345		476.34	334.1	347.1	687.2	1020.3	1349.3	
477.12	333	346.0	682	1017	1348		476.34	334.1	347.1	684.2	1020.3	1352.3	
488.74	329	342.0	678	1014			487.96	330.0	343.1	680.1	1017.2		
488.74	329	342.0	678	1017			487.96	330.0	343.1	680.1	1020.2		
497.22	333	346.0	681	1016			496.44	334.0	347.1	683.1	1019.1		
497.22	333	346.0	683	1012			496.44	334.0	347.1	685.1	1015.1		
458.74	330	343.0	679	1016	1343	1674	457.96	331.1	344.2	681.3	1019.4	1347.4	1679.5
458.74	329	343.0	675	1011	1342		457.96	330.1	344.2	677.3	1014.4	1346.4	
515.38	327.6	340.0	683				514.60	328.6	341.0	685.0			
515.38	327.6	340.0					514.60	328.6	341.0				
502.72	327	340.0	676	1017			501.94	328.0	341.0	678.1	1020.1		
502.72	327	340.0	677	1010	1348		501.94	328.0	341.0	679.1	1013.1	1352.1	
528.72	327	342.0					527.94	328.0	343.0				
528.72	327	342.0					527.94	328.0	343.0				
473.54	328	341.0	678	1012	1348	1673	472.76	329.1	342.1	680.2	1015.3	1352.3	1678.3
473.54	328	341.0	675	1011	1344		472.76	329.1	342.1	677.2	1014.3	1348.3	
466.50	333	347.0	682	1016	1349		465.72	334.1	348.2	684.2	1019.3	1353.4	
466.50	333	346.0	683	1015	1347		465.72	334.1	347.2	685.3	1018.3	1351.4	
mean	329.7	342.9	679.7	1014.4	1346.0	1673.5		330.5	343.8	681.6	1017.5	1350.2	1678.9
stdev	2.6	2.5	3.2	2.6	2.5	0.7		2.6	2.6	3.2	2.6	2.5	0.8

Table 4.9. Summary of numerous theorectical determinations of ω_e and D_e for the ground state of ruthenium dimer.

Authors(Ref)	Method	Ground State	ω_e (cm^{-1})	D_e(e
Cotton and Shim6	SCF/CI	$^7\Delta_u$	116	0.6
Das, Balasubramanian7	MCSCF(CASSCF)	$^7\Delta_u$	273	2.0
Chen,Krasowski,Fitzgerald8	Gaussian, density funct	-	335	-
Goursot,Pedocchi,Coq9	Gaussian, density funct	$^7\Delta_u$	380	-
Harada, Dexpert10	Gaussian, density funct	heptet	274	2.5
"	Effective core potentials	heptet	203	1.1
Miedma and Gingerich5	Heat of Vaporization	-	-	3.3
This work			347.1	2.0

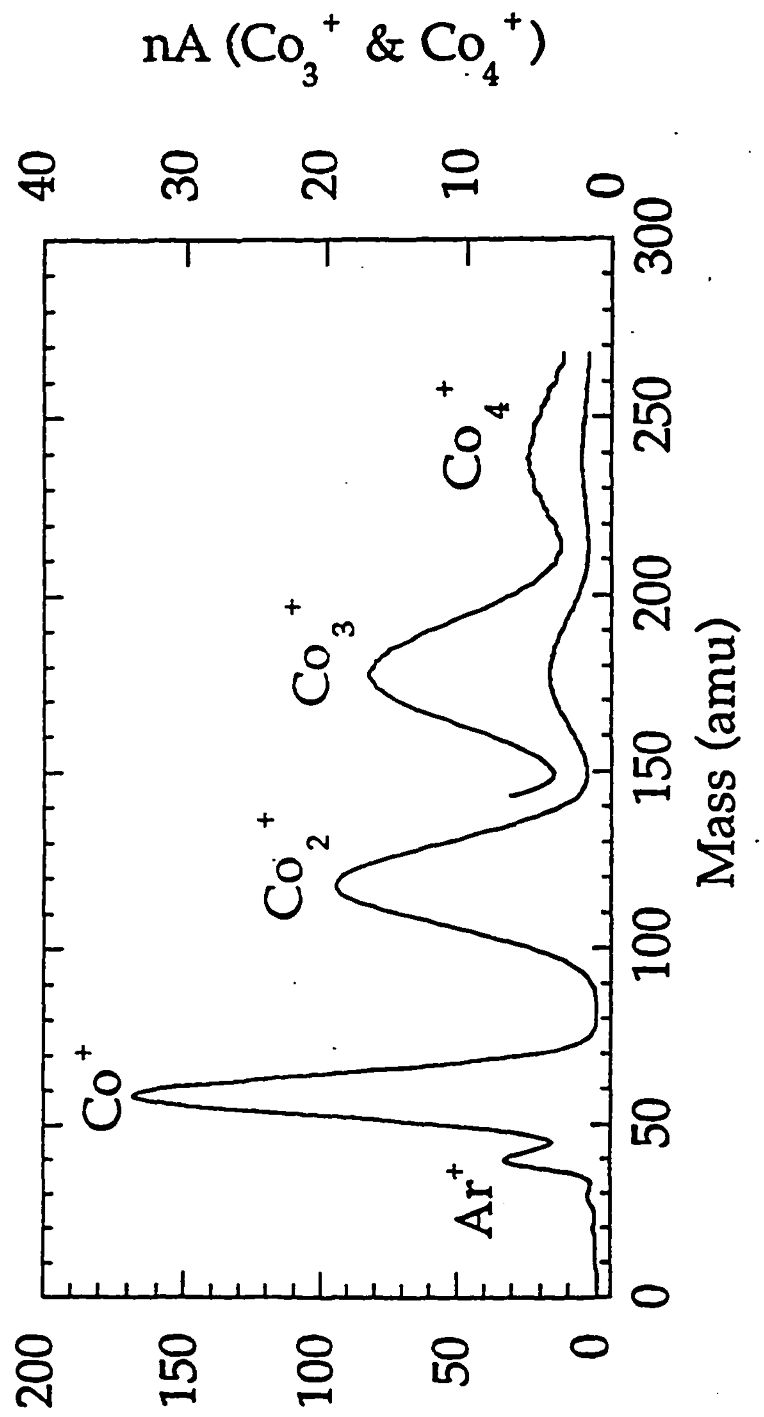

Figure 4.1. Mass Scan of sputtered Cobalt metal clusters.

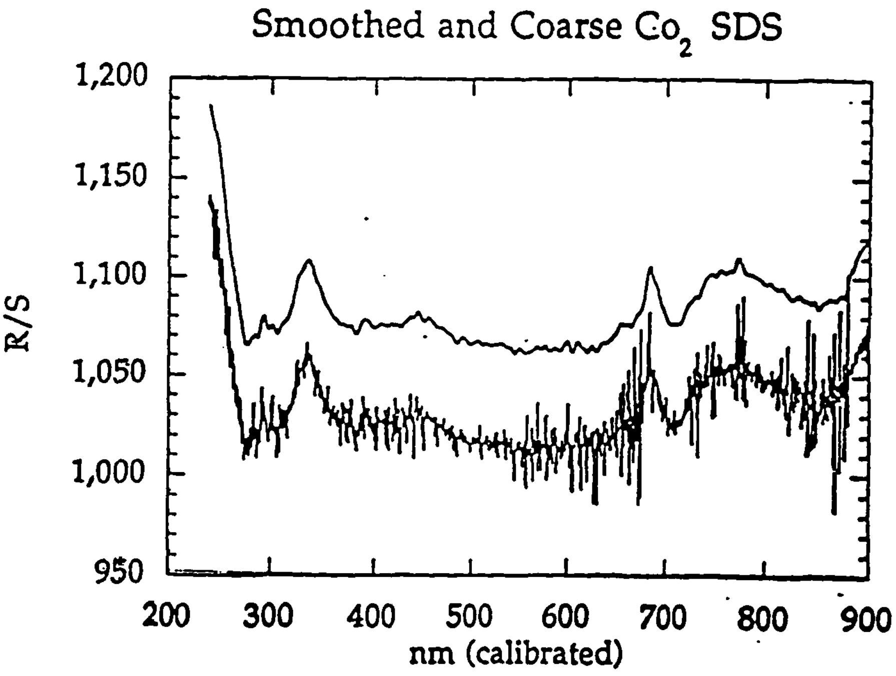

Figure 4.2. Absorption "SDS" spectra of Co_2 in Argon matrix at 14 K.

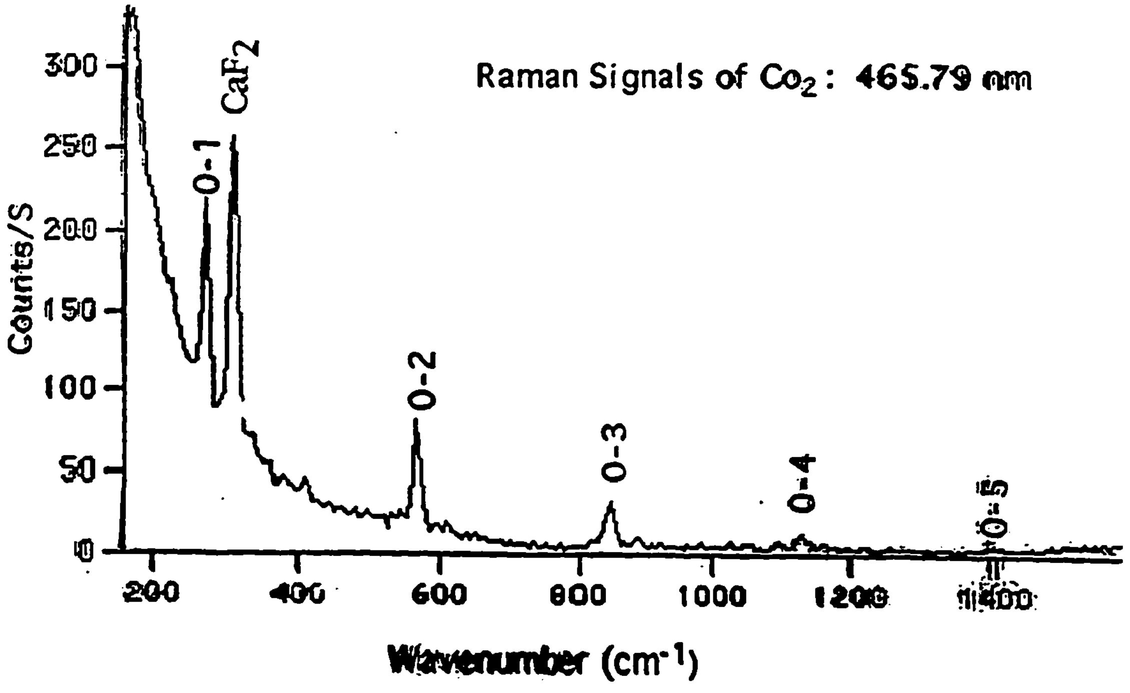

Figure 4.3. Raman spectra of mass-selected Co_2 in Argon matrix at 14 K.

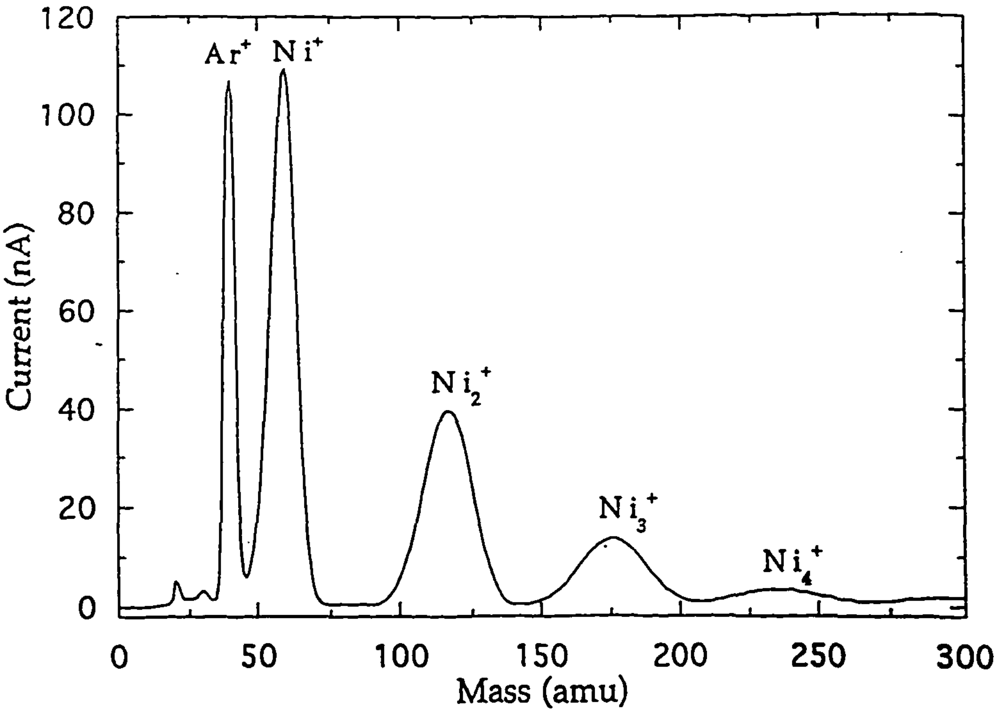

Figure 4.4. Mass Scan of sputtered Nickel metal clusters.

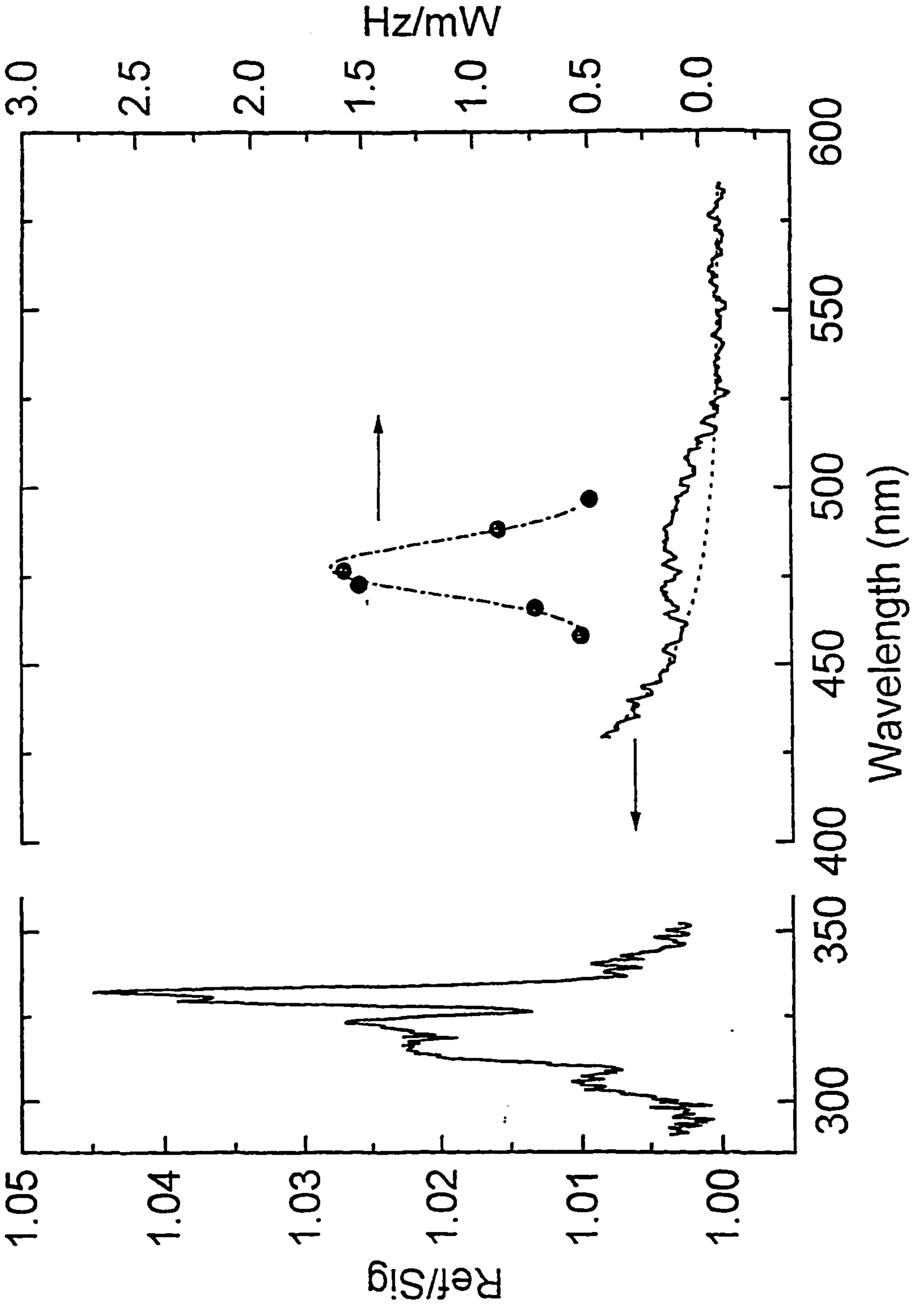

Figure 4.5. Absorption "SDS" spectra of Ni_2 in Argon matrix at 14 K.

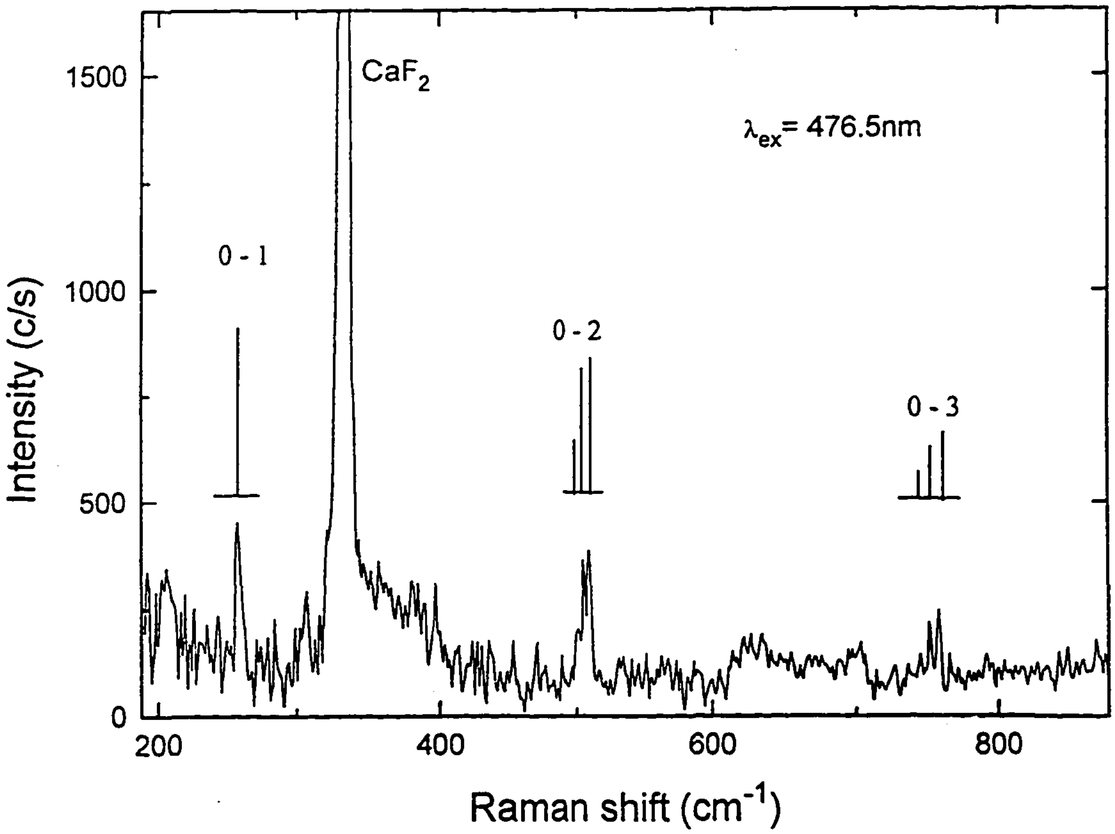

Figure 4.6. Isotopically resolved resonance Raman spectra of Ni_2 in an Argon matrix at 14 K.

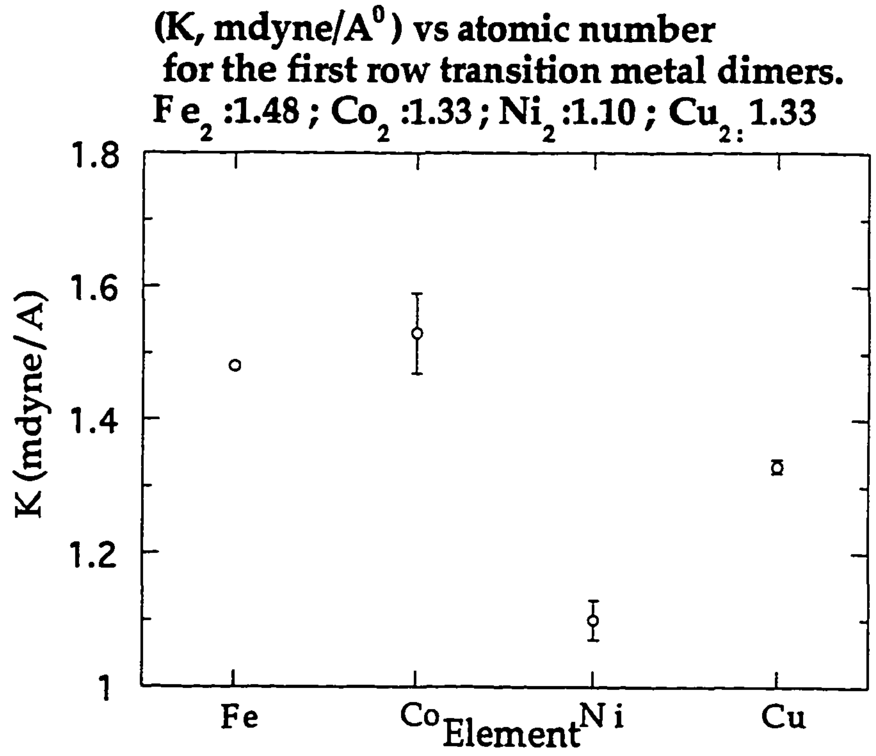

Figure 4.7. Experimental Stretching force Constants for Dimers of Fe, Co, Ni and Cu. Force Constants are in mdyne/A at 14 K.

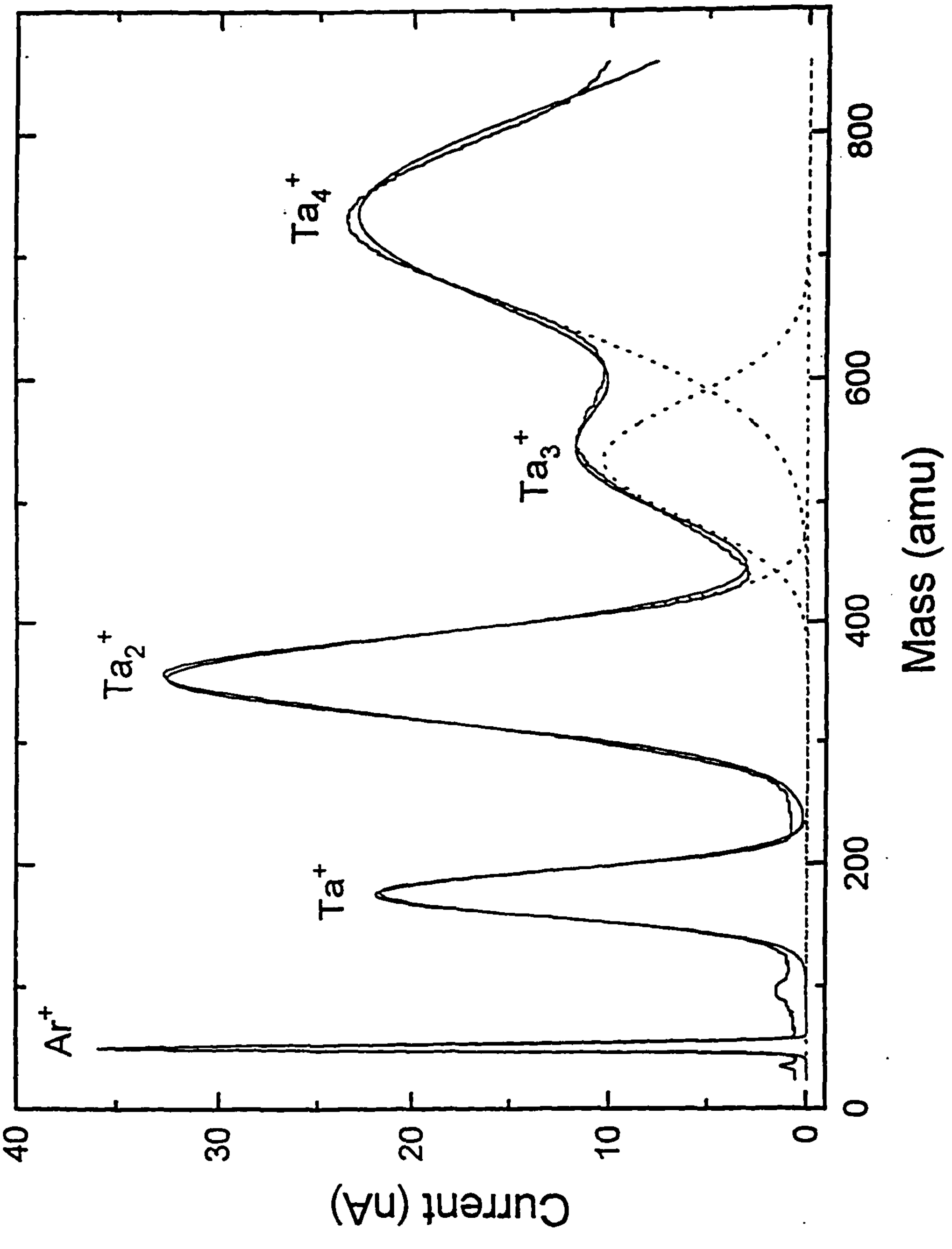

Figure 4.8. Mass Scan of Ta sputtered clusters.

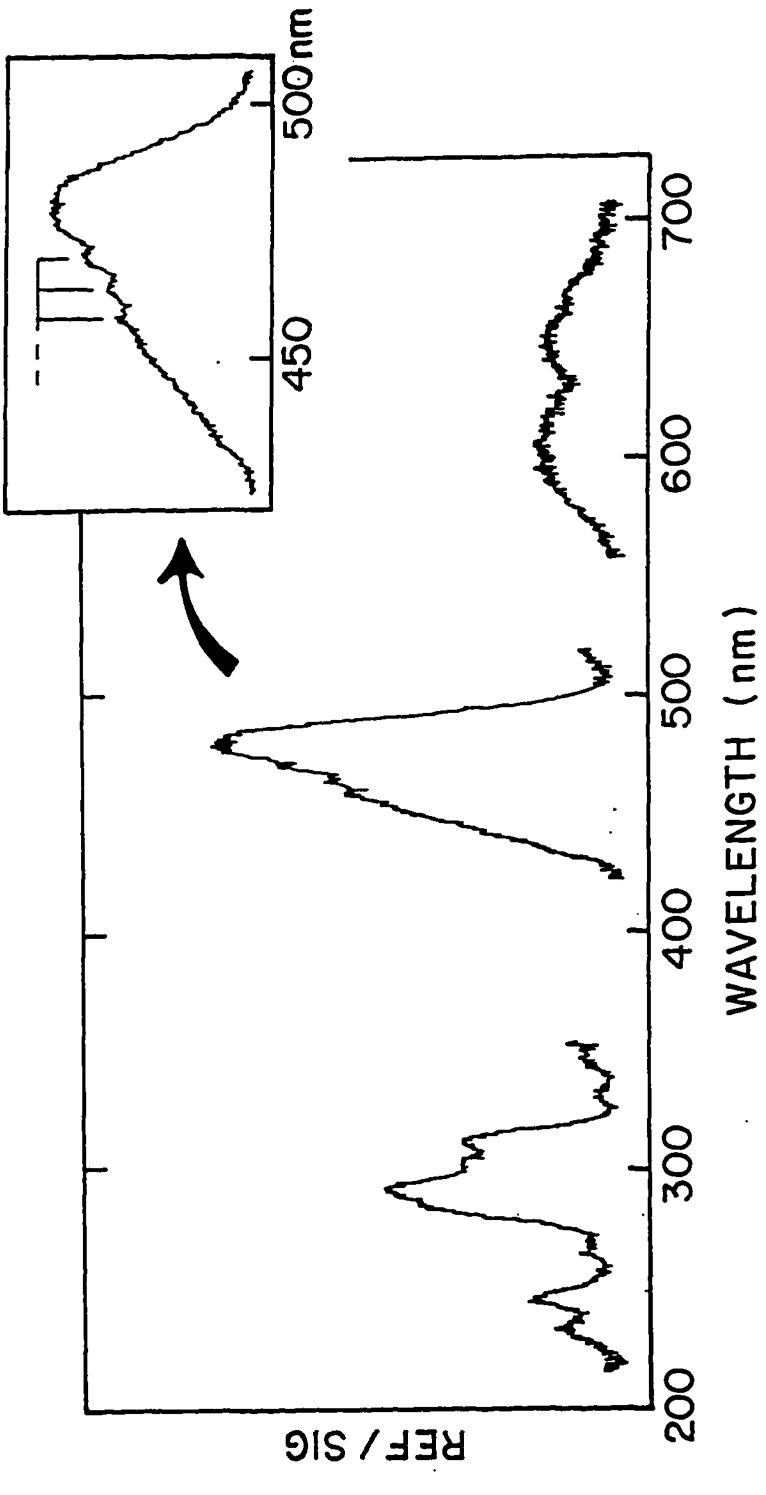

Figure 4.9. Absorption (SDS) spectra of mass-selected Ta_2 in Agron matrix at 14 K.

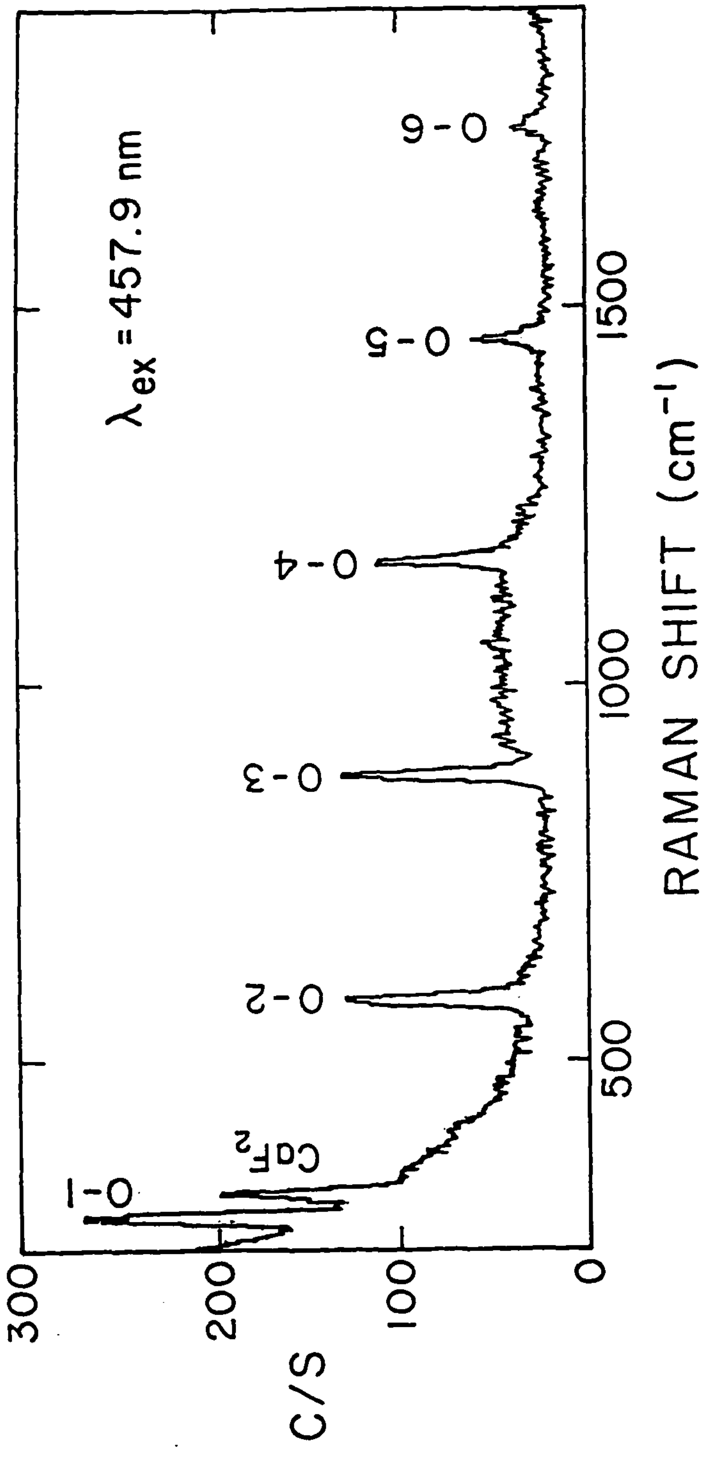

Figure 4.10. Raman spectra of mass-selected Ta_2 in Argon matrix at 14 K taken with the Spex double-mate and PMT.

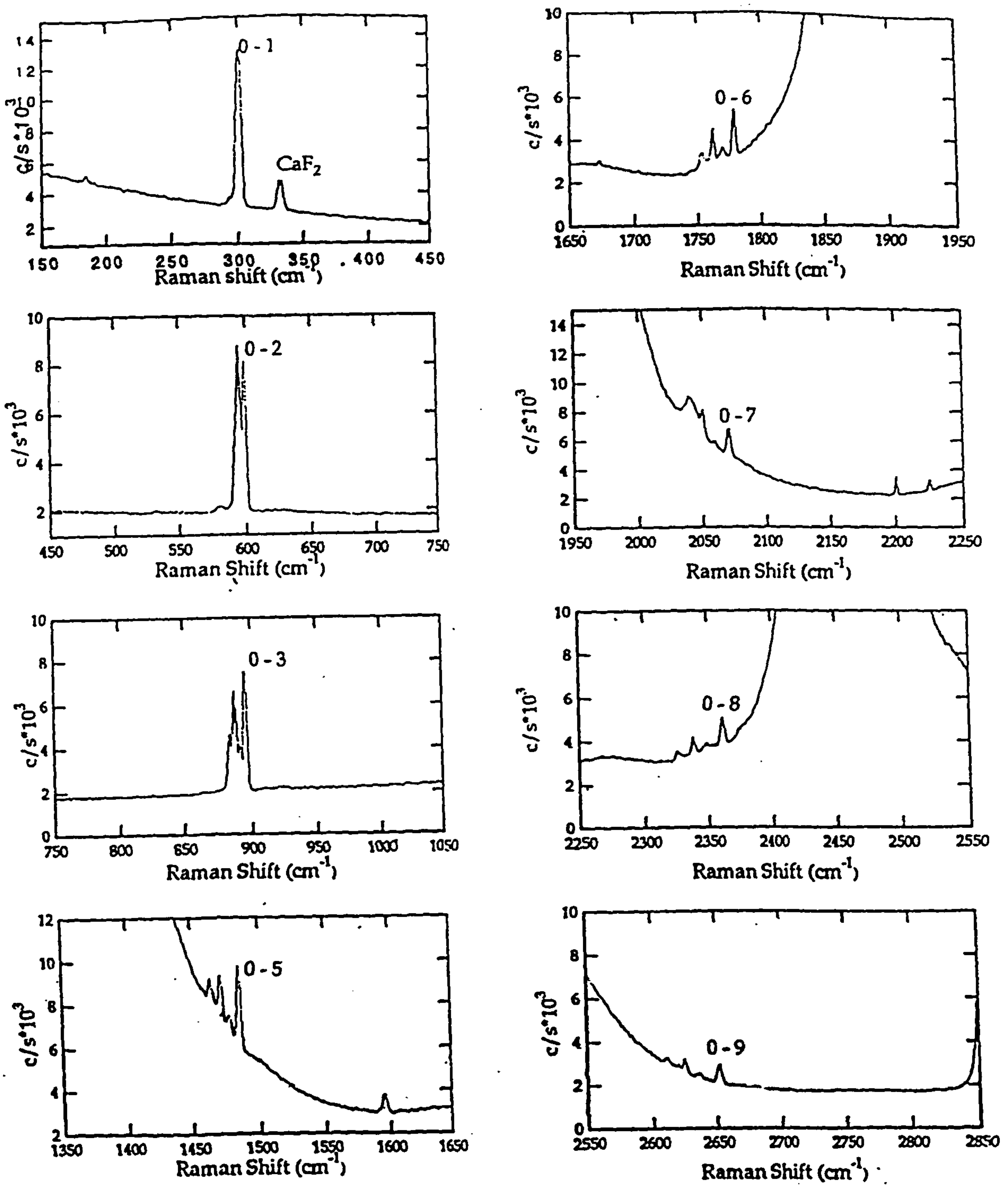

Figure 4.11. Raman spectra of mass-selected Ta_2 in Argon matirx at 14 K taken with the Spex "Spectrum-One" CCD Triple-mate system.

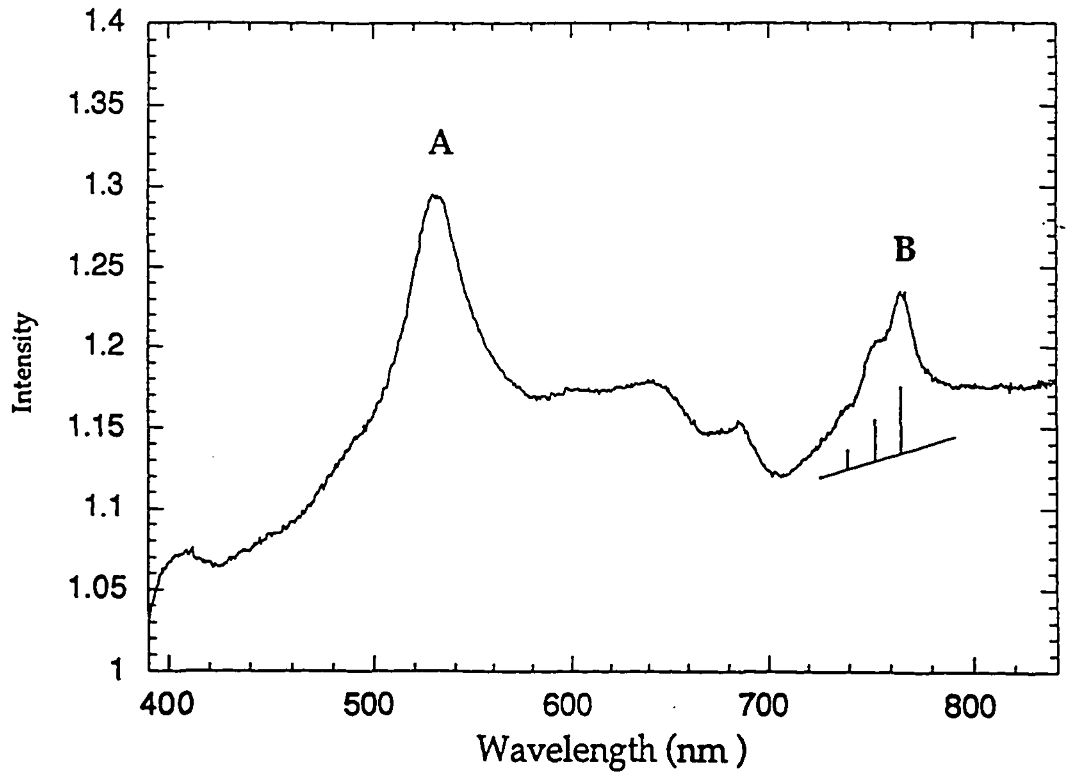

Figure 4.12. Absorption (SDS) spectra of mass-selected Ta_4 in Agron matrix at 14 K.

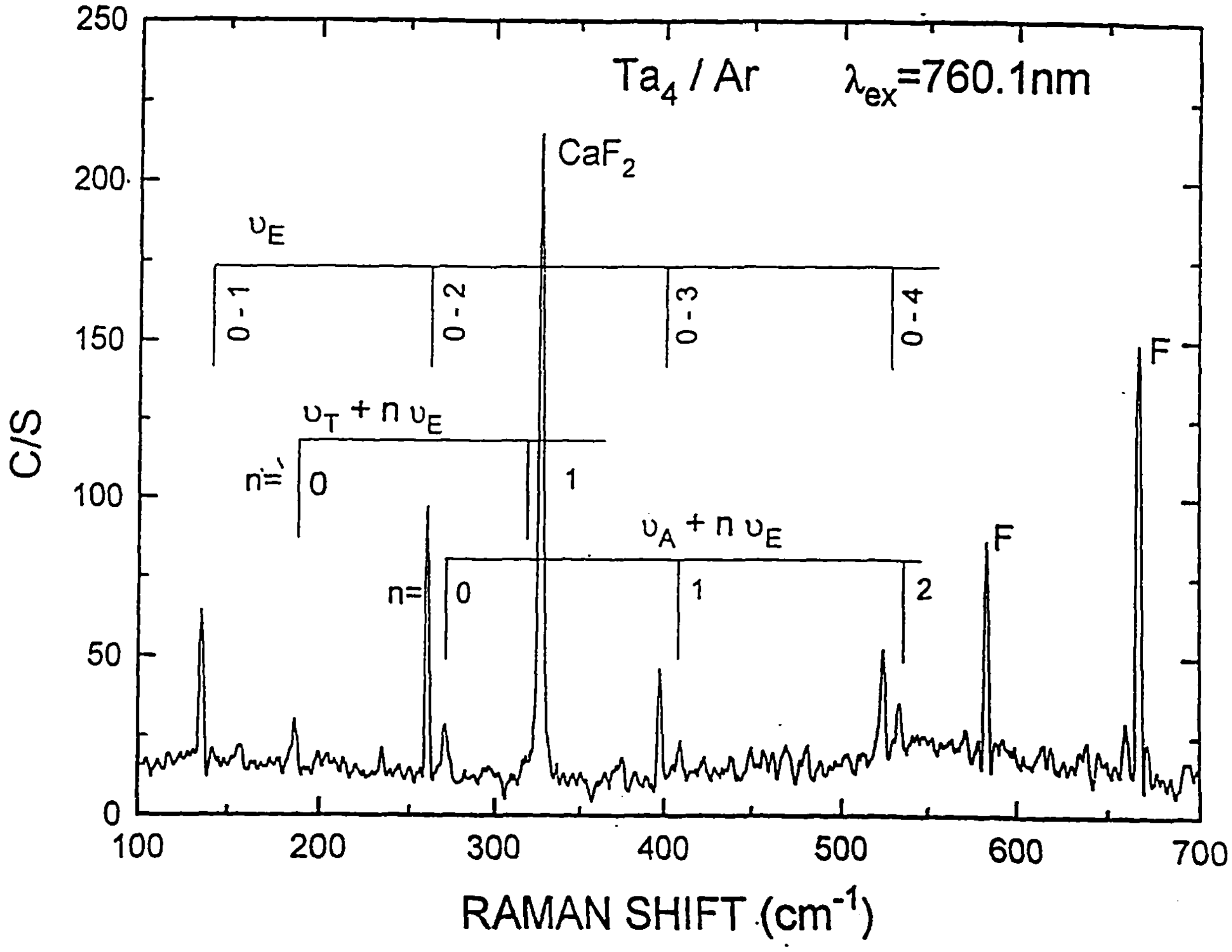

Figure 4.13. Raman spectra of mass-selected Ta_4 in Argon matirx at 14 K taken with the Spex "Spectrum- One" CCD Triple-mate system.

Herzberg (Vol. II, Infrared and Raman Spectra, p. 92)

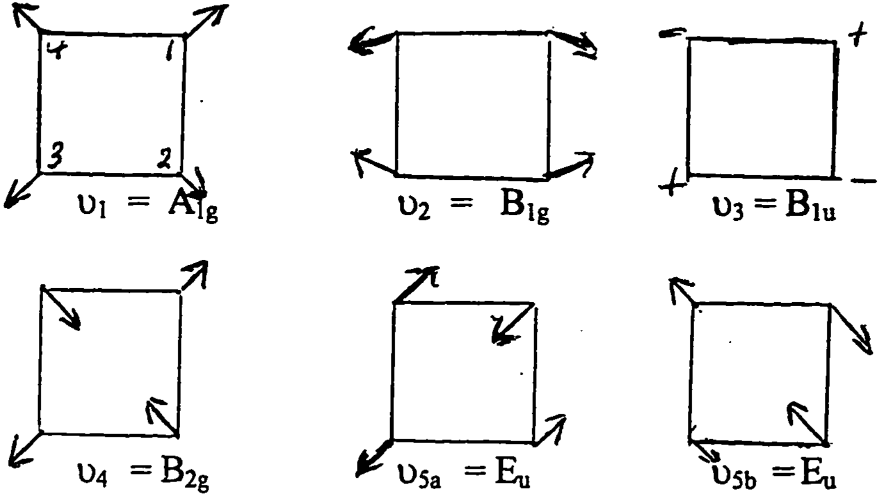

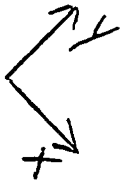

Raman Active (Normal modes): A_{1g}, B_{1g}, B_{2g}

$$Q_{Ag} = 1/2(Y_1 + X_2 - Y_3 - X_4)$$

$$Q_{B1g} = 1/2(X_1 + Y_2 - X_3 - Y_4)$$

$$Q_{B1u} = 1/2(-Z_1 + Z_2 - Z_3 + Z_4)$$

$$Q_{B2g} = 1/2(Y_1 - X_2 - Y_3 + X_4)$$

$$Q_{Eu} = 1/2\,(X_1 - X_2 + X_3 - X_4)$$

Figure 4.14. Raman Active Modes for a Square planar molecule.

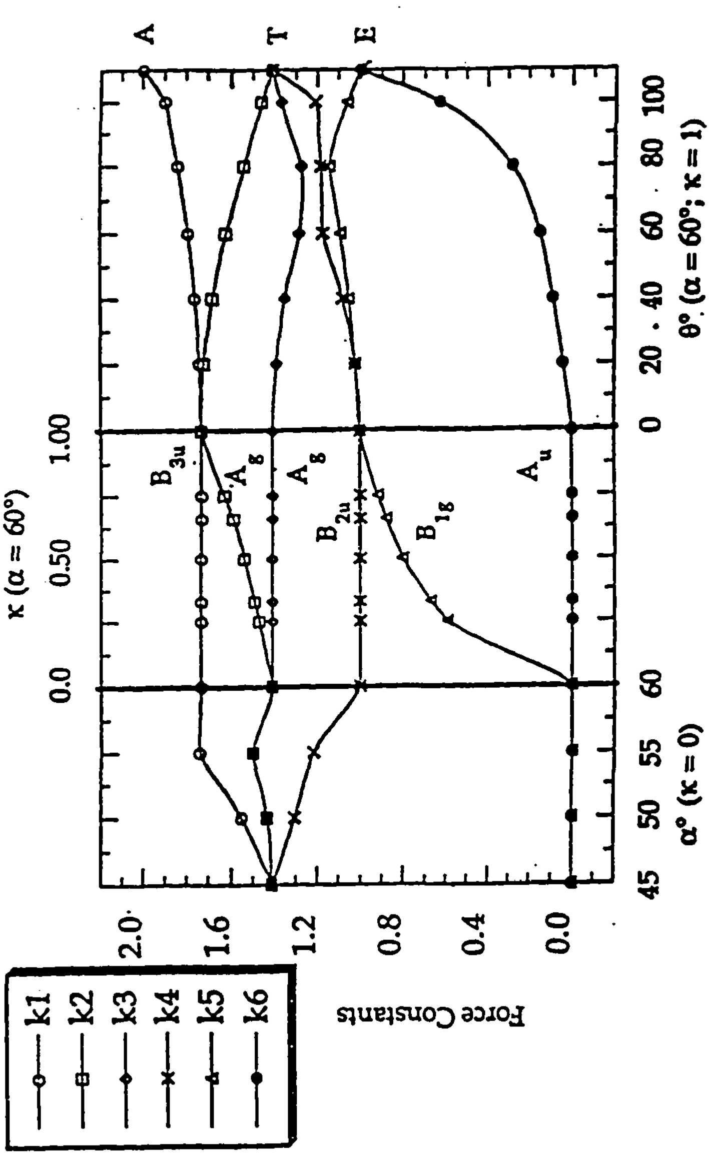

Figure 4.15. Variation of electronic symmetry with Romboidal angle to Tetrahedral structure.

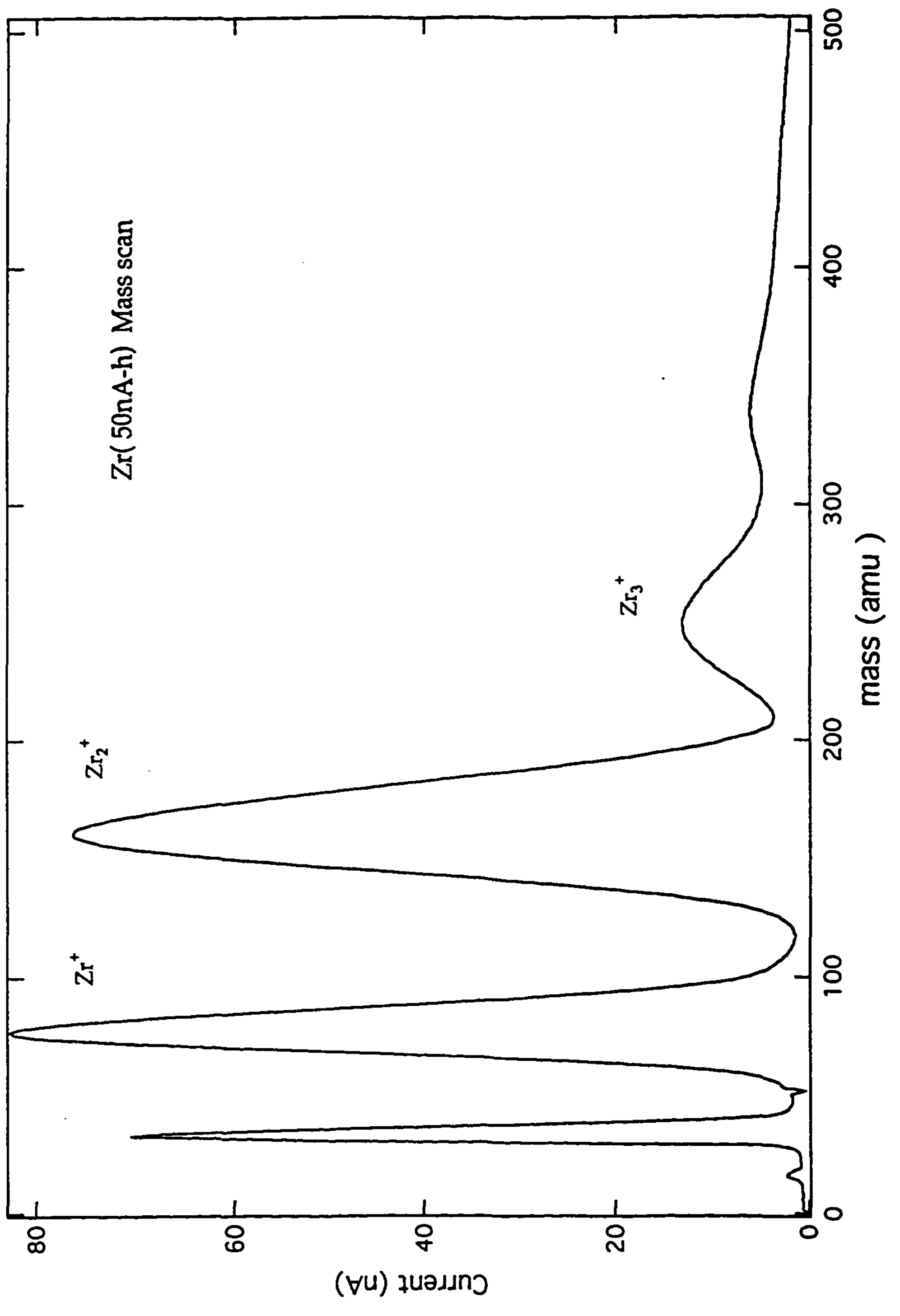

Figure 4.16. Mass Scan of sputtered Zr clusters from sputtering target, measured in situ by recording the current on the Faraday plate as a function of the magnetic field on the Wien filter.

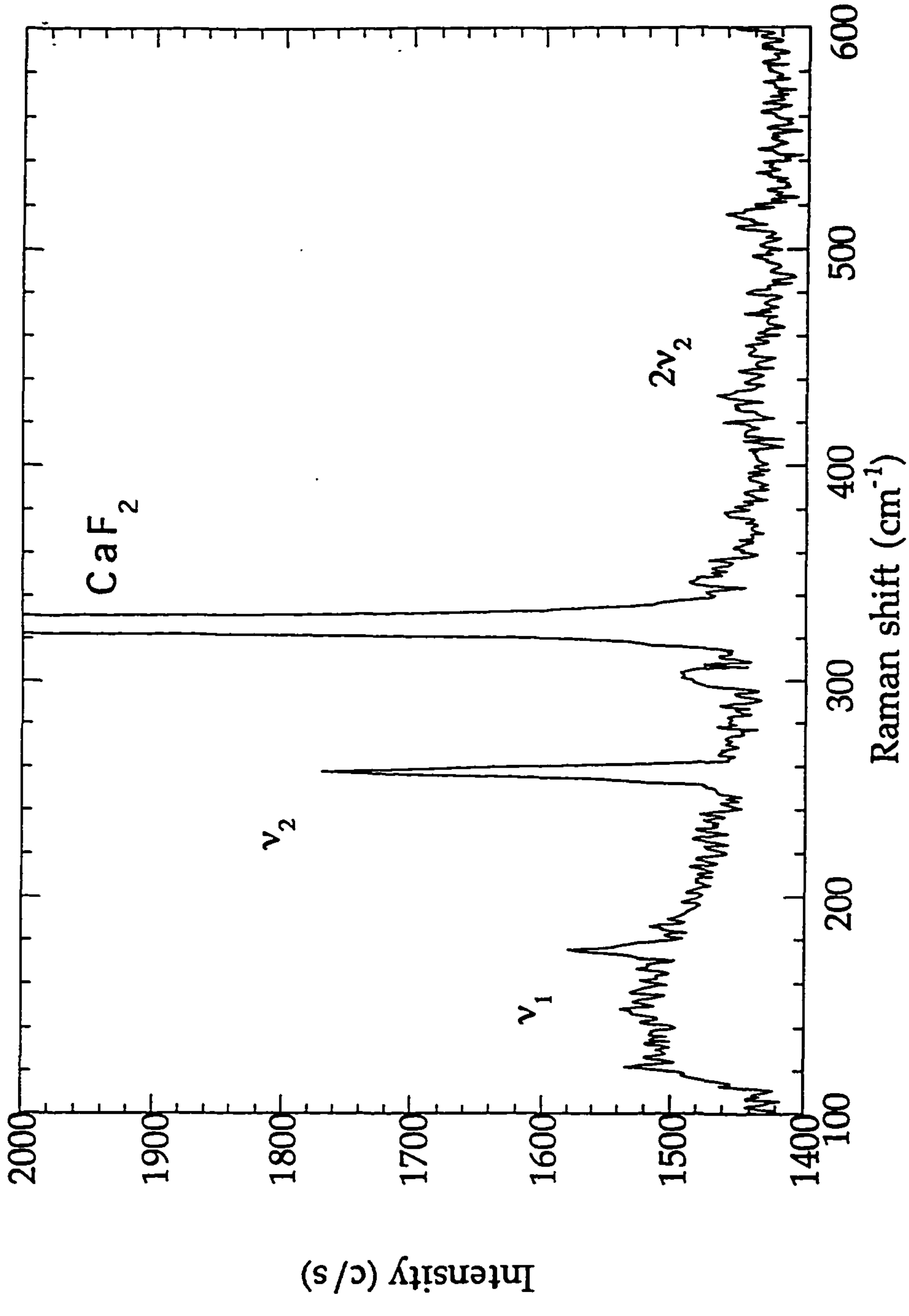

Figure 4.17. Resonance Raman spectrum of Zr_3 at 14K in the Argon matrix. In additon to the line at 330cm^{-1} due to the CaF_2 substrate, three spectral lines are observed.

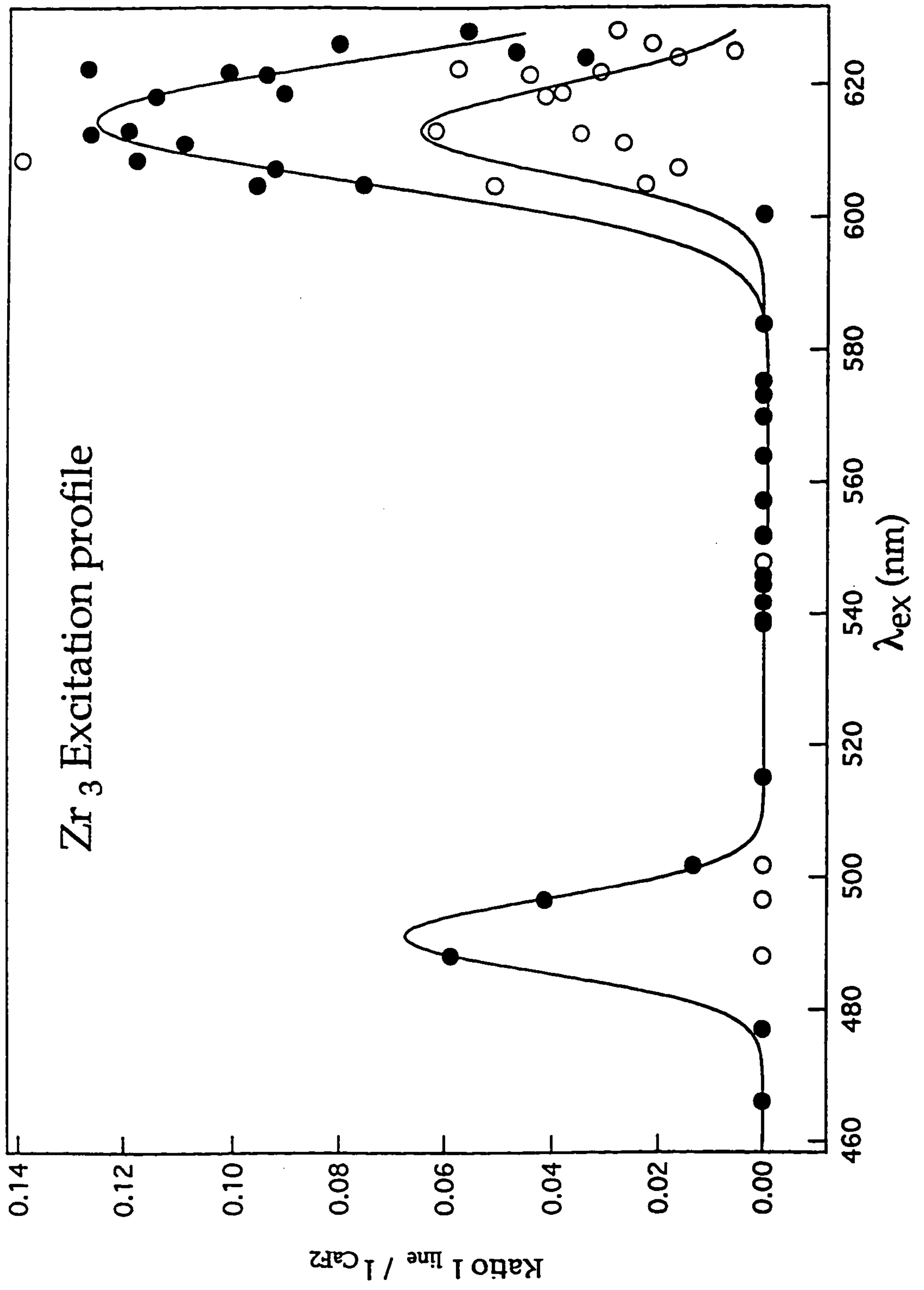

Figure 4.18. Raman excitation profiles for the υ_1 (a_1') (filled circles) and the $\upsilon_2(e')$ (open circles) lines of Zr_3.

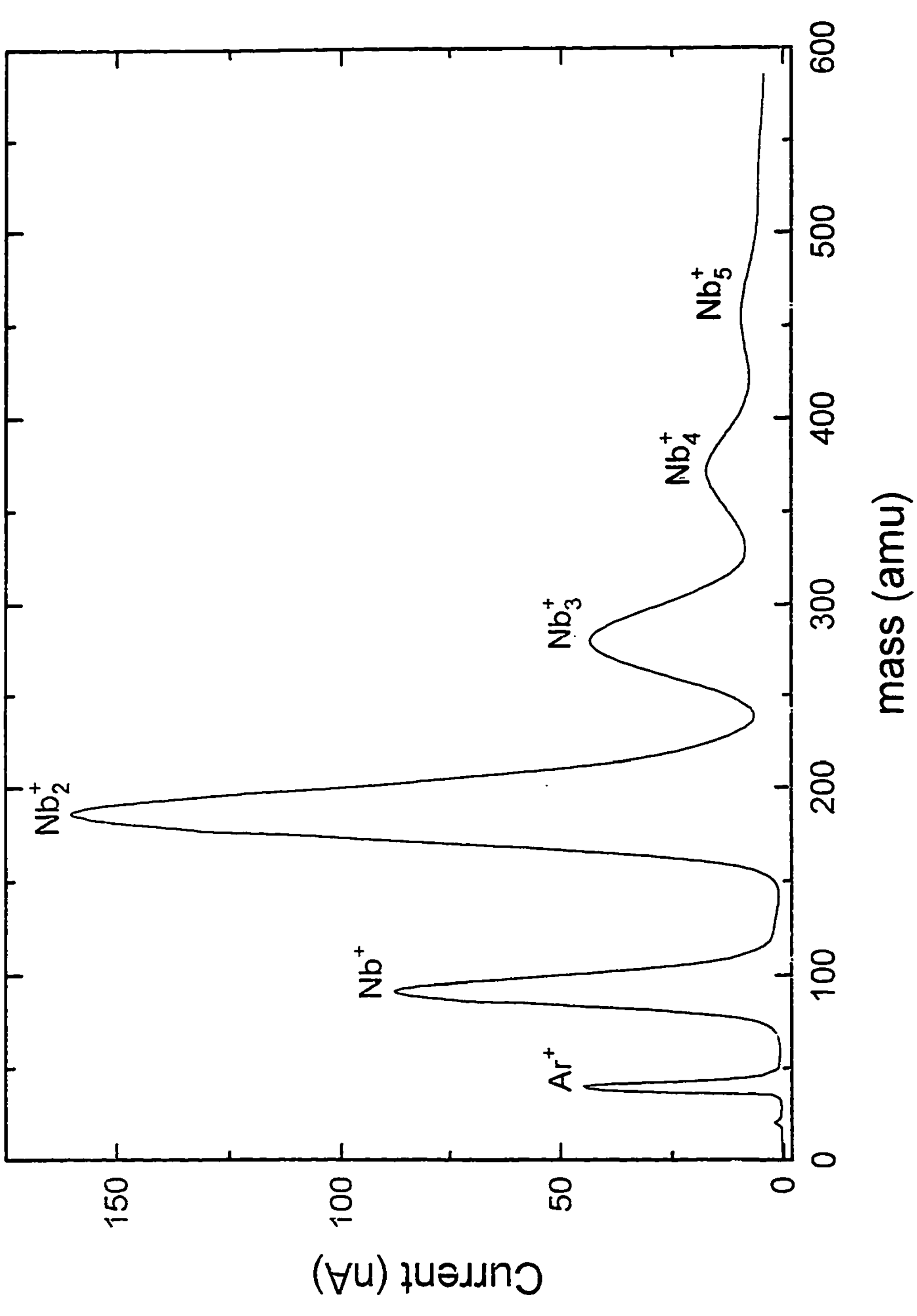

Figure 4.19. Mass Scan of sputtered Niobium metal clusters.

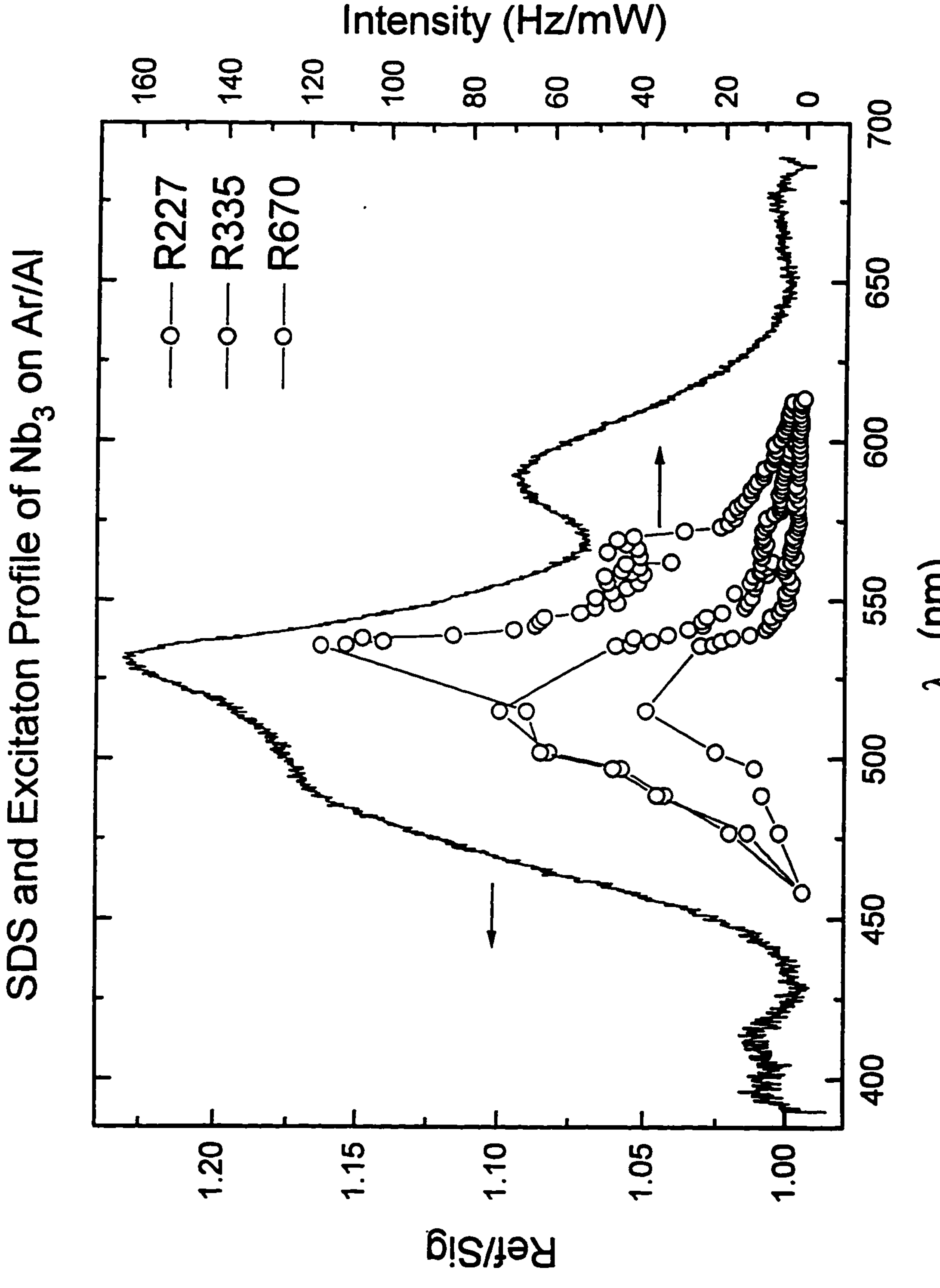

Figure 4.20. Absorption "SDS" spectra(left hand scale) of Nb_3 in Argon matrix at 14 K. Superimposed are excitation profiles for two fundamentals and one overtone (rigth hand scale) for triatomic niobium is solid Ar.

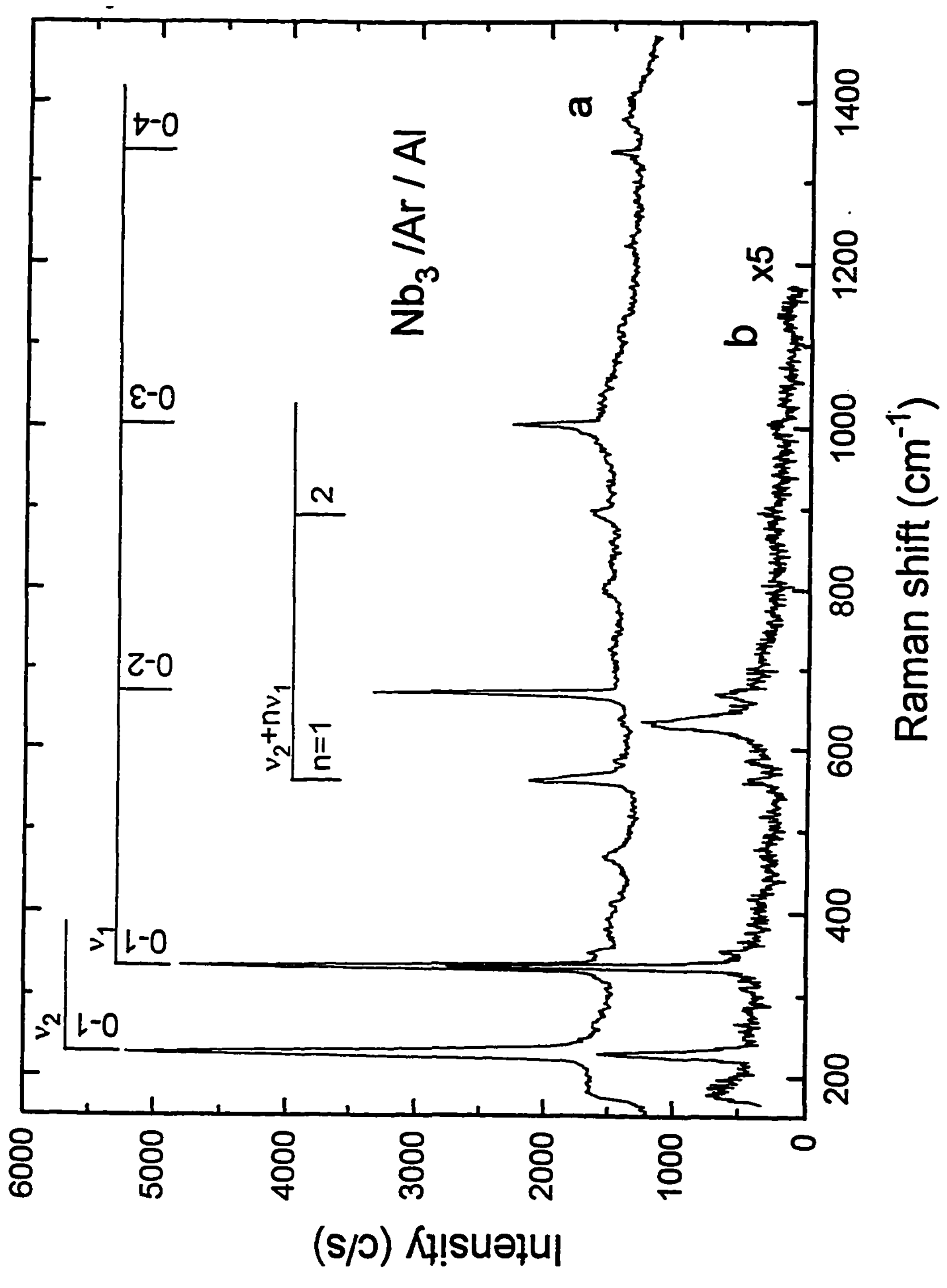

Figure 4.21. The resonance Raman spectra of Nb_3 in Ar matrix excited with (a) 514.5 nm; and 588.8 nm radiation. The intensity in the latter was multiplied by a factor of five as compared to the former.

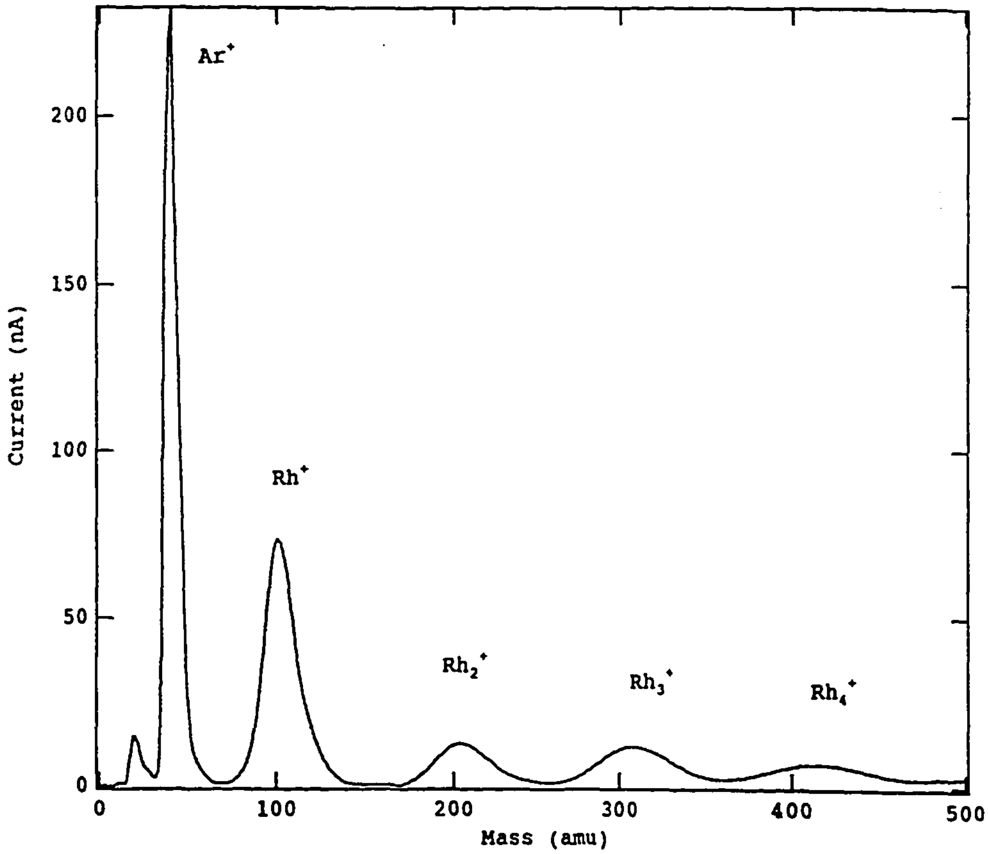

Figure 4.22. Mass Scan of sputtered Rhodium metal clusters.

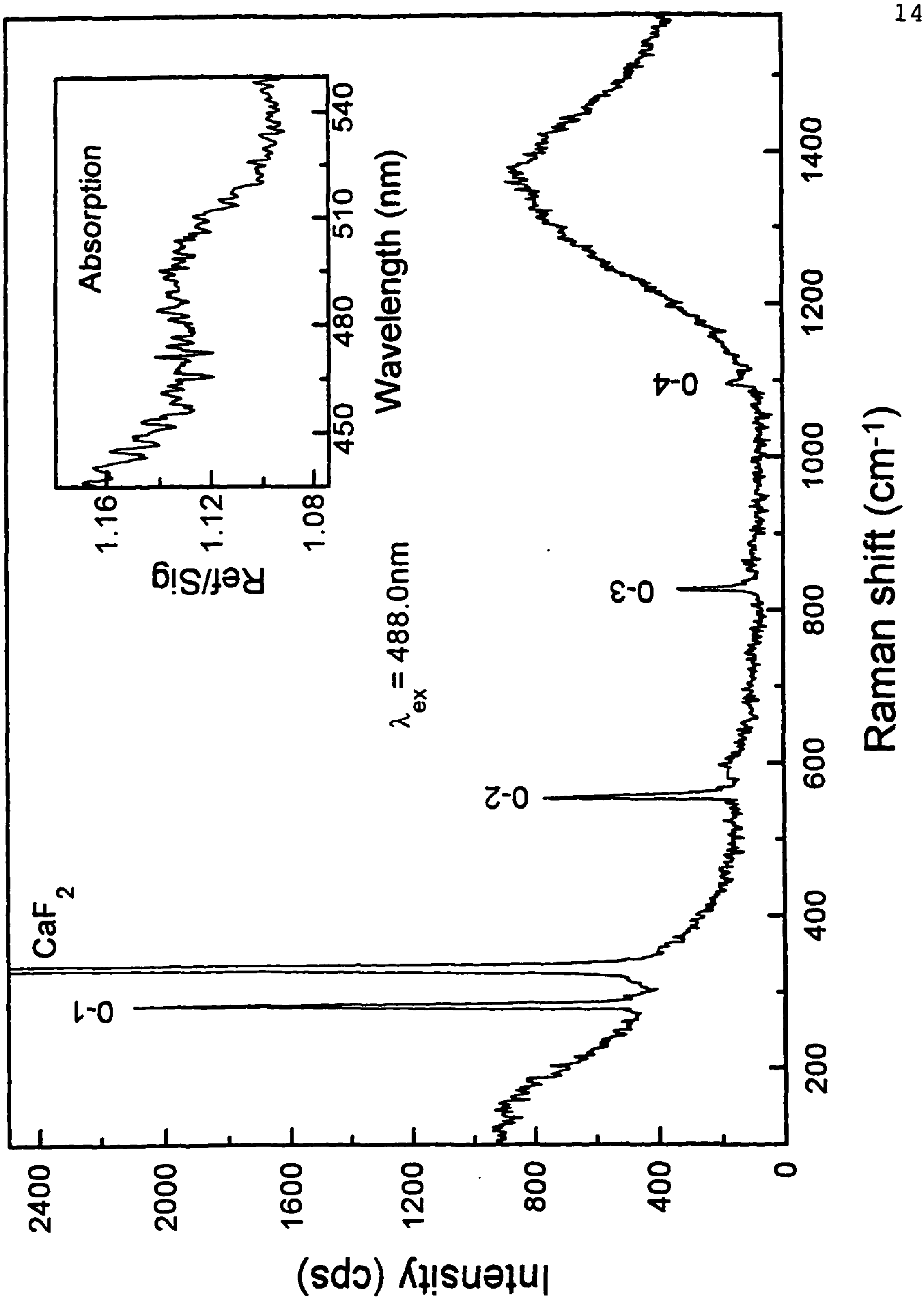

Figure 4.23. Resonance Raman and (insert) absorption (scattering depletion spectra for Rh_2 in an argon matrix.

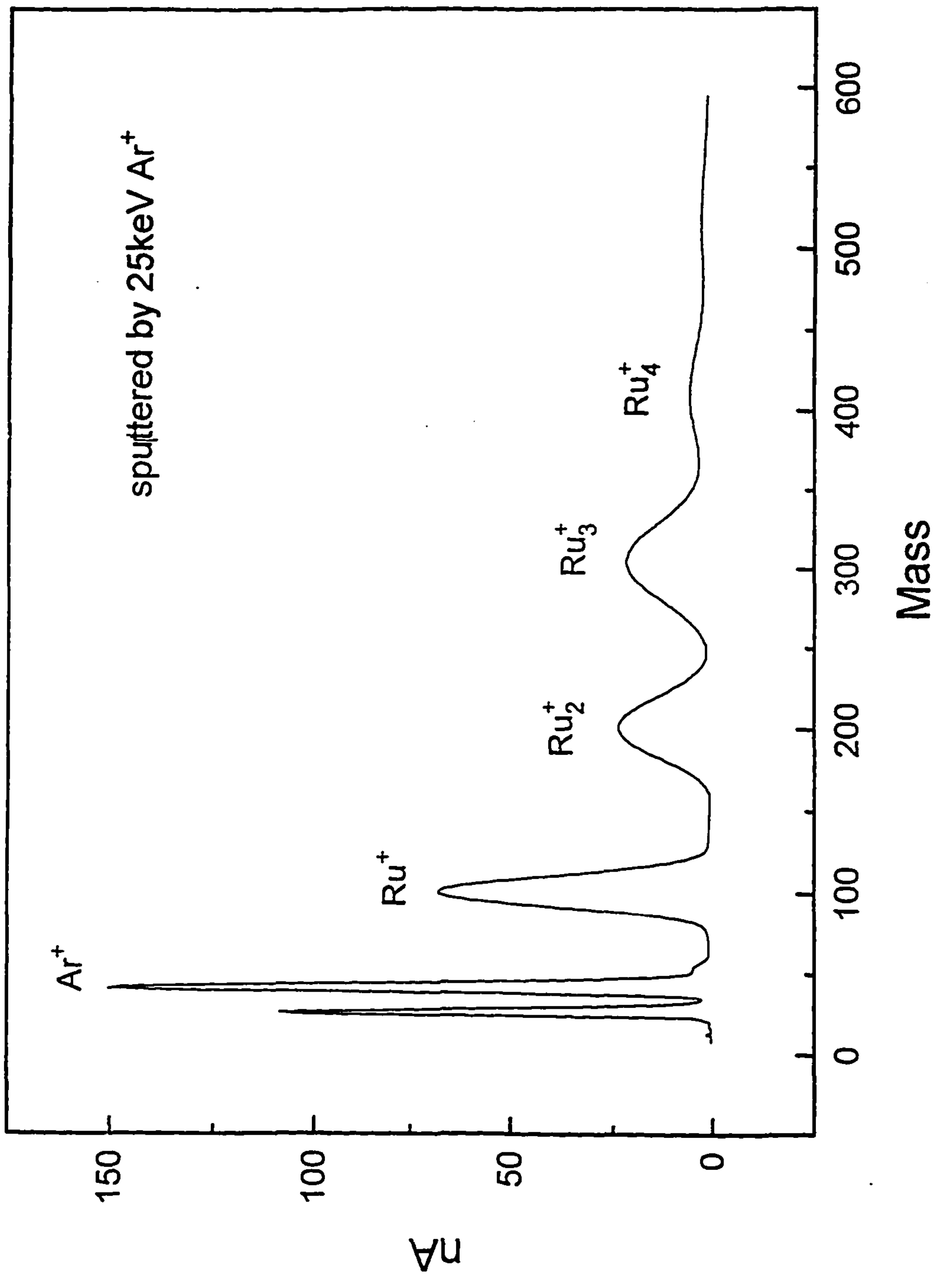

Figure 4.24. Mass Scan of sputtered Ruthenium metal clusters.

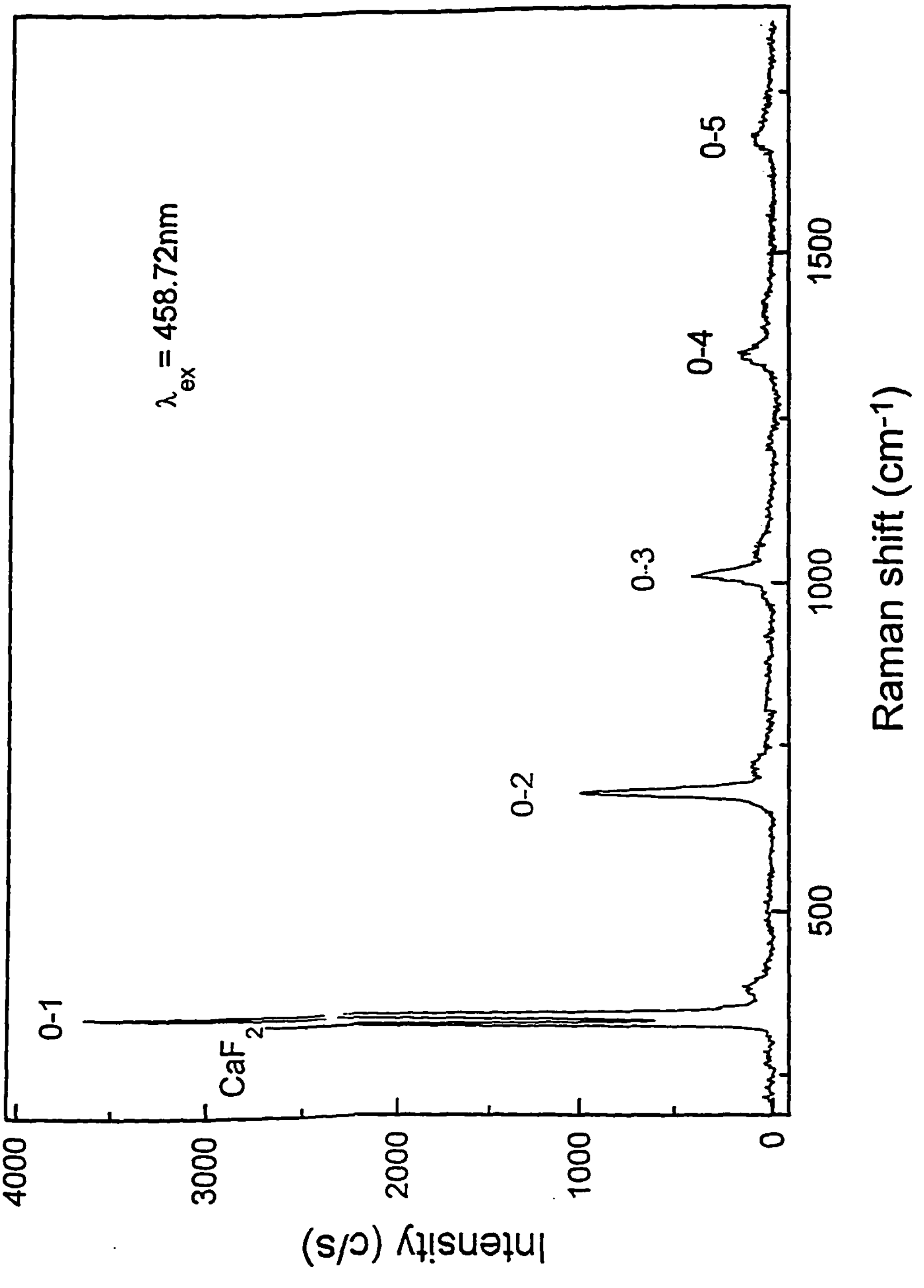

Figure 4.25. Resonance Raman Spectra of Ru$_2$ in Ar matrix with 458.7 nm radiation.

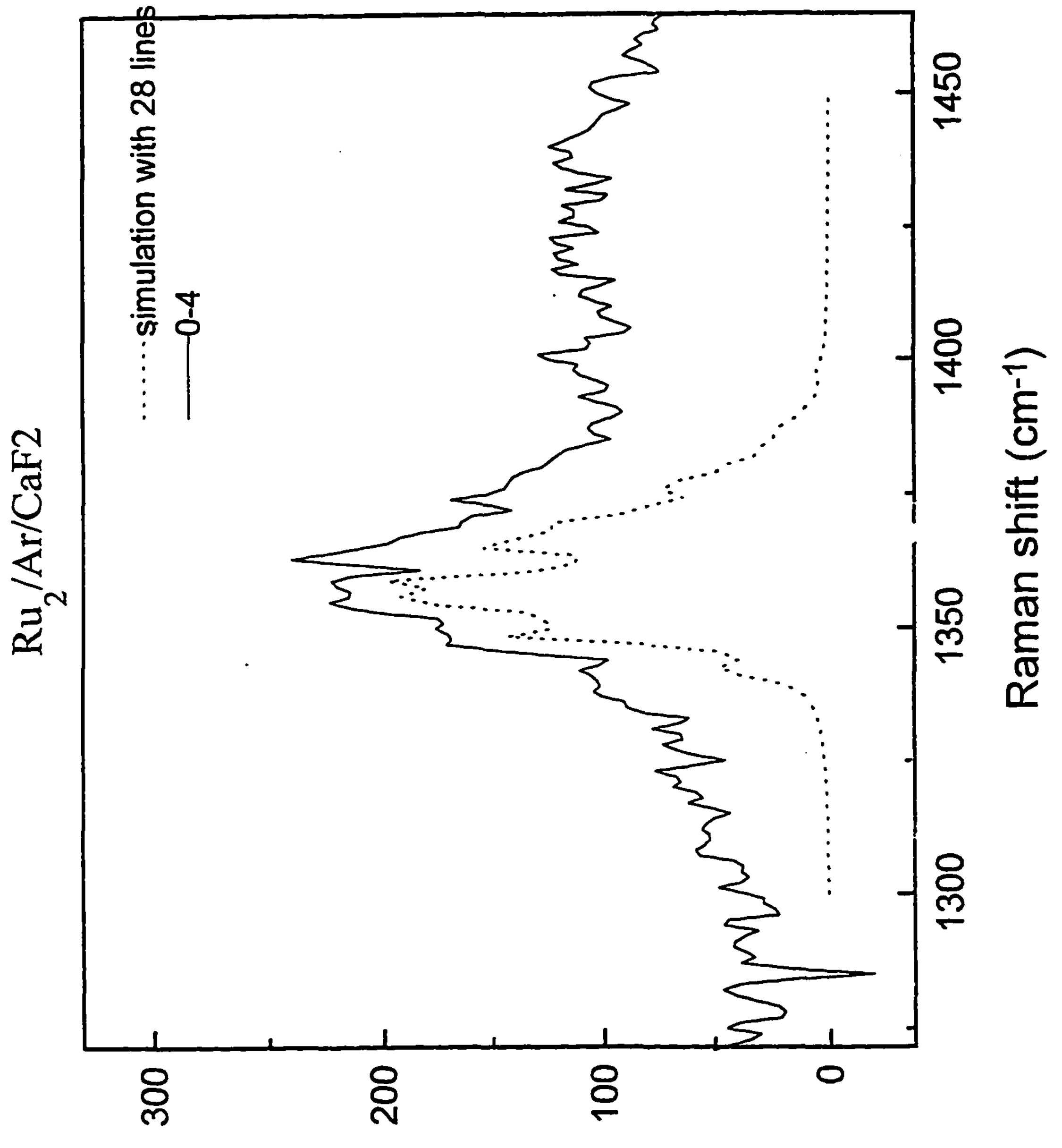

Figure 4.26. Simulated effect of twenty eight isotopes of Ru_2 on the shape of the 0-4 overtone, and comparison with the experimentally observed line.

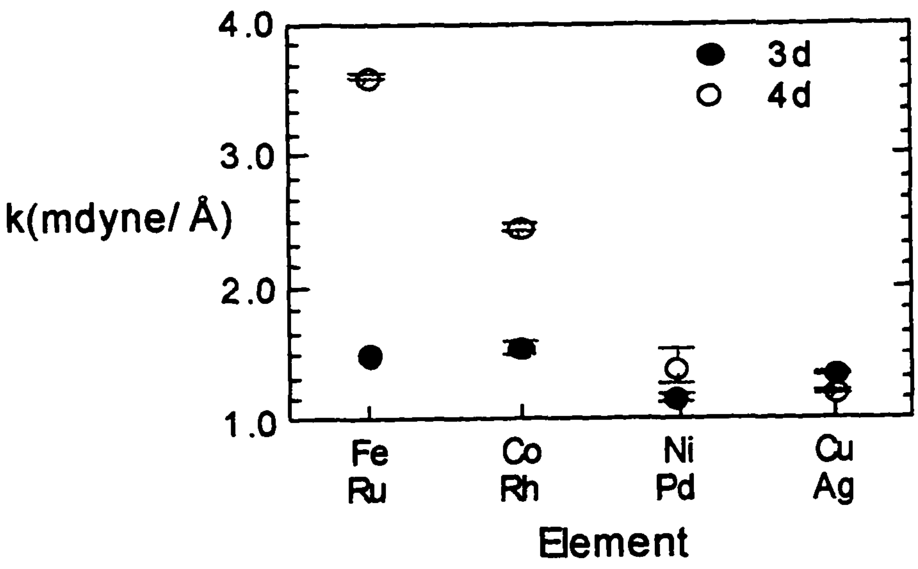

Figure 4.27. Experimental Stretching force Constants for Dimers of Pd, Rh, Ru and Ag. Force Constants are in mdyne/A at 14 K.

REFERENCES

1. Jian-Guo Dong, Zhendong Hu, Robert Craig, J. R. Lombardi, and D. M. Lindsay, *Raman Spectroscopy of Mass-selected Cobalt Dimer in Argon Matrices,* J. Chem. Phys. **101** (11), 1 December 1994.

2. Zhendong Hu, Jian-Guo Dong, John R. Lombardi, and D. M. Lindsay, *Absorption, fluorescence, and Raman spectra of Mass-selected Rhenium Dimers in Argon Matrices,* J. Chem. Phys. **101** (1), 1 July 1994.

3. Huaming Wang, Robert Craig, Hanae Haouari, Jian-Guo Dong, Zhendong Hu, Alberto Vivoni, John R. Lombardi, and Derek M. Lindsay, *Absorption and Raman Spectroscopy of Mass-selected Tantalum tetramers in Argon Matrices,* J. Chem. Phys., Vol. **104**, No. 10, 8 March 1996

4. C.V. Venkateswaran, Proc. Ind. Acad. Sci. **2A**, 260 (1935).

5. *Fifth International Meeting on Small Particles and Metal Clusters,* Konstanz, Germany, 1990. Zeits. Phys. **D19**, (1991); *Sixth International Meeting on Small Particles and Metal clusters, Chicago, Illinois,* 1992. Zeits. Phys. **D26**, (1993).

6. *International Symposium on the Physics and Chemistry of Small Clusters*, NATO Advanced Workshop, Richmond, Virginia (1991). See: *Physics and Chemistry of Finite Systems: From Clusters to Crystals*, edited by P. Jena and S. N. Knanna and B. K.Rao (Kluwer, Dordrecht, 1992).

7. *Symposium on Clusters and Cluster Assembled Materials*, Materials Research Society Meeting, Boston (1990). See: MRS Symposium Series 206, (1991).

8. *First International Conference on Nuclear and Atomic Clusters*, Turku, Finland (1991); *Second International Conference on Nuclear and Atomic Clusters*, Santorini, Greece (1993).

9. *Transition Metal Molecules*, W. Weltner and R. J. Van Zee, Ann. Rev. Phys. Chem. **35**, 291 (1984).

10. *Clusters of Transition-metal Atoms*, M.D. Morse, Chem. Rev **86**, 1049 (1986).

11. *Metal Clusters*, edited by M. Moskovits (Wiley, New York 1986).

12. *Spectroscopy and Dynamics*, edited by M. A. Cuncan, *Advances in Metal and Semiconductor Clusters* (JAI press,

Greenwich CT, 1992).

14. For example: T.H. Maugh, Science **219**, 474, 944, 1413 (1983).

15. A. L. Robinson, Science **185**, 772 (1974); 194, 1150 (1976).

16. J. H. Sinfelt, Science **195**, 641 (1977): Acc. Chem. Res. 10, 15 (1977).

17. J. Haggin, Chem. & Eng. News, pg. 32, Jan. 18 (1993).

18. J. F. Hamilton and P. C. Logel, J. Catal. 29, 253 (1973); Photo. Sci. Eng. **18**, 507 (1974); J.F. Hamilton, J. de Phys. **C2**, 181, (1977).

19. C. Wang, S. Pollack, D. Cameron and M.M. Kappes, J. Chem. Phys. **93**, 3787 (1990).

20. See, for example: W. Harbich, S. Fedrigo, F. Meyer, D.M. Lindsay, J. Ligieres, J. C. Rivoal and D. Kreisle, J. Chem. Phys. **93**, 8535 (1990).

21. E.C. Honea, A. Ogura, C.A. Murray, k. Raghavachari, W.O. Sprenger, M.F. Jarrold and W.L. Brown, Nature 366, 42 (1993).

22. Zhendong Hu, Bo Shen, Qinwei Zhou, S. Deosaran, J. R. Lombardi, D. M. Lindsay and W. Harbich, J. Chem. Phys. **95**, 2206 (1991).

23. Zhendong Hu, Bo Shen, Qinwei Zhou, S. Deosaran, J.R. Lombardi, D. M. Lindsay, Proc. SPIE **1599**, 65 (1992).

24. M. Morse, Chem. Rev. **86**, 1049 (1986).

25. Zhengdong Hu, Bo Shen, Qinwei Zhou, S. Deosaran, J. R. Lombardi, D. M. Lindsay and W. Harbich, J. Chem. Phys. **95**, 2206 (1991).

REFERENCES for Cobalt dimer

26. J.Ho, M.L. Polak, K.M Ervin, and W.C. Lineberger, J. Chem. Phys. **99**, 8542 (1993).

27. J. Ho, Ph.D. thesis, University of Colorado, Boulder, 1991.

28. E.M. Spain and M.D. Morse, J. Chem. Phys. **97**, 4641 (1992).

29. D.G. Leopold and W.C. Lineberger, J. Chem. Phys. **85**, 51 (1986).

30. D.G. Leopold, J. Alomof, W.C. Lineberger, and P.R.

Taylor, J. Chem. Phys. **88**, 3780 (1988).

31. Z. Hu, B. Shen, Q. Zhou, S. Deosaran, J.R. Lombardi, D.M. Lindsay, and W. Harbich, J. Chem. Phys. **95**, 2206 (1991).

32. Z. Hu, B. Shen, S. Deosaran, J.R. Lombardi, and D.M. Lindsay,Proc. SPIE **1599**, 65 (1992).

33. W. Harbich, S. Fredrigo, F. Meyer, D.M. Lindsay, J. Lignieres, J.C. Rivoal, and D. Kreisle, J. Chem. Phys. **93**, 8535 (1990).

34. Z. Hu, B. Shen, Q. Zhou, J.R. Lombardi, and D.M. Lindsay, J. Chem. Phys. **96**, 8757 (1992).

35. Product of current and depostition time in hours; 1nA-h=$2.25x10^{13}$ particles.

36. G.A. Ozin and A. J. L. Hanlan, Inorg. Chem. **18**, 1781 (1979).

37. A.R. Gee, D.C. O'Shea, and H.Z. Cummins, Solid State Commun. **4**, 43 (1965).

38. D.P. DiLella, A Loewenschuss, and M. Moskovits (to be published). See Table I of: D.P., DiLella, W. Zlimm, R.H., Lipson, M. Moskovits, and K.V. Taylor, J. Chem. Phys. **77**,

5263 (1982).

39. G. Herzberg, Spectra of Diatomic Molecules (Van Nostrand, New York, 1950).

40. C.E. Moore, Atomic Energy Levels, Natl. Stand. Ref. Data. Ser. No. 35 (U.S. Natl. Bur. Stand. Washington, D.C. 1971).

41. I. Shim and K. A. Gingerich, J. Chem. Phys. **78**, 5693 (1983).

42. T.L. Haslett and M. Moskovits, J. Mol. spectrosc. **135**, 259 (1989).

43. E.A. Rohfing and J.J. Valentini, J. Chem. Phys. **84**, 6560 (1986).

REFERENCES For Nickel Dimer

44. Z. Hu, B. Shen, Q. Zhou, S. Deosaran, J.R. Lombardi, D.M. Lindsay and W. Harbich, J. Chem. Phys. **95**, 2206 (1991).

45. Z. Hu, B. Shen, Q. Zhou, S. Deosaran, J.R. Lombardi and D.M. Lindsay, Proc. SPIE **1599**, 65 (1992).

46. Z. Hu, Jain-Guo Dong, John R. Lombardi, and D.M Lindsay, J. Chem. Phys. **97,** 9263 (1993).

47. *Spectra of Diatomic Molecules,* G. Herzberg (Van Nostrand, New York, 1945).

48. K.P. Huber, and G. Herzberg, *Constants of Diatomic Molecules,* Van Nostrand, New York, 1979.

49. Hanae Haouari, Huaiming Wang, Robert Craig, John R. Lombardi, and D.M. Lindsay, J. Chem. Phys., **103,** 9527 (1995).

50. Huaiming Wang, Robert Craig, Hanae Haouari, Yifei Liu, John R. Lombardi, and D.M. Lindsay, J. Chem. Phys., **105,** 5355 (1996).

51. Z. Hu, J.G. Dong, J.R. Lombardi and D.M. Lindsay, J. Chem. Phys. **97,** 8811 (1992).

52. Z. Hu, B. Shen, J.R. Lombardi and D.M. Lindsay, J. Chem. Phys. **96,** 8757 (1992).

53. D. G. Leopold and W.C. Lineberger, J. Chem. Phys. **85,** 51 (1986).

54. J. Dong, Z. Hu, R. Craig, J.R. Lombardi, D.M. Lindsay, and W. Harbich, J. Chem. Phys. **101,** 9280 (1994).

55. M. Moskovits and J.E. Hulse, J. Chem. Phys. **66**, 3988 (1977).

56. T.C. DeVore, A. Ewing, H.F. Franzen and V. Calder, Chem. Phys. Lett. **35**, 78 91975).

57. C. Cosse' M. Fouassier, T. Mejean, M. Tranquille, D.P. DiLella and M. Moskovits. J. Chem. Phys. **73**, 6076 (1980).

58. G. Herzberg, *Spectra of Diatomic Molecules* (Van Nostrand, New York, 1950).

59. J. Ho, M.L. Pollack, K.M. Ervin, and W.C. Lineberger, J. Chem. Phys. **99**, 8542 (1993).

60. W.C. Lineberger, private communication.

61. T.L. Haslett and M. Moskovits, J. Molec. Spectrosc. **135**, 259 (1989).

62. E.A. Rolfing and J.J. Valentini, J. Chem. Phys. **85**, 51 (1986).

63. T.H. Upton and W.A. Goddard, J. Am. Chem Soc. **100**, 5659 (1978). I. Shim, J.P. Dahl and H. Johansen, Int. J. Quantum Chem. **15**, 311 (1979). J.O. Noell, M.D. Newton, P.J. Hay, R.L. Martin and F.W. Bobrowicz, J. Chem. Phys. **73**, 2360

(1980).

64. E.M. Spaing and M.D. Morse, J. Chem. Phys. **97**, 4641 (1992).

65. M. Moskovits and J.E. Hulse, J. Chem. Phys. **66**, 3988 (1977).

66. J.C. Pinegar, J.D. Langenberg, C.A. Arrington, E.M. Spain and M. D. Morse, J. Chem. Phys. **102**, 66 91995).

67. Z. Hu, J.-G. Dong, J.R. Lombardi, D.M Lindsay and W. Harbich, J. Chem. Phys. **101**, 95 (1994).

68. A.M. James, P Kowalczyk. R. Fournier and B. Simard, J. Chem. Phys. **99**, 8504 (1993).

References for Tantalum Dimer

69. See, for example, *Metal Clusters*, edited by M. Moskovits (Wiley, New York, 1986).

70. See, for example, J. Ho, K.M. Ervin, M.L. Polak, M.K. Giles, and W.C. Linegerger, J. Chem. Phys. **95**, 4845 (1991).

71. J. Ho, K. M. Ervin, and W.C. Lineberger, J. Chem. Phys. **93**, 6987 (1990).

72. D.G. leopold, T.M. Miller, and W.C. Lineberger, J. Am. Chem. Soc. **108**, 178 (1986).

73. W.C. Lineberger (private communicaiton).

74. R.D. Van Zee, S.C. Blanespoor, and T.S. Zweir, J. Chem. Phys. **88**, 4650 (1988).

75. Z. Hu, B.Shen, Q. Zhou, S.Deosaran, J.R. Lombardi, D.M. Lindsay, Proc. SPIE **1599**, 65 (1992).

76. Z. Hu, Q. Zhou, J.R. Lombardi, and D.M. Lindsay, in *Spectroscopy of mass-Selected Ziconium Dimers in Argon, in Physics and Chemistry of Finite Systems: from Clusters to Crystals*, edited by P. Jena, S.N. Khanna, and B.K. Rao (Kluwer Academic, Drodrecht, 1992).

77. M.D. Morse, Chem. Rev. **86**, 1049 (1986).

78. D.M. Lindsay, F. Meyer, and W. Harbich, Z. Phys D **12**, 15 (1989).

79. Z. Hu, Q. Zhou, J.R. Lombardi, D.M. Lindsay, and W. Harbich (in preparation).

80. We use units of nA-h (the product of current times the depostion time in hours) where 1 nA-h = 2.25 X 10^{13} particles.

81. W.R.M. Graheam and W. Weltner, J. Chem. Phys. **56**, 4400 (1971).

82. F. Schloch and E. Kay, J. Chem. Phys. **59**, 718 (1973).

83. M. Kreglewski and M. Vala, Chem. Phys. **56**, 381 (1981).

84. We also observed good guality absorption and excitiation spectra for atomic tantalum following depostions of about 100 nA-h of Ta^+ ions.

85. A.R. Gee, D.C. O'Shea, and H.Z. Cummins, Solid State Commun. **4**, 43 (1965).

86. S.P. Walch and C.W. Bauschlicher, in Comparison of ab initio Quantum Chemistry with Experiment, edited by R..J. Barlett (Reidel, Boston, 1985).

87. M.D. Morse, Adv. in Metal Semicond,. Clusters **1** (1992).

88. C. Cosse', M. Fouassier, T. Mejean, M. Tranquile, D.P. DiLella, and M. Moskovits, J. Chem. Phys. **73**, 6076 (1980).

89. M. Moskovits and W. Limm, Ultramicroscopy **20**, 83 (1986).

90. V.E. Bondybey and J.H. English, Chem. Phys. Lett. **94**, 443 (1983).

91. M.J. Pelin, T. Foosnaes, and D.M. Gruen, Am. Chem. Soc. Symp. Ser. **179**, 219 (1982).

References for Tantalum Tetramer

92. Z. Hu, B. Shem, Q. Zhou, S. Deosaran, J.R. Lombardi, D.M. Lindsay, and W. Harbich, J. Chem. Phys, **95**, 2206 (1991).

93. Z. Hu, B. Shen, Q. Zhou, S. Deosaran, J.R. Lombardi, and D.M. Lindsay, Proc. SPIE **1599**, 65 91992).

94. Z. Hu, Q. Zhou, J.R. Lombardi, and D.M. Lindsay, in Physics and Chemistry of Finite Systems: from Clusters to Crystals, edited by P. Jena, S.N. Khanna, and B.K. Rao (Kluwer Academic, Dordrecht, 1992), p. 969.

95. Z. Hu, J.-G. Dong, J.R. Lombardi, and D.M. Lindsay, J. Phys. Chem. **97**, 8811 (1992).

96. Z. Hu, B. Shen. J.R. Lombardi, and D.M. Lindsay, J. Chem. Phys. **96,** 8757 (1992).

97. C.S. Venkateswaran, Proc. Ind. Acad. Sci. **2A,** 260 (1935).

98. H.S. Gutowsky and C.J. Hoffman , J. Am. Chem. Phys. **72,** 5751 (1950).

99. L.R. Maxwell, S.B. Hendrick, and V.M. Mosley, J. Chem. Phys. **3,** 699 (1935).

100. C.D. Thomas and N.S. Gingrich, J. Chem. Phys. **6,** 659 (1938).

101. F.J. Kohl, O.M. Uy, and D. Carlson, J. Chem. Phys. **47,** 2667 (1967).

102. V.E. Bondybey and J.H. English, Chem. Phys. **73,** 42 (1980).

103. M. Morse (private communication).

104. G.A. Ozin and D.F. McIntosh, J. Phys. Chem. **90,** 5756 (1986).

105. E.C. Honea, A. Ogura, C.A. Murray, K. Raghavachari, W.O. Springer, M.F. Jarrold, and W.L. Brown, Nature **366,** 41

(1993).

106. R.J. VanZee, C.A. Baumann, and W. Weltner, J. Chem. Phys. **82**, 3912 91985).

107. G. Herzberg, *Infrared and Raman Spectra of Polyatomic Molecules*, Van Nostrand, Princeton, 1945).

108. I. B. Bersuker, *The Jahn-Teller Effect and Vibronic Interactions in Modern Chemistry* (Plenum, New York, 1984).

References for Zirconium Trimer

109 K. Balasubramanian and Ch. Ravimohan, J Chem. Phys. **92**, 3659 (1990).

110. C. W. Bauschilicher, Jr., H. Partidge, S.R. Langhoff, and M. Rosi, J. Chem. Phys. **95**, 1057 (1991).

111. Z. Hu, Q. Zhou, J.R. Lombardi, and D.M. Lindsay, in Physics and Chemistry of Finite Systems: from Clusters to Crystals, edited by P. Jena, S.N. Khanna, and B.K. Rao (Kluwer Academic, Dordrecht, 1992), p. 969.

112. D. Dai and K. Balasubraminian, Chem. Phys. Lett. **231**, 4 (1994).

113. D. Dai and K. Balasubramanian, Chem. Phys. Lett. **193**, 565 (1992).

114. Z. Hu, B. Shem, Q. Zhou, S. Deosaran, J.R. Lombardi, D.M. Lindsay, and W. Harbich, J. Chem. Phys, **95**, 2206 (1991).

115. Z. Hu, B. Shen, Q. Zhou, S. Deosaran, J.R. Lombardi, and D.M. Lindsay, Proc. SPIE **1599**, 65 (1992).

116. Z. Hu, Q. Zhou, S. Deosaran, J.R. Lombardi, and D.M. Lindsay, in *Physics and Chemistry of Finite Systems: From Clusters to Crystals*, edited by P. Jena, S.N. Khanna, and B.K. Rao (Kluwer, Dordrecht, 1992), p. 969.

117. Z. Hu, J.G. Dong, J.R. Lombardi and D. M. Lindsay, J. Phys. Chem. **97**, 9263 (1993).

118. Z. Hu, J.G. Dong, J.R. Lombardi and D.M. Lindsay, J. Chem. Phys. **97**, 8811 (1992).

119. Z. Hu, B. Shen, J.R. Lombardi and D.M. Lindsay, J. Chem. Phys. **96**, 8757 (1992).

120. G. Herzberg, Infrared and Raman Spectra of Polyatomic Molecules (van Nostrand, Princeton, 1945).

121. G. A. Ozin and D.F. McIntosh, J. Phys. Chem. **90**, 5756 (1986).

REFERENCES for Niobium Trimer

122. M.D.Morse, Chem.Rev. **86**, 1049(1986).

123. M.M.Kappes, Chem.Rev. **88**, 369(1988).

124. Z.Hu, J.-G.Dong, J.R.Lombardi, and D.M.Lindsay, J.Chem.Phys. **97**, 9263(1993).

125. H.Sellers, J.Phys.Chem. **94**, 1338(1990).

126. S.K.Loh, Li Lian, and P.B. Armentrout, J.Am.Chem.Soc. **111**, 3167(1989).

127. M.B.Knicklbein and S.Yang, J.Chem.Phys. **93**, 5760(1990).

128. Z.Hu, B.Shen, Q.Zhou, S.Deosaran, J.R.Lombardi, and D.M.Lindsay and W.Harbich, J.Chem.Phys. **95**, 2206(1991).

129. A.R.Gee, D.C.O'Shea, and H.Z.Cummins, Solid State Commun. **4**, 43(1965).

130. Z.Hu, B.Shen, Q.Zhou, S.Deosaran, J.R.Lombardi, and D.M.Lindsay, Proc. SPIE **1599**, 65(1991).

131. Z.Hu, B.Shen, J.R.Lombardi, and D.M.Lindsay, J.Chem.Phys., **96**, 8757(1992).

132. G.Herzberg, *Infrared and Raman Spectra of Polyatomic Molecules*(van Nostrand, Princeton, 1945).

133. T.G.Spiro and P.Stein, Am.Rev.Phys.Chem. **28**, 501(1977).

134. E.B.Wilson, Jr., J.C.Decius, and P.C.Cross, *Molecular Vibrations* (McGraw-Hill, New York,1971).

135. D.Dai and K.Balasubramanian, Chem.Phys.Lett. **231**, 4(1994).

REFERENCES for Rhodium Dimer, Rh_2

136. M. D.Morse, Chem.Rev. **86**, 1049(1986).

137. S.R. Langhoff and C.W. Bauschlicher, Ann.Rev.Phys.Chem. **82**, 5584 (1985).

138.R. Salahub, in *Ab Initio Methods in Quantum Chemistry II*, edited by K. P. Lawley (Wiley, New York, 1987), p. 447.

139. Shim, Mat. Fys. Meddr. Danske. Vidensk. Selsk.16 Res. Dep.Of Neils Bohr Fellows **41**, 147 (1985).

140. K. Balasubramanian and D. Liao, J. Phys. Chem., **93**, 3989 (1989).

141. F. Illas, J. Rubio, J. Canellas, and J.M. Ricart, J. Chem. Phys., **93**, 2603 (1996).

142. M. Harada and H. Dexpert, J. Phys. Chem., **100**, 565 (1996).

143. D.L.Cocke, and K.A. Gingerich, J. Chem. Phys., **60**, 1958 (1974).

144. Z.Hu, B.Shen, Q.Zhou, S.Deosaran, J.R.Lombardi, and D.M.Lindsay and W.Harbich, J.Chem.Phys. **95**, 2206(1991).

145. Z.Hu, B.Shen, J.R.Lombardi, and D.M.Lindsay, J.Chem.Phys., **96**, 8757(1992).

146. Z.Hu, B.Shen, Q.Zhou, S.Deosaran, J.R.Lombardi, and D.M.Lindsay, Proc. SPIE **1599**, 65 (1991).

147. Z.Hu, J.-G.Dong, J.R.Lombardi, and D.M.Lindsay, J.Chem.Phys. **97**, 9263 (1993) 65(1991).

148. G.Herzberg, *Spectra of Diatomic Molecules*(van Nostrand, Princeton, 1945).

149. Z.Hu, J.-G.Dong, J.R.Lombardi, and D.M.Lindsay, J.Chem.Phys. **101**, 95(1994) 65(1991).

REFERENCES for Ruthenium dimer, Ru_2

150. G. Sprintschink, H. Sprintschink, P. Kirsch and D. G. Whitten, J. Amer. Chem. Soc. **98**, 2337 (1976).

151. A. R. Miedema and K. A. Gingerich, J. Phys. **B12**, 2081 (1979) see alos: K. A. Ginerich, Faraday Symp. Chem. Soc. **14**, 109, (1980)

152. F. A. Cotton and I. Shim. J. Amer. Chem. Soc. **104**, 7025 (1982).

153. K. K. Das and K. Balasubramanian, J. Chem. Phys. **95**, 2568 (1991).

154. J. Andzelm, E. Radzio and D. R. Salahub, J. Chem. Phys. **83**, 4573 (1985).

155. H. Chem, M. Krasowski and G. Fitzgerald, J. Chem. Phys. **98**, 8710 (1993).

156. A. Goursot, L. Pedocchi and B. Coq., J. Phys. **98**, 8710 (1993).

157. M. Harada and H. Dexpert, J. Phys. Chem. **100**, 565 (1996).

158. Z. Hu, B. Shen, J. R. Lombardi and D. M. Lindsay, J. Chem. Phys. **96**, 8757 (1992).

159. Z. Hu, B. Shen, J. R. Lombardi and D. M. Lindsay, J. Chem. Phys. **96**, 8757 (1992); Z. Hu, B. Shen, Q. Zhou, S. Deosaran, J. R. Lombardi and D. M. Lindsay, Proc. SPIE **1599**, 65 (1991).

160. D. Haarer, J. Chem. Pphys. **67**, 4076 (1977).

161. C. Kittel, Introduction to Solid State Physics (John Wiley, New York, 1976).

162. G. Herzberg, *Spectra of Diatomic Molecules* (van Nostrand, New York, 1945).

163. S.M. Casey and D. G. Leopold, J. Phys. Chem., **97**, 816 (1993).

164. J. Ho, K. M. Ervin, M.L. Polak, M. K. Gilles and W. C. Linegerger, J. Chem. Phys., **95**, 4845 (1991).

165. K. P. Huber and G. Herzberg, Constants of Diatomic Molecules (Van Nostrand, New York, 1979).

166. For example, see: M. D. Morse, Chem. Rev. **86**, 1049 (1986); K. Balasubramanian, J. Chem. Phys, **89**, 5310 (1988); J. Ho, M. L. Polak, K. M. Ervin and W. C. Lineberger, J. Chem. Phys., **99**, 8542 (1993).

167. assuming equal bond contributions from sσ, dσ, dπ and dδ orbitals.

168. H. S. Johnston, Gas Phase Reaction Rate Theory (The Ronald Press, New York, 1966), Eqn. 4-55. See also: L. Pauling, J. Amer. Chem. Soc. 69, 542 (1947).